UNIVERSITY OF CALGARY

Two-mode squeezing in a cold atomic ensemble

by

Arina Tashchilina

A THESIS

SUBMITTED TO THE FACULTY OF GRADUATE STUDIES

IN PARTIAL FULFILLMENT OF THE REQUIREMENTS FOR THE

DEGREE OF DOCTOR OF PHILOSOPHY

GRADUATE PROGRAM IN PHYSICS AND ASTRONOMY

CALGARY, ALBERTA

NOVEMBER, 2019

Abstract

We investigate experimentally and theoretically the generation of a continuous variable entanglement using laser cooled atomic gas in free space and cavity mode. This is of a fundamental interest due to the nonclassical correlation of quadrature observables of the two-mode squeezed (TMS) state. The TMS state is the basis for complete quantum teleportation and continuous variable quantum repeaters. It is also used in quantum metrology and quantum key distribution.

We employ a novel scheme for generating a TMS vacuum based on a non-degenerate four-wave mixing process in a cold atomic cloud coupled to a cavity. We send two pumps collinear to the cavity mode and ensure that the two generated quantum fields are simultaneously resonant with the cavity. The cavity enhancement enables us to demonstrate results close to a free space in hot atomic gases (-5.2 dB) where optical densities are much higher.

Our system is versatile because, together with continuous variables, it is suitable for the discrete variable domain using the Duan-Lukin-Cirac-Zoller protocol. The design is oriented to make the delay between two modes possible and could be used for hybrid continuous repeaters. The system is devised and built fully as a part of my PhD, wherein we characterize our system and demonstrate the squeezing of -3.7 dB.

Since the quantum dynamics of the system is not intuitive, we provide simple models and consolidate segmental information on generation of TMS states. To make sure that the dynamics is not oversimplified, we construct a novel theory where we treat both fields and atoms as quantum objects. The theory supports and enriches our understanding and confirms our experimental data. Based on the experimental and theoretical results we spotlight the detrimental effects and propose improvements to our system.

We theoretically investigate that the certain class of TMSV states are optically dark. These states propagate through a polarized to one hyperfine level Λ atoms without degradation or evolution. Based on this we propose a new way of generation of TMSV through the dissipation or dynamically controlled broadening.

Acknowledgements

I would like to thank Eugene Moiseev for being patient, for inspiring and teaching me during these long six years. I would like to thank Patrick J. Irwin for always willing to discuss my project, for giving practical suggestions, and for sharing kindness. I would like to thank Sergey Moiseev for being eager to go through pages of algebra and helping to find meaning in it. I would like to thank my supervisors, Alexander Lvovsky and Barry Sanders, who helped me from the first until the last day. Special thanks to my colleagues who I had a special pleasure to work with: Xianxin Guo, Fan Yang, Duncan McIntyre, Kenzo Makino. Kenneth Fox, Paul Papin, and Mariann Howell helped me to become a better writer. Judy Chew gave me an emotional support during the toughest months.

Table of Contents

List of Figures and Illustrations

List of Tables

List of Symbols, Abbreviations and Nomenclature

AOM	Acousto-optical modulator
BS	beam splitter
CV	continuous variable
DAVLL	dichroic atomic vapour laser lock
DDS	direct digital synthesizer
DLCZ	Duan-Lukin-Cirac-Zoller protocol
ECDL	external-cavity diode laser
EPR	Einstein-Podolsky-Rosen
EOM	electro-optic modulator
FSR	free spectral range
FWHM	full width at half maximum
FWM	four-wave mixing
HV	high vacuum
HWP	half-wave plate
LO	local oscillator
LPF	low-pass filter
MOT	magneto-optical trap
OD	optical depth
OPA	optical parametric amplifier
opamp	operational amplifier

OPLL	optical phase-locked loop
OPO	optical parametric oscillator
PBS	polarizing beam splitter
PDH	Pound–Drever–Hall technique
PID	proportional–integral–derivative controller
PLL	phase-lock loop
QWP	quarter-wave plate
RBW	resolution bandwidth
RF	radio frequency
RWA	rotating-wave approximation
SQL	standard quantum limit
TMS	two-mode squeezing
TMSV	two-mode squeezed vacuum
UHV	ultra-high vacuum
VBW	video bandwidth
^{87}Rb	Atom Rubidium 87
k_B	Boltzmann constant
$\sigma^{\pm}$	right (left) circularly polarized light

Chapter 1

Introduction

Interest in continuous variable entanglement arose at the early stage of quantum theory. Einstein, Podolsky, and Rosen questioned the consistency of the theory and triggered the quantum non-locality debate by providing the special example of the extreme continuous entanglement state, later named the EPR state after the authors [1]. The experimental capability to investigate similar states came only after decades of developments across the field of quantum optics. The generation of squeezed states in hot atomic gas [2] and later in nonlinear crystals [3] allowed the conversion of non-classical noise properties of electromagnetic quadrature into non-classical correlations between quadratures of the different modes [4]. The obtainable two-mode squeezed vacuum (TMSV) state is a workhorse for fundamental studies and is of special value for quantum science and technology [5]. TMSV is the basis of complete quantum teleportation [6], continuous variable (CV) quantum repeaters [7], quantum metrology [8, 9], and quantum key distribution [10, 11].

Squeezing is mainly generated via parametric processes, when nonlinear media mediates scattering of pumping fields into photons having correlated properties. The nonlinear processes include parametric down-conversion in nonlinear crystals [3, 12] and four-wave mixing (FWM) in both fibers [13] and atomic gases [14, 15]. Other exotic media to generate squeezing are semiconducting lasers [16], optomechanical systems [17], rare earth ion doped crystals

[18, 19], as well as non-optical squeezing in microwave domain [20] and trapped ions [21]. The generation of a TMSV within an atomic ensemble has a special interest with perspective of integration with atomic quantum memories for a large scale network.

1.1 Squeezing generation

Squeezing was first observed in 1985 via degenerate FWM in a hot sodium vapour [2]. In this experiment the quadratures of the single optical mode were squeezed by –0.3 dB below the standard quantum limit. Implementation of a cold atomic cloud in a cavity for squeezing generation by the Giacobino group helped to improve the previous result to –1 dB [22], but no entanglement investigation was done. Subsequent work by the same group [23] allowed observation of two-mode squeezing and the corresponding violation of the separability criteria in continuous variables [24]. The low value of the squeezing in these experiments was explained by unwanted incoherent processes such as Raman scattering, which result in increased noise in quadrature correlations.

A substantial increase in two-mode squeezing generation in atomic ensembles was achieved in hot vapor by McCormick et al. [25]. The mechanism they employed for two-mode squeezing was FWM, which was induced by a far-detuned continuous pump acting on both transitions in the atomic Λ scheme. The resulting Stokes and anti-Stokes modes exhibit correlations in the number of photons. An extra seeding of one of the modes with a coherent state displaces both states by a complex amplitude, thus producing a displaced two-mode squeezing. The displacement partially removes the problem with excess noise, since the contributions of harmful fluctuations from other nonlinear processes cancel out [25, 26]. This seeded TMS is called either twin-beam or intensity squeezing.

Later, the same system was used to demonstrate spatially multimode quadrature squeezing [15]. A noise reduction of –4 dB below the vacuum level was achieved by exploiting the coherence of the long-lived atomic hyperfine states. The local oscillator (LO) was sent

through the same atomic cell in order to reduce the phase fluctuation between the photons and LO and, hence, to see the quadtrature correlation below the vacuum level. The use of a LO having different spatial modes helped to quantify entanglement between different spatial modes. Shortly after this experiment, time delayed entanglement was demonstrated by sending one of the conjugated beams through the slow light media formed [27]. We summarize six important experiments on TMS generation in atomic ensembles in Table 1.1. We additionally mention milestones on squeezing generation in other media, among which are the first generation of TMS [4] and the record value of TMS [12] (highlighted with gray color).

Atoms	**Atomic media**	**Type of Squeezing**	**Squeezing level, dB**	**Reference**	**Year**
Na	atomic beam	Single mode	-0.3	Slusher [2]	1985
$KTiOPO_4$	crystal	Intensity	-1.55	Heidmann [4]	1987
Cs	MOT	Quadrature	-0.22	Josse [23]	2004
^{85}Rb	vapour	Intensity	-8.1 (-3.5)	McCormick[25]	2007
^{85}Rb	vapour	Intensity	-8.8	McCormick[28]	2008
^{85}Rb	vapour	Quadrature	-5.2 (-4.3)	Boyer[15]	2008
Cs	room T	Quadrature	-3.5	Wasilewski [29]	2009
^{85}Rb	vapour	Intensity	-9.2	Glorieux [14]	2011
PPKTP	crystal	Quadrature	-10.45	Eberle [12]	2013

Table (1.1) Two-mode squeezing in atomic ensembles, with the first experiment on a single-mode squeezing included. In the brackets are the values uncorrected for losses if given.

1.2 Duan-Lukin-Cirac-Zoller protocol

A similar approach in a slightly different context was proposed for creating a discrete variable repeater [30] and called after the authors: Duan, Lukin, Cirac, and Zoller (DLCZ). In this protocol, a polarized atomic sample with the Λ-level scheme is exposed to a pump that acts on one transition. The resulting Raman scattering creates TMSV between the scattered light and the atomic excitation. The detection of scattered light projects the created entanglement between atoms and light into an atomic coherent excitation superposition. If

the atomic sample is homogeneous and has a large enough coherence time, the application of the second strong counter-propagating pump converts the atomic excitation into a photonic mode with a given wavevector, which is determined by the phase matching of two applied pumps and scattered photons. Thanks to the coherent enhancement, the probability of restoring the excitation or retrieval efficiency is proportional to $1 - e^{-\alpha}$, where α is the ensemble's optical depth [31].

The first demonstration of single photon generation was performed in cold atomic gas, where non-classical properties of restored field has been observed [32, 33]. Subsequent research extended the protocol applicability with temporal and spatial multimodeness [34, 35], the long lifetime of atomic coherence [36, 37, 38], and enhanced efficiency [39, 40]. Furthermore, in some experiments high efficiency has been combined with a long lifetime [41, 42].

The two mechanisms behind the lifetime extension were the confinement of atoms in an optical lattice and the use of collinear geometry, both of which minimize dephasing due to atomic motion. Moreover, both the optical lattices operating at the magic wavelength [43] and the encoding of atomic excitation on magnetically insensitive levels suppress inhomogeneity—due to optical Stark shifts and magnetic field—and extend the lifetime further.

High efficiency requires significant optical depth of an ensemble. The straightforward increase of optical depth can be done by employing a denser atomic ensemble, for example, the compressed 2D magneto-optical trap [44]. In the same time the large density introduces inhomogeneity, which limits efficiency and coherence lifetime. Trapping an atomic ensemble with high optical depth is also challenging, due to larger atom-atom interaction within the trap. Another way to effectively enhance an optical depth is to use an optical cavity. It seems to be the more prominent approach that combines benefits of trapped dilute gas with high restoring efficiency [42].

1.3 Motivation

We propose to extend the DLCZ system into the continuous variable domain. As a method it holds promise for generating of two-mode squeezed light with a long programmable delay [45]. The most obvious application of continuous variables is unconditional teleportation between atomic ensembles, which has the advantage of transferring quantum states with subsequent purification [46, 47].

The setup's versatility allows operation in two regimes, discrete and continuous. While the continuous domain spans over the infinite basis, in the discrete domain, information is encoded in an arbitrary superposition of two orthogonal states of photon: $\alpha\,|\,0\,\rangle + \beta\,|\,1\,\rangle$. The discrete states, $|\,0\,\rangle$ and $|\,1\,\rangle$, can be set by different physical degrees of freedom: the Fock basis, polarization states, frequency or time bins, and different spatial modes [48]. One major advantage of the discrete variables in communication is that in most bases the encoded quantum information is not affected by linear loss. Herein, losses do not decrease the fidelity of the measured state, but they only reduce the communication rate between two parties.

CVs however deal with observables having a continuous spectrum of eigenvalues, such as canonical position or momentum of electromagnetic mode. The main advantage of the CV is its ability to perform an unconditional swap between two remotely separated entangled states via a phase-space displacement, conditioned on the measurement result [49]. In this case, the losses degrade the fidelity of the prepared state but do not change the rate. Therewith, there exist hybrid schemes that combine the strengths of both domains [50, 51].

Thus, the developed setup would be capable of working in hybrid version of quantum teleportation and repeater protocols. Several identical setups of this kind should also allow the creation of an entanglement between discrete and continuous variable systems and teleportation of a discrete variable state using CV protocols.

1.4 Methods

In our work we would like to combine promising approaches towards the single system, which unites the collective coherent enhancement of the emission by a cavity and advantages of cold atomic ensembles as the light storage media. The use of the optical cavity for Stokes and anti-Stokes photons defines the spatial modes and increases efficiency. It could be understood as the incoming light bounces back and forth between the mirrors, thus increasing effective interaction duration. High efficiency manifests itself as high coincidence counts in a single photon regime and as a quadrature correlation below the standard quantum limit in continuous variables.

By means of laser cooling the atoms are slowed down to the temperatures below 100 μK. Thus atoms could be considered effectively stationary during short interaction times. Together with that, cooling removes the Doppler inhomogeneous broadening, narrowing atomic linewidth to the natural one. Long-lived hyperfine coherence of the cold atomic ensemble enables millisecond storage time and can be extended to a sub-second by confining gas in an optical dipole trap [42].

The detection of two-mode squeezing and hence the CV entanglement is performed by means of homodyne detection [52]. The homodyne detection produces an output based on a result of an interference between the input state and the classical wave with a given complex amplitude. The technique allows measurement of an arbitrary superposition of canonical position and momentum of the electromagnetic mode. Subsequent processing of the measurement discloses nonclassical correlations between the modes.

Theoretically the system is analyzed in the Heisenberg-Langevin picture [53]. The obtained system of stochastic differential equation enables to build up intuitive and qualitative description of the experiment. The different regimes of operation and proper control parameters of the experiment can be validated through the theoretical analysis.

1.5 Outline

In this dissertation I study two mode squeezing generation in atomic ensembles both experimentally and theoretically. Each chapter has a detailed outline, below I give the general concept and the roadmap of my dissertation.

The second chapter covers the requisite theoretical background. Introductory Section 2.1 sets forth the three main concepts of two-mode squeezing: definition, generation, and measurement. It is followed by a basic semiclassical model of an optical parametric oscillator that evinces the genuine generation process and notable regimes of operation. The subsequent section describes the basic theory of light-atom interaction, where an ensemble of two-level atoms is coupled to a cavity mode. Based on this, a fully quantum model is built to describe four-wave mixing in an atomic sample that interacts with two cavity modes and two classical pumps. The quantum and macroscopic properties of the generated light are presented as the primary results of the chapter.

In the third chapter a new approach of two mode squeezing generation is proposed. In contrast to the traditional approach where generation is achieved through unitary evolution, we theoretically justify its appearance in the presence of dissipation. The system under investigation has a typical Λ-type atomic structure, with two pumping fields addressing both optical transitions and two signal fields, which are in two-photon resonance with the pumps. We reveal that a TMSV state with a particular squeezing parameter propagates through this media without absorption (is a "dark" state). Besides theoretical justification of our idea, we find a number of experiments showing evidence of the proposed mechanism.

The next chapter is devoted to an experimental apparatus and techniques for developing a cold atomic ensemble interacting with a cavity. The approaches used are general and applicable to most quantum optical experiments with atoms. In our work we combine well-known techniques with home-made electronics to best fit our needs, or minimize the costs. In this chapter we describe tools emphasizing their applicability ranges and suggesting modifications for further improvement of the performance. Our experiment encompasses

atomic cloud preparation, lasers that address the atoms, cavity assembly and stabilization, the frequency locking circuits, the optical detection scheme, and data acquisition.

In Chapter 5, we demonstrate the performance and the results of the experiment, based on the framework from Chapter 2 and methodology from Chapter 4. In Sections 5.2–5.1 we characterize our system as a source of two-mode squeezed light. The primary evidences of TMS—two mode squeezing spectrum and time domain correlation—are presented in Section 5.3.

Chapter 2

Theory

The theoretical aspects of the two-mode squeezing generation process are described in this chapter. We progress from a simple semiclassical model to a fully quantum description. The first two sections aim to build an intuition of squeezed states that will become a base model for the more advanced quantum description. In Section 2.1, we derive the two-mode squeezed state in the Fock and position bases. This derivation allows us to describe the main properties of this state and its generation process. We account for losses via a beam-splitter model and show how it affects the squeezing level. In Section 2.2, we construct a simple model for a parametric process inside a cavity, and we analyze its regimes of operation and the behaviour of observables in the Fourier-domain. To model experimental conditions, we include losses into the physical system by means of the Langevin-Heisenberg equations. In Section 2.3, we outline the cavity quantum electrodynamics approach as a quantum description of light-matter interaction. Finally in the last Section 2.4, we present a generalized theory that includes atomic level structure, two quantized cavity modes, and two coherent fields inducing the four-wave mixing process. This derivation is done specifically for our system and is novel.

2.1 Two-mode squeezed state

Different quantum states of the electromagnetic field having various non-classical properties are actively used in implementation of quantum information protocols and fundamental quantum experiments such as teleportation, quantum key distribution, quantum computing, boson sampling, and Bell's inequality [54, 55, 56].

The most practical approach for generation of various two mode quantum states is spontaneous parametric scattering in a crystal with $\chi^{(2)}$ nonlinearity. In this process a nonlinear crystal is pumped by a continuous wave or pulsed laser. Nonlinearity induces the decay of the pump photon into two idler and signal photons. Energy and momentum conservation dictates conditions for the frequency and wavevector of the scattered photons:

$$\omega_{\mathrm{p}} = \omega_{\mathrm{s}} + \omega_{\mathrm{i}} \quad \text{and} \quad \boldsymbol{k}_{\mathrm{p}} = \boldsymbol{k}_{\mathrm{s}} + \boldsymbol{k}_{\mathrm{i}}, \tag{2.1}$$

where $\omega_{\mathrm{p,s,i}}(\boldsymbol{k}_{\mathrm{p,s,i}})$ is the frequency (wavevector) of the pump, signal, and idler photons. The refractive index of the crystal makes fulfillment of momentum conservation more demanding, since (2.1) is expressed as $\omega_{\mathrm{p}} n_{\mathrm{p}} = \omega_{\mathrm{s}} n_{\mathrm{s}} + \omega_{\mathrm{i}} n_{\mathrm{i}}$. The common technique to satisfy this condition is birefringent phase matching [57], where the matching of a refractive index for ordinary and extraordinary polarizations happens at a particular temperature. Depending on the crystal cut different phase matching regimes could be exploited. For a Type I crystal the process is degenerate, i.e., signal and idler photons have the same polarization; for a Type II crystal the scattered photons have orthogonal polarizations.

For a description of the quantum properties we need to provide a quantum description of spontaneous parametric down conversion and the generated state. Generally speaking, the dynamics of the process are dictated by the effective Klyshko Hamiltonian [58]:

$$\hat{H} = \hbar \chi^{(2)} \Omega a^{\dagger} b^{\dagger} e^{-i(\omega_{\mathrm{p}} - \omega_{\mathrm{s}} - \omega_{\mathrm{i}})t + i(\boldsymbol{k}_{\mathrm{p}} - \boldsymbol{k}_{\mathrm{s}} - \boldsymbol{k}_{\mathrm{i}})\boldsymbol{r}} + \mathrm{h.c.}, \tag{2.2}$$

where $a, (a^\dagger), b, (b^\dagger)$ are canonical creation (annihilation) operators for signal and idler modes, Ω is the C-number corresponding to the amplitude of a pump with a phase ϕ, and $\chi^{(2)}$ is an effective nonlinearity coefficient.

It may seem that we have constrained ourselves to study of only spontaneous parametric down-conversion. In fact the same Hamiltonian governs other nonlinear processes. The FWM—the main scope of this dissertation—is based on a third-order nonlinearity $\chi^{(3)}$ and involves four waves: two pumping fields and two created fields. Nevertheless the FWM process is described by the same effective Hamiltonian under assumption of strong undepleted pumping fields. In this case, constants in Hamiltonian (2.2) should be replaced according to $\chi^{(2)} \to \chi^{(3)}$ and $\Omega \to \Omega_1\Omega_2$, where Ω_1 and Ω_2 are Rabi-frequencies of pumps. Further phase matching changes to include all four waves: $\omega_{\rm p1} + \omega_{\rm p2} = \omega_{\rm s} + \omega_{\rm i}$ and $\boldsymbol{k}_{\rm p1} + \boldsymbol{k}_{\rm p2} = \boldsymbol{k}_{\rm s} + \boldsymbol{k}_{\rm i}$.

2.1.1 Two-mode squeezed state in Fock basis

If conditions (2.1) are satisfied, the Hamiltonian governs the following evolution:

$$|\,\Psi(t)\,\rangle = \exp\left(-\frac{i\hat{H}}{\hbar}t\right)|\,\Psi(0)\,\rangle = \exp\left(\chi^{(2)}\,|\,\Omega\,|\,t\left(-a^\dagger b^\dagger e^{i\phi} + abe^{-i\phi}\right)\right)|\,\Psi(0)\,\rangle\,, \tag{2.3}$$

the time t here corresponds to time in the traveling wave reference frame. In this case the output from a crystal with length l would correspond to time evolution $t = nl/c$. Usually the evolution operator (2.3) is called the two-mode squeezer and is written in the form

$$S(r,\phi) = \exp\left(-\frac{i\hat{H}}{\hbar}t\right) = e^{r(-a^\dagger b^\dagger e^{i\phi} + abe^{-i\phi})}, \tag{2.4}$$

where $r = \chi^{(2)}\,|\,\Omega\,|\,nl/c$ (or $r = \chi^{(3)}\,|\,\Omega_1\,|\,|\,\Omega_2\,|\,nl/c$) is the squeeze parameter.

The simplest example of a correlated two-mode state is the two-mode squeezed vacuum

generated by the action of the two-mode squeezer on the two-mode vacuum:

$$|\,\mathrm{TMSV}\,\rangle = e^{r(-a^\dagger b^\dagger e^{i\phi} + ab e^{-i\phi})}\,|\,0,0\,\rangle\,. \tag{2.5}$$

If we introduce operators $K_+ = a^\dagger b^\dagger$, $K_- = ab$, and $2K_0 = n_a + n_b + 1$ with commutation relationships $[K_-, K_+] = 2K_0 = [ab, a^\dagger b^\dagger] = [ab, a^\dagger]b^\dagger + a^\dagger[ab, b^\dagger] = bb^\dagger + a^\dagger a = n_a + n_b + 1$, they form the SU(1,1) algebra that provides a relationship [59]:

$$e^{\alpha_0 K_0 + \alpha_+ K_+ + \alpha_- K_-} = e^{\gamma_+ K_+} e^{\log(\gamma_0) K_0} e^{\gamma_- K_-}, \tag{2.6}$$

where $\gamma_0 = \left(\cosh r - \frac{2\alpha_0}{r}\sinh r\right)^{-2}$, $\gamma_\pm = \frac{2\alpha_\pm \sinh r}{2\theta\cosh r - \alpha_0 \sinh r}$, $r = \sqrt{\frac{\alpha_0^2}{4} - \alpha_+\alpha_-}$. From the form of the squeezer we find coefficients $\alpha_0 = 0$, $\gamma_+ = \frac{\alpha_+}{\phi}\tanh r$ and the two-mode squeezed vacuum state has the form:

$$|\,\mathrm{TMSV}\,\rangle = \frac{e^{-\tanh r \cdot a^\dagger b^\dagger e^{i\phi}}}{\cosh r}\,|\,0,0\,\rangle\,. \tag{2.7}$$

If we introduce a new notation $\epsilon = e^{i\phi}\tanh r$, then for two harmonic oscillators described by annihilation and creation operators $a(a^\dagger)$ and $b(b^\dagger)$, the two-mode squeezed vacuum state can be written as

$$|\,\mathrm{TMSV}\,\rangle = \sqrt{1-|\epsilon|^2}\, e^{-\epsilon a^\dagger b^\dagger}\,|\,0,0\,\rangle\,. \tag{2.8}$$

where $\sqrt{1-|\epsilon|^2}$ is a normalization constant with $|\,\epsilon\,| < 1$. If we expand an exponent in a Taylor series we note that the state is the sum of pairwise generated photons in two modes.

2.1.2 Two-mode squeezed state in continuous variables

As we can see from (2.8) TMSV is spanned over the whole infinite Fock basis, thus it is natural to represent it also in continuous variables, rather than only in the excitation

number representation. Before proceeding further, we assume the following conventions for dimensionless canonical position and momentum operators: $\hat{X} = \frac{\hat{a}+\hat{a}^\dagger}{\sqrt{2}}$ and $\hat{P} = \frac{\hat{a}-\hat{a}^\dagger}{\sqrt{2}i}$ with the commutation relation $[\hat{X}, \hat{P}] = i$. The squeezing operator modifies these quadratures according to the Bogoliubov transformation:

$$S^\dagger(r,\phi)\hat{X}_a S(r,\phi) = \cosh r\hat{X}_a + \sinh r\hat{X}_b, \tag{2.9}$$

$$S^\dagger(r,\phi)\hat{X}_b S(r,\phi) = \cosh r\hat{X}_b + \sinh r\hat{X}_a. \tag{2.10}$$

The vacuum state wavefunction $|\,0,0\,\rangle$ in the position representation is Gaussian and stays Gaussian after the transformation [60]:

$$\frac{1}{\sqrt{\pi}} e^{-\hat{X}_a^2/2-\hat{X}_b^2/2} \to \frac{1}{\sqrt{\pi}} e^{-(\cosh r X_b+\sinh r X_a)^2/2-(\cosh r X_a+\sinh r X_b)^2/2}. \tag{2.11}$$

After this rearrangement, the position wavefunction for a TMSV is

$$\Psi(X_a, X_b) = \frac{1}{\sqrt{\pi}} e^{-e^{-2r}(X_a-X_b)^2/4-e^{2r}(X_a+X_b)^2/4}. \tag{2.12}$$

Each quadrature on its own is not squeezed, on the contrary, its range of possible values is stretched (Fig. 2.1). However, if we measure the coordinate of one of the parties, then the coordinate of the second mode will lie in a narrower range compared to the vacuum. In the extreme case of an infinite squeezing, two modes (particles) are in the EPR state. If we measure the coordinate of one mode, we can have an exact answer for the coordinate of the second mode. Whilst this information is obtained without disturbing the second particle, the entanglement between parties is destroyed and the momenta of the second particle becomes fully uncertain.

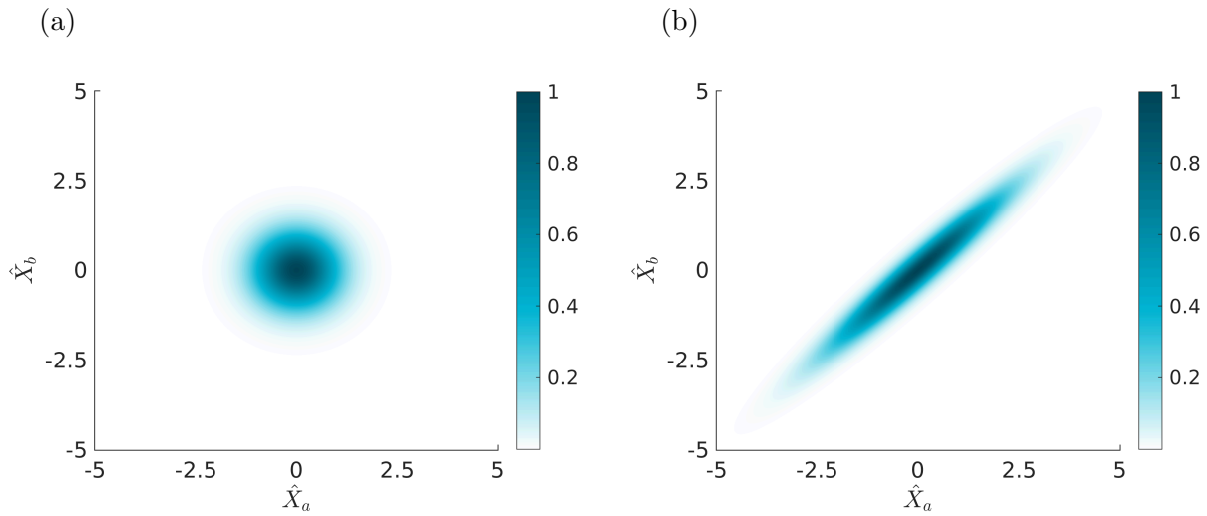

Figure (2.1) The position wavefunction of a two-mode state either in (a) vacuum or (b) two-mode squeezed state with $r = -1$

2.1.3 Canonical quadrature correlations

We have shown in the previous section non-classical correlations between quadratures of two modes in a phase space, although for a consistent theory we need to have a mathematical measure to characterize squeezing. The common approach is to find uncertainties[1] of two Hermitian operators which obey the Heisenberg uncertainty relation:

$$\sqrt{\langle\, \Delta\hat{A}^2 \,\rangle \cdot \langle\, \Delta\hat{B}^2 \,\rangle} \geq \frac{1}{2} |\, \langle\, [A, B] \,\rangle\, | \,. \tag{2.13}$$

Specifically for the canonical position and momentum operators the Heisenberg inequality sets the lower bound for the product of uncertainties: $\sqrt{\langle\, \Delta\hat{X}^2 \,\rangle \cdot \langle\, \Delta\hat{P}^2 \,\rangle} \geq \frac{1}{2}$. The state is called single-mode squeezed if the variance of one of the operators goes below this limiting value $\langle\, \Delta\hat{X}^2 \,\rangle < \frac{1}{2}$ at the expense of uncertainty of a conjugate operator $\langle\, \Delta\hat{P}^2 \,\rangle > \frac{1}{2}$. Both vacuum and coherent states are the minimum-uncertainty states with $\langle\, \Delta\hat{X}^2 \,\rangle = \langle\, \Delta\hat{P}^2 \,\rangle = \frac{1}{2}$. Thus the squeezed state allows to resolve signals below the shot-noise level or below vacuum level.

The two-mode squeezed state involves two harmonic oscillators, where each of them on its

[1] An uncertainty or standard deviation is $\sqrt{\langle\, \Delta\hat{A}^2 \,\rangle} = \sqrt{\langle\, \hat{A}^2 \,\rangle - \langle\, \hat{A} \,\rangle^2}$

own is not squeezed, but is in a thermal state. At the same time, the canonical quadratures of two modes are nonclassicaly correlated, what could be demonstrated with the two-mode position sum (difference)

$$\hat{X}_{\pm} = \frac{\hat{X}_a \pm \hat{X}_b}{\sqrt{2}} = \frac{\hat{a} + \hat{a}^\dagger \pm \hat{b} \pm \hat{b}^\dagger}{2} \tag{2.14}$$

and the two-mode position sum (difference) variances:

$$\langle\, \Delta\hat{X}_{\pm}^2 \,\rangle = \frac{\langle\, \hat{a}\hat{a} + \hat{a}^\dagger\hat{a}^\dagger + \hat{b}\hat{b} + \hat{b}^\dagger\hat{b}^\dagger + 2(\hat{n}_a + \hat{n}_b + 1) \,\rangle \pm 2\langle\, \hat{a}\hat{b} + \hat{a}^\dagger\hat{b} + \text{h.c.} \,\rangle}{4} - \langle\, \hat{X}_{\pm} \,\rangle^2. \tag{2.15}$$

The standard quantum limit (SQL) noise is the variance (2.15) taken with respect to the vacuum in both channels. Similarily, to a single-mode case, it is one half $\langle\, \Delta\hat{X}_{\pm}^2 \,\rangle_{\text{vac}} = 1/2$.

Let us find variances for the TMSV state. The decomposition in a Fock-basis (2.8) dictates that an average over TMSV in Equation (2.15) only leaves the terms that keep the number of photons in both modes the same:

$$\langle\, \Delta\hat{X}_{\pm}^2 \,\rangle_{\text{TMSV}} = \frac{\langle\, \hat{n}_a \,\rangle_{\text{TMSV}} + \langle\, \hat{n}_b \,\rangle_{\text{TMSV}} + 1 \pm \langle\, \hat{a}\hat{b} + \text{h.c.} \,\rangle_{\text{TMSV}}}{2}. \tag{2.16}$$

The mean number of photons $\langle\, n \,\rangle$ in a single mode of $|\,\text{TMSV}\,\rangle$ state:

$$\langle\, \hat{n} \,\rangle_{\text{TMSV}} = \left(1 - |\,\epsilon\,|^2\right) \sum_n |\,\epsilon\,|^{2n}\, n = \frac{|\,\epsilon\,|^2}{1 - |\,\epsilon\,|^2}. \tag{2.17}$$

The correlation terms are

$$\langle\, \hat{a}\hat{b} + \hat{a}^\dagger\hat{b}^\dagger \,\rangle_{\text{TMSV}} = -\frac{2\Re e(\epsilon)}{1 - |\,\epsilon\,|^2}. \tag{2.18}$$

Thus the variance of sum (difference) of quadratures is

$$\langle \Delta \hat{X}_{\pm}^2 \rangle_{\text{TMSV}} = \frac{1}{2} \frac{1 + |\epsilon|^2 \mp 2\Re e(\epsilon)}{1 - |\epsilon|^2} = \frac{1}{2} \frac{1 + r^2 \mp 2r\cos(\phi)}{1 - r^2}. \tag{2.19}$$

Angle ϕ—the phase of the pump—sets the quadratures among which we have squeezing. As an example $\phi = 2\pi n$ will result in

$$\langle \Delta \hat{X}_{\pm}^2 \rangle_{\text{TMSV}} \Big|_{\phi=2\pi n} = \frac{1}{2} \frac{1 \mp \epsilon}{1 \pm \epsilon} = \frac{1}{2} e^{\mp 2r}, \quad n \in \mathbb{Z}. \tag{2.20}$$

If the squeeze parameter is nonzero, the uncertainty of the sum of the position operators is lower than the vacuum level fluctuations (SQL), at the same time the difference has an excessive noise. As angle ϕ changes, the error contour rotates, and at angles $\phi = (n+1)\pi$ the situation is reversed: the difference is squeezed and the sum is anti-squeezed.

2.1.4 Arbitrary quadrature correlations

The quadratures experiencing squeezing are not always canonical position and momentum, but generalized quadratures, which are obtained from the former by a rotation on an arbitrary angle. These generalized quadratures are written for the intermediate angle θ, where the angle is between the electric field amplitude and a classical reference wave[2]:

$$\hat{Q}(\theta) = \cos\theta \hat{X} + \sin\theta \hat{P} = \frac{\hat{a}e^{-i\theta} + \hat{a}^\dagger e^{i\theta}}{\sqrt{2}}, \tag{2.21}$$

where $\theta \in \{0, \pi\}$ and conjugate quadrature is $\hat{Q}(\theta + \pi/2)$. Following the same line of derivations as in the previous section, and assuming each mode to have its own quadrature with phase θ_a or θ_b, we arrive to a variance of two arbitrary quadratures of two modes

[2]Electric field in canonical quadratures: $\hat{E}_k \propto \hat{X}_k \cos(\omega_k t - kr) + \hat{P}_k \sin(\omega_k t - kr)$ or in generalized quadratures: $\hat{E}_k \propto \hat{Q}_k(\theta)\cos(\omega_k t - kr - \theta) + \hat{Q}_k(\theta + \pi/2)\sin(\omega_k t - kr - \theta)$, please see [5].

averaged over TMSV:

$$\langle\, \Delta\hat{Q}_{\pm}^2 \,\rangle_{\mathrm{TMSV}} = \frac{1}{2}\left(\frac{1+r^2 \mp 2r\cos\left(\phi+\theta_a+\theta_b\right)}{1-r^2}\right). \tag{2.22}$$

Obviously, the properly chosen quadrature phase $(\theta_a+\theta_b) = -\phi$ allows measurement of the squeezing of the corresponding quadrature. Thus the phase ϕ determines which pairs of quadratures are squeezed, e.g., at $\phi = 0$ the difference in positions $\hat{X}_-$ is squeezed, while at $\phi = \pi/2$ the difference in momenta $\hat{P}_- = \hat{P}_1 - \hat{P}_2$.

2.1.5 Number of photon distribution

If we expand an exponent from Equation (2.8) in a Taylor series we note that the state is the sum of pairwise generated photons in two modes:

$$|\,\mathrm{TMSV}\,\rangle = \sqrt{1-|\epsilon|^2}\sum_{n=0}^{\infty}(-\epsilon)^n\,|\,n,n\,\rangle\,. \tag{2.23}$$

Each next term has less weight ($|\,\epsilon\,| < 1$), although for ideal squeezing we need an infinite number of photons. The perfectly squeezed state is impossible to generate, although we can select the fidelity we need and truncate the series at the required point.

We ask ourselves how many pairs of photons do we need for a desirable squeezing level. In Figure 2.2(a) we demonstrate the amount of squeezing as a function of the averaged number of photons in the TMSV state. From this graph we can conclude that even the highest ever recorded value of TMSV (Table 1.1) does not require a high mean number of excitations—only two photons for –10 dB of squeezing. Although this could be misleading as we do not know a standard deviation. For this we find the distribution of photons in TMSV state to be

$$p(n) = \frac{\langle\, n\,\rangle^n}{(\langle\, n\,\rangle+1)^{n+1}} \tag{2.24}$$

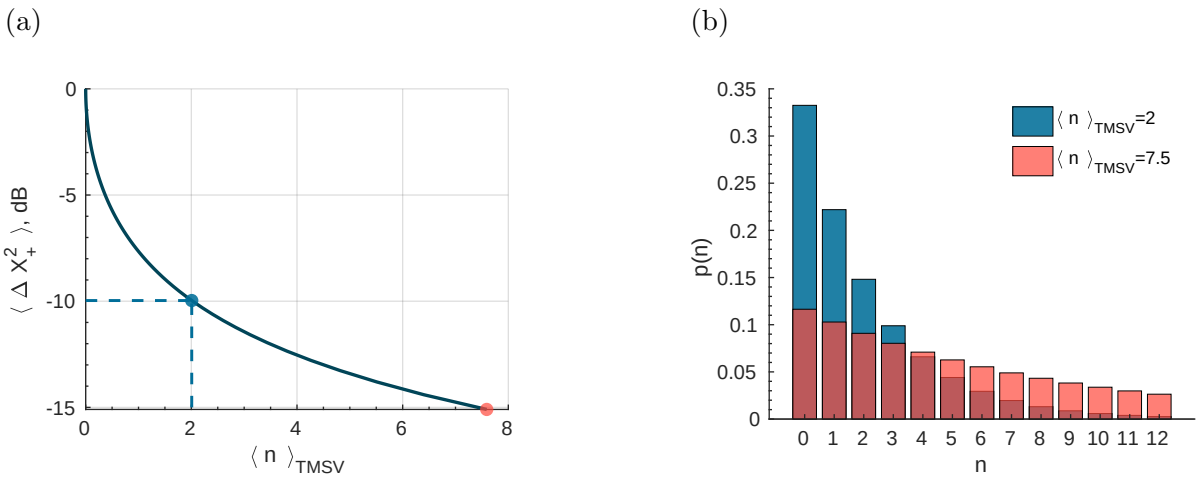

Figure (2.2) (a) Dependence of squeezing level on the averaged number of photons in the state. (b) Number of photons distibution in TMSV state for two squeezing levels: -10 dB and -15 dB (marked on subfigure (a) with a corresponding color)

where averaged photon number is given by Equation (2.17). The distribution is presented on a histogram 2.2(b), we can see that it does not have a sharp peak and we expect the truncation to be at much higher values than the mean number of photons. Indeed to reach fidelity of 95%, for the same –10 dB of squeezing, we need to keep up to 24 pairs of photons.

2.1.6 Two-mode squeezing with losses

It is well known that nonclassical states are especially prone to losses. They are inevitable in any experiment, and could be split into several categories: optical losses, inefficiencies of detectors, and discretization during the acquisition process. Achieving even –10 dB of squeezing is a challenging task. Staying in the same easy model, we can gain insight about the behaviour of TMS states in the presence of losses.

Let's assume modes $\hat{a}$ and $\hat{b}$ experience losses with coefficients η_a and η_b. We are able to include losses via the beam-splitter model. The quantum mode of interest is lost proportional to the transmittance of the beam-splitter $\sqrt{1-\eta_a}$. Instead of the lost mode a portion of vacuum is admixed from the free port. For the sake of convenience we will stay in the Heisenberg picture. The initial wavefunction for modes $\hat{a}$ and $\hat{b}$ is in the TMSV state and

operators evolve as follows:

$$\hat{a} \to \sqrt{1-\eta_a}\hat{a} + \sqrt{\eta_a}\hat{c}, \tag{2.25}$$

$$\hat{b} \to \sqrt{1-\eta_b}\hat{b} + \sqrt{\eta_b}\hat{d}. \tag{2.26}$$

Here we have assumed that absorption happens independently for both modes. We can use these modified operators to find quadratures (Eq. 2.21), which are measured by homodyne detectors in the presence of losses:

$$\hat{Q}_{\theta_a} = \frac{1}{\sqrt{2}}\left(\sqrt{1-\eta_a}\hat{a} + \sqrt{\eta_a}\hat{c}\right)e^{-i\theta_a} + \frac{1}{\sqrt{2}}\left(\sqrt{1-\eta_a}\hat{a}^\dagger + \sqrt{\eta_a}\hat{c}^\dagger\right)e^{i\theta_a}, \tag{2.27}$$

$$\hat{Q}_{\theta_b} = \frac{1}{\sqrt{2}}\left(\sqrt{1-\eta_b}\hat{b} + \sqrt{\eta_b}\hat{d}\right)e^{-i\theta_b} + \frac{1}{\sqrt{2}}\left(\sqrt{1-\eta_b}\hat{b}^\dagger + \sqrt{\eta_b}\hat{d}^\dagger\right)e^{i\theta_b}. \tag{2.28}$$

Then variances of these quadratures are averaged over the two-mode squeezed vacuum state and vacuum for the reservoir modes $|\,\phi_0\,\rangle = |\,\mathrm{TMSV}\,\rangle \otimes |\,0,0\,\rangle$:

$$\left\langle \Delta\hat{Q}^2_{\pm}\left(\theta_a,\theta_b\right)\right\rangle_{\phi_0} = \frac{\langle\,\hat{n}_{a'} + \hat{n}_{b'}\,\rangle_{\phi_0} + 1 \pm \langle\,\hat{a}'\hat{b}'e^{-i\theta} + \mathrm{h.c.}\,\rangle_{\phi_0}}{2}. \tag{2.29}$$

The nonzero terms in Equation (2.29) are

$$\langle\,\hat{a}'\hat{b}'e^{-i\theta} + \mathrm{h.c.}\,\rangle = \sqrt{(1-\eta_a)(1-\eta_b)}\langle\,\hat{a}\hat{b}\,\rangle e^{-i\theta} + \mathrm{h.c.}$$

$$\langle\,\hat{n}_{a'}\,\rangle = (1-\eta_a)\langle\,\hat{n}_a\,\rangle, \quad \langle\,\hat{n}_{b'}\,\rangle = (1-\eta_b)\langle\,\hat{n}_b\,\rangle.$$

As the result we have the quadrature variance:

$$\langle\,\Delta\hat{Q}^2_{\pm}(\theta_a,\theta_b)\,\rangle_{\phi_0} = \frac{1}{2}\frac{1+\epsilon^2(1-\eta_a-\eta_b) \mp 2\epsilon\sqrt{(1-\eta_a)(1-\eta_b)}\cos(\theta_a+\theta_b)}{1-\epsilon^2}. \tag{2.30}$$

Losses effect both squeezing and antisqueezing levels as shown in Figure 2.3.

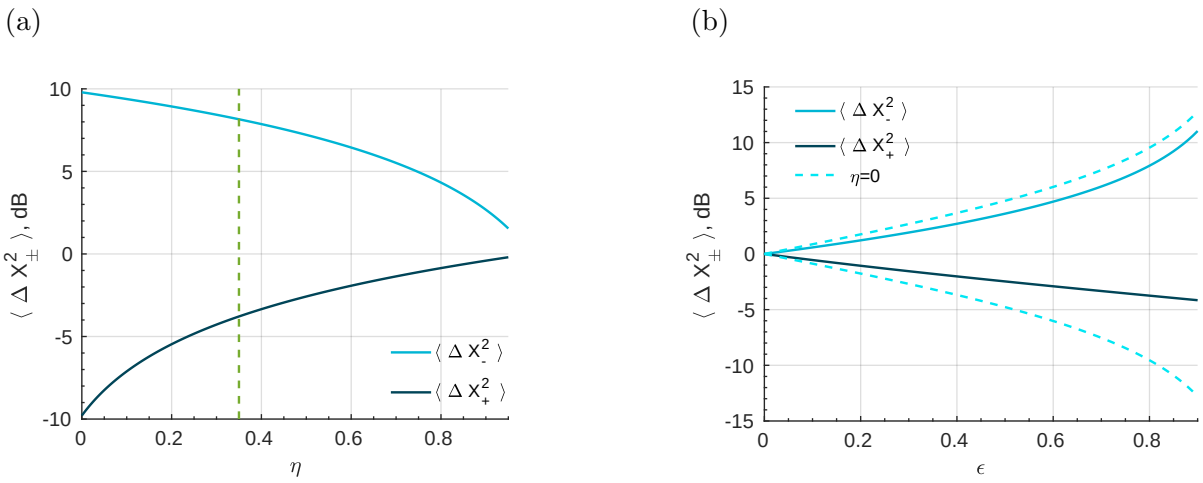

Figure (2.3) Losses included as a simple beam-splitter model. (a) We show how the squeezing and antisqueezing levels depend on losses η for the parametric gain $\epsilon = 0.81$. The green dashed line demonstrates $\eta = 35\%$ level. (b) Losses are close to experimental 35% for each channel. Dashed lines demonstrate squeezing and antisqueezing levels without losses.

2.2 Optical parametric oscillator

As it is seen from the analysis above, the maximum reduction of the quantum noise $\frac{1-\epsilon}{1+\epsilon}$ is limited by the nonlinearity coefficient, power of the pump, and length of the crystal. The nonlinear coefficient is limited by crystal structure and is difficult to maximize. The pump power can be increased up to the damage threshold of the crystal, e.g., ~ 10 GW/cm^2 for BBO, but thermal effects may limit practical power even lower. Similar practical issues rise with the length of the crystal: the non-uniformity in the growth limits the length to several centimeters.

One way to overcome this problem is to use a multiple-pass configuration, where n passes of the same pump pulse through the nonlinear media are employed. It is equivalent to n actions of squeezer operator (2.4) on the original vacuum input. This increases the effective nonlinearity and subsequent squeezing by n times, as though the media is n times longer. The ultimate multiple-pass configuration is realized when the crystal is placed in an optical resonator, which is resonant with signal and idler modes. Effectively this configuration is equivalent to multiple pass with the number of passes equal to the finesse of the cavity. This configuration—nonlinear crystal in a cavity—is usually called an optical parametric oscillator

(OPO). Before describing the atomic OPO, we would like to describe the conventional two-mode OPO and get some intuition on its operational regimes, which we will later relate to the atomic OPO.

2.2.1 Equations of motion

The effective Hamiltonian for parametric amplification of two resonator modes below the threshold can be written as [61]

$$\hat{\mathcal{H}} = \hbar\omega_{\mathrm{c}} a_1^\dagger a_1 + \hbar\omega_{\mathrm{c}} a_2^\dagger a_2 + i\hbar\left(\chi^* a_1 a_2 - \chi a_1^\dagger a_2^\dagger\right), \tag{2.31}$$

where the phase-matching condition and energy conservation must hold. The gain is assumed to be very broadband ($\chi(\omega)$ is constant for large region of ω). The dynamics of optical modes is described by Heisenberg equations of motion in a rotating frame with carrier frequency ω_{c}. The cavity is assumed to be a single-sided. We can write the Heisenberg-Langevin equations for the cavity field operators:

$$\dot{a}_1 = -\chi a_2^\dagger - \frac{\kappa + \kappa_{\mathrm{in}}}{2} a_1 + \sqrt{\kappa} a_{1,\mathrm{in}} + \sqrt{\kappa_{\mathrm{in}}}\hat{F}_1, \tag{2.32}$$

$$\dot{a}_2^\dagger = -\chi^* a_1 - \frac{\kappa + \kappa_{\mathrm{in}}}{2} a_2^\dagger + \sqrt{\kappa} a_{2,\mathrm{in}}^\dagger + \sqrt{\kappa_{\mathrm{in}}}\hat{F}_2^\dagger, \tag{2.33}$$

where κ corresponds to the energy decay per time unit through the input mirror, while κ_{in} corresponds to internal losses in the cavity, e.g. the energy decay of cavity mode per unit of time via all process except leakage through the entering mirror, and $\hat{F}_{1,2}$ are two delta-correlated Langevin noise operators, which are included to fulfill the fluctuation-dissipation theorem [53]. The Langevin noise operators have the single component correlator $\langle\, \hat{F}_{n,m}(t) \,\rangle = 0$ and the two times correlator $\langle\, \hat{F}_n(t)\hat{F}_m^\dagger(t') \,\rangle = \delta_{nm}\delta(t-t')$ and $\langle\, \hat{F}_n^\dagger(t)\hat{F}_m(t') \,\rangle = 0$. We perform a Fourier transform $a_1(t) = \int a_1(\omega)e^{-i\omega t}d\omega$, $a_2^\dagger(t) = \int a_2^\dagger(-\omega)e^{-i\omega t}d\omega$. The solution of this

linear system of equations:

$$a_1(\omega) = \frac{\left(i\omega - \frac{\kappa+\kappa_{\rm in}}{2}\right)}{\Delta_{\rm d}}\left(\sqrt{\kappa}a_{1,\rm in}(\omega) + \sqrt{\kappa_{\rm in}}\hat{F}_1(\omega)\right) + \\ + \frac{\chi\left(\sqrt{\kappa}a^\dagger_{2,\rm in}(-\omega) + \sqrt{\kappa_{\rm in}}\hat{F}^\dagger_2(-\omega)\right)}{\Delta_{\rm d}}, \tag{2.34}$$

$$a^\dagger_2(-\omega) = \frac{\left(i\omega - \frac{\kappa+\kappa_{\rm in}}{2}\right)}{\Delta_{\rm d}}\left(\sqrt{\kappa}a^\dagger_{2,\rm in}(-\omega) + \sqrt{\kappa_{\rm in}}\hat{F}^\dagger_2(-\omega)\right) + \\ + \frac{\chi^*\left(\sqrt{\kappa}a_{1,\rm in}(\omega) + \sqrt{\kappa_{\rm in}}\hat{F}_1(\omega)\right)}{\Delta_{\rm d}}, \tag{2.35}$$

where the denominator is $\Delta_{\rm d} = |\,\chi\,|^2 - (i\omega - \frac{\kappa+\kappa_{\rm in}}{2})^2$. We use input-output cavity coupling relationships $a_{\rm out} = \sqrt{\kappa}a - a_{\rm in}$ to obtain the reflected field for both modes:

$$a_{1,\rm out}(\omega) = -\,a_{1,\rm in}(\omega)\frac{|\,\chi\,|^2 + \omega^2 + \frac{\kappa^2-\kappa^2_{\rm in}}{4} + i\omega\kappa_{\rm in}}{\Delta_{\rm d}} + \frac{\chi\kappa a^\dagger_{2,\rm in}(-\omega)}{\Delta_{\rm d}} \\ + \sqrt{\kappa\kappa_{\rm in}}\frac{(i\omega - \frac{\kappa+\kappa_{\rm in}}{2})\hat{F}_1(\omega) + \chi\hat{F}^\dagger_2(-\omega)}{\Delta_{\rm d}}, \tag{2.36}$$

$$a^\dagger_{2,\rm out}(-\omega) = -\,a^\dagger_{2,\rm in}(-\omega)\frac{|\,\chi\,|^2 + \omega^2 + \frac{\kappa^2-\kappa^2_{\rm in}}{4} + i\omega\kappa_{\rm in}}{\Delta_{\rm d}} + \frac{\chi^*\kappa a_{1,\rm in}(\omega)}{\Delta_{\rm d}} \\ + \sqrt{\kappa\kappa_{\rm in}}\frac{(i\omega - \frac{\kappa+\kappa_{\rm in}}{2})F^\dagger_2(-\omega) + \chi^*\hat{F}_1(\omega)}{\Delta_{\rm d}}. \tag{2.37}$$

This analytical solution could be used to find any correlators of interest, as an example we find the intensity spectrum and variances of quadratures.

2.2.2 Observables

We can find some experimentally measured parameters, such as the energy spectrum of generated photons in each mode for an input vacuum. For this purpose we first calculate

the total number of photons in time domain within a single given cavity mode

$$\langle\, n_{1(2),\mathrm{out}} \,\rangle = \langle\, a^{\dagger}_{1(2),\mathrm{out}}(t) a_{1(2),\mathrm{out}}(t) \,\rangle = \\ = \iint d\omega' d\omega \langle\, a^{\dagger}_{1(2),\mathrm{out}}(-\omega') a_{1(2),\mathrm{out}}(\omega) \,\rangle_{\mathrm{vac}} e^{-i(\omega'+\omega)t}. \tag{2.38}$$

By taking into account the commutation relations $[a_{1(2),\mathrm{out}}(\omega), a^{\dagger}_{1(2),\mathrm{out}}(\omega')] = \delta(\omega - \omega')$ between the annihilation and creation operators in frequency domain Equation (2.38) can be simplified to

$$\langle\, n_{1,\mathrm{out}} \,\rangle_{\mathrm{vac}} = \langle\, n_{2,\mathrm{out}} \,\rangle_{\mathrm{vac}} = \int d\omega \frac{|\,\chi\,|^2 \kappa(\kappa + \kappa_{\mathrm{in}})}{\left|\, |\,\chi\,|^2 - (i\omega - \frac{\kappa+\kappa_{\mathrm{in}}}{2})^2 \,\right|^2}. \tag{2.39}$$

The resulted expression under the integral is the spectrum of generated photons at the output of the given cavity mode. It follows a Lorentzian-like shape. The number of photons decreases as a result of an increase of internal losses in the cavity. At the central frequency with respect to a cavity $\omega = 0$ this function has a singular point: $\frac{\kappa+\kappa_{\mathrm{in}}}{2} = \chi$, which corresponds to an infinite growth of number of photons (Fig. 2.4(a)). This is called a threshold condition for a parametric oscillator. For further analysis the regime above the threshold requires including dynamics of pumps. The generation of an infinite number of photons depletes the pumps and χ does not stay constant.

Another observable we are considering characterizes nonclassical correlations of the emitted photons. This nonclassicality is revealed in the variance of the generalized sum and difference quadratures operator:

$$\hat{X}_{\pm}(\omega, \theta_1, \theta_2) = \frac{a_{1,\mathrm{out}}(\omega) e^{-i\theta_1} + a^{\dagger}_{1,\mathrm{out}}(-\omega) e^{i\theta_1} \pm a_{2,\mathrm{out}}(\omega) e^{-i\theta_2} \pm a^{\dagger}_{2,\mathrm{out}}(-\omega) e^{i\theta_2}}{\sqrt{2}}, \tag{2.40}$$

where phases θ_1 and θ_2 set the specific canonical quadrature. Experimentally it is controlled by the phase of the local oscillator. Variance of this operator averaged over the vacuum state

(a) (b)

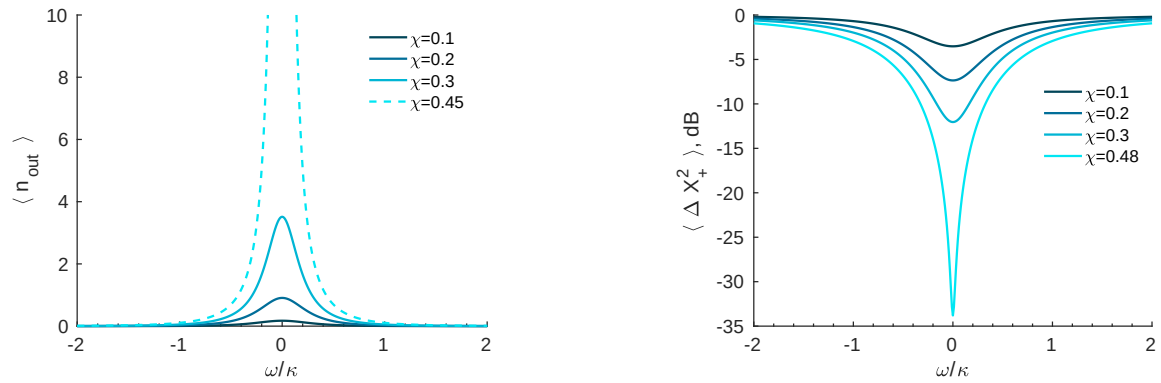

Figure (2.4) Spectrum of averaged number of photons (a) and squeezing spectrum (b) depending on the gain χ. All frequencies are normalized by the cavity linewidth κ=1, gain χ is frequency independent, no internal losses $\kappa_{\text{in}} = 0$. (a) Dashed line is a generation near threshold $\frac{\kappa}{2} \approx \chi$. (b) Spectrum of squeezing for the phases $\theta_1 + \theta_2 = 0$. As the gain approaches threshold $\frac{\kappa}{2} \approx \chi$ squeezing becomes infinitely high with a narrow linewidth

is

$$\begin{aligned}\langle \Delta\hat{X}_{\pm}^2 \rangle =& \frac{\left(|\chi|^2 + \omega^2 + \frac{\kappa^2-\kappa_{\text{in}}^2}{4}\right)^2 + \kappa_{\text{in}}^2\omega^2 + \kappa^2|\chi|^2}{|\Delta_{\text{d}}|^2} \mp \\ &\mp \frac{2\kappa}{|\Delta_{\text{d}}|^2}\left(|\chi|^2 + \omega^2 + \frac{\kappa^2-\kappa_{\text{in}}^2}{4}\right)\Re e(\chi e^{-i(\theta_1+\theta_2)}) + \\ &+ \kappa\kappa_{\text{in}}\frac{|\chi|^2 + \omega^2 + (\frac{\kappa+\kappa_{\text{in}}}{2})^2 \mp (\kappa+\kappa_{\text{in}})\Re e(\chi e^{-i(\theta_1+\theta_2)})}{|\Delta_{\text{d}}|^2}. \end{aligned} \tag{2.41}$$

and it depends on the phases of the quadratures we are interested in. Mathematically the perfect squeezing is observed if the threshold condition is fulfilled, as an infinite number of photons in the signal and idler modes is generated. The spectrum of generated photons and squeezing spectrum narrows as gain approaches the threshold condition (Fig. 2.4).

In the previous system of equations $\chi(\omega)$ is constant for a large region of ω, which is not fulfilled in the case of atomic systems. Thus we modify χ to depend on ω and have a finite bandwidth. The simplest two-level atom has an imaginary part of susceptibility with a Lorentzian shape $\chi = \frac{\chi_0}{(\omega-\omega_0)^2+\gamma_0^2/4}$. We phenomenologically include it into our solution, Equation (2.39), instead of constant χ, then the spectrum of generated photons narrows

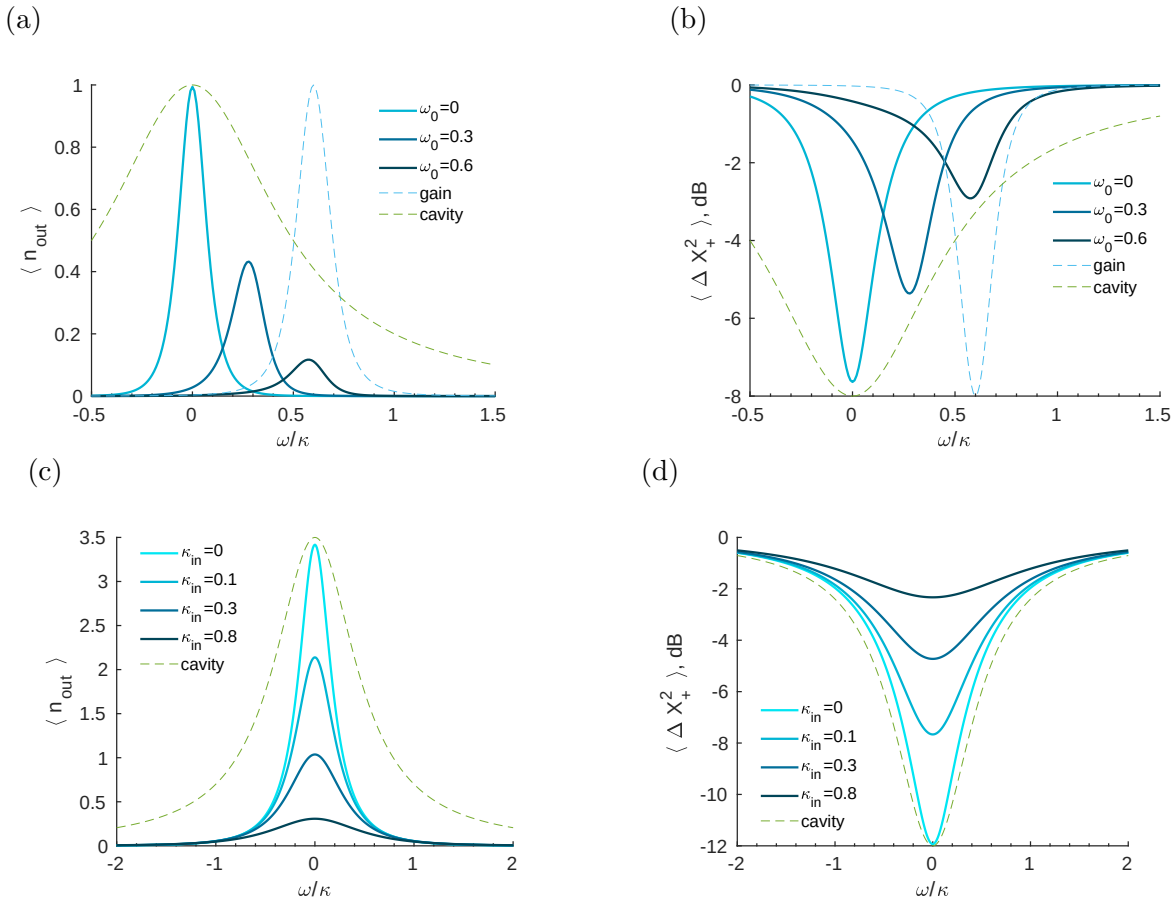

Figure (2.5) Spectrum of averaged number of photons (a) and (c) and squeezing spectrum (b) and (d). All frequencies are normalized by the cavity linewidth κ=1, gain χ is frequency dependent. The dashed lines show normalized gain (blue) and cavity (green) linewidths. (a)–(b) χ is a Lorentzian function of frequency ω with parameters $\gamma_0 = 0.3$ and $\epsilon_0 = 5 \cdot 10^{-3}$. We shift the central frequency of the gain with respect to the cavity to the right by an amount of ω_0 displayed in the legend. Internal losses are zero $\kappa_{\text{in}} = 0$. (c)–(d) Dependence on internal losses. The central frequency of the gain is kept the same as for the cavity.

down only to the gain bandwidth of the OPO (Fig. 2.5(a)). If we mismatch the central frequencies of the cavity and gain spectrum it will result in asymmetric generation and a significant decrease in generated rate, and an asymmetric squeezing spectrum (Fig. 2.5(b)).

2.3 Cavity quantum electrodynamics

To develop a theory of an atomic based optical parametric oscillator we first review the basic quantum theory of light-atom interaction. Secondly, we apply this theory to N two-level atoms interacting with the cavity mode. We analyze how the reflection of the input light from the cavity changes depending on experimental conditions, such as detunings, cooperativity, and intensity of the input field. This model enables us to estimate the number of atoms interacting with the cavity from the reflection spectrum, which is a valuable parameter for an atomic based optical parametric oscillator, as we will see later.

2.3.1 Light-atom interaction

We approximate the interaction of an atom with a single optical mode as an interaction of a quantum two-level system and a bosonic mode. A two-level system as being equivalent to spin 1/2 can be described by Pauli operators with canonical commutation relationship $[\hat{S}_i, \hat{S}_j] = 2i\epsilon_{ijk}\hat{S}_k$, where ϵ_{ijk} is a Levi-Civita tensor and indices (i, j, k) are integer values from one to three. The electromagnetic mode is described by creation and annihilation operators $[\hat{a}, \hat{a}^\dagger] = 1$.

The energy of the atomic transition is assumed to be $\hbar\omega_\mathrm{a}$, while the cavity has resonant frequency ω_c. The free Hamiltonian of noninteracting two-level atom and the cavity takes the following form:

$$\hat{H}_0 = \hbar\omega_\mathrm{c}\hat{a}^\dagger\hat{a} + \frac{\hbar\omega_\mathrm{a}}{2}\hat{S}_z. \tag{2.42}$$

The interaction can be decomposed into the cavity-atom coupling and interaction between

cavity and external driving field. We consider a dilute gas, where atoms do not interact with each other. The light-matter interaction is well described by the dipole approximation, if the central wavelength of the electro-magnetic field is much larger than the size of an atom [53, Ch. 5]. As an example, the typical sizes of alkali atoms are 3–5 Bohr radii, on the other hand the transition wavelenths lie in the range of 670–850 nm, so the condition is fulfilled.

$$\hat{V}_{\mathrm{ac}} \approx -\hat{\boldsymbol{E}} \cdot \hat{\boldsymbol{d}} = \sqrt{\frac{2\pi\hbar\omega_{\mathrm{c}}}{V}}(\hat{a}^{\dagger}e^{i\omega_{\mathrm{c}}t - i\boldsymbol{k}\boldsymbol{r}} - \hat{a}e^{-i\omega_{\mathrm{c}}t + i\boldsymbol{k}\boldsymbol{r}})\left(d_{12}\hat{S}_{21} + d_{12}^{*}\hat{S}_{12}\right), \tag{2.43}$$

here $\hat{S}_{21} = \frac{\hat{S}_x + i\hat{S}_y}{2} = |\,2\,\rangle\langle\,1\,|$ and $\hat{S}_{12} = \frac{\hat{S}_x - i\hat{S}_y}{2} = |\,1\,\rangle\langle\,2\,|$ are the atomic transition operators and $d_{12} = \langle\,2\,|\,\boldsymbol{r}\cdot\boldsymbol{e}\,|\,1\,\rangle$ is the matrix element of the electric dipole moment, $\boldsymbol{e}$ is a light polarization vector, V is a cavity volume, $\boldsymbol{r}$ is a vector pointing from the origin to the atom.

The first step is to use the rotating-wave approximation (RWA), where energy non-conserving operator products are disregarded [53, Ch. 5]. In particular, in Equation (2.43) the terms proportional to $\hat{a}^{\dagger}\hat{S}_{21}$ and $\hat{a}\hat{S}_{12}$ are neglected, this is valid if an effective coupling constant is smaller than the transition frequency $g = \sqrt{\frac{2\pi\hbar\omega_{\mathrm{c}}}{V}}\,|\,d_{12}\,| \ll \omega_{\mathrm{a}}$, which is the case for optical dipole transitions. The best fiber-resonator achieves the coupling constant of 100 MHz [62], which is negligible in comparison with the optical transition.

Secondly, to make the Hamiltonian independent of oscillatory terms we can introduce a rotating frame with the driving frequency ω_{d}. The Hamiltonian in the rotating frame can be derived through the following unitary transformation [59]:

$$\hat{H}_{\mathrm{rf}} = \hat{U}\left(\hat{H}_0 + \hat{V}_{\mathrm{ac}}\right)\hat{U}^{\dagger} + i(\partial_t\hat{U})\hat{U}^{\dagger}, \tag{2.44}$$

where this unitary transformation represents the rotations of atoms with the cavity frequency, and rotations of the cavity with the external driving field:

$$\hat{U} = \exp\left(\frac{i\omega_{\mathrm{c}}t}{2}\hat{S}_z\right)\exp\left(i\omega_{\mathrm{d}}t\hat{a}^{\dagger}\hat{a}\right). \tag{2.45}$$

By applying the Baker-Campbell-Hausdorff formula

$$e^{i\lambda\hat{G}}\hat{A}e^{-i\lambda\hat{G}} = \hat{A} + i\lambda[\hat{G},\hat{A}] + \frac{(i\lambda)^2}{2!}[\hat{G}[\hat{G},\hat{A}]] + \cdots \tag{2.46}$$

and in the rotating frame the Hamiltonian has the form:

$$\hat{H}_{\mathrm{rf}} = \frac{\Delta}{2}\hat{S}_z + \delta\hat{a}^\dagger\hat{a} + g(\hat{a}\hat{S}_{21}e^{ikr} + \hat{a}^\dagger\hat{S}_{12}e^{-ikr}), \tag{2.47}$$

where $\Delta = \omega_{\mathrm{a}} - \omega_{\mathrm{c}}$, $\delta = \omega_{\mathrm{c}} - \omega_{\mathrm{d}}$ are the cavity-atom and cavity-driving field detunings. The Hamiltonian (2.47) is solvable for a single atom [53] and its solution describes a plethora of phenomena, such as vacuum Rabi splitting, collapse and revivals, etc.

2.3.2 N atoms

The Hamiltonian (2.47) is easily generalized for N identical atoms by summing over all j-th indices. However, it is convenient to use collective spin operators $\hat{S}^+ = \frac{1}{\sqrt{N}}\sum_{j=1}^{N} e^{ikr_j}\hat{S}_{21}^j$ and $\hat{S}^z = \frac{1}{N}\sum_{j=1}^{N}\hat{S}_z^j$, which obey commutation relations [63]:

$$\left[\hat{S}^+,\hat{S}^-\right] = \hat{S}^z, \quad \left[\hat{S}^\pm,\hat{S}^z\right] = \pm\frac{2}{N}\hat{S}^\pm. \tag{2.48}$$

The Hamiltonian (2.47) in these new notations is

$$\hat{H} = \frac{N\Delta}{2}\hat{S}^z + \delta\hat{a}^\dagger\hat{a} + \sqrt{N}g\left(\hat{a}\hat{S}^+ + \hat{a}^\dagger\hat{S}^-\right). \tag{2.49}$$

As we can see from this Hamiltonian, coherent interaction of N atoms provides an enhancement for coupling strength by a factor of $\sqrt{N}$. The equations of motion for given operator $\hat{A}$ can be written taking into account dissipative effects such as spontaneous emission and

losses in the cavity using a master equation type approach [64]:

$$\frac{d}{dt}\langle\,\hat{A}\,\rangle = \mathrm{Tr}\left(\hat{A}\frac{d\rho}{dt}\right) = \mathrm{Tr}\left(\hat{A}\left(-i[\hat{H},\rho] + \hat{L}\rho\right)\right), \tag{2.50}$$

where the so-called Lindblad term $\hat{L}\rho$ represents atomic coherence decay due to radiative spontaneous emission γ and cavity parasitic losses κ_{in}:

$$\hat{L}\rho = \gamma\sum_{j=1}^{N}\left(\hat{S}_{12}^{j}\rho\hat{S}_{21}^{j} - \frac{1}{2}\left(\hat{S}_{21}^{j}\hat{S}_{12}^{j}\rho + \rho\hat{S}_{21}^{j}\hat{S}_{12}^{j}\right)\right) + \kappa_{\mathrm{in}}\left(\hat{a}\rho\hat{a}^{\dagger} - \frac{1}{2}\left(\hat{a}^{\dagger}\hat{a}\rho + \rho\hat{a}^{\dagger}\hat{a}\right)\right). \tag{2.51}$$

It is a reasonable assumption for a dilute cold gas of neutral atoms such as rubidium or other alkali atoms that we are able to limit decoherence by the radiative decay [65].

The cavity coupling with the driving field is expressed through the beam-splitter type of interaction. A cavity with a high enough finesse can be treated through the input-output formalism [61]. Taking into account the Lindblad term and the input-output relationship for the cavity the equations of motion (2.50) for collective atomic coherence, population operators, and cavity modes are derived with help of permutation under the trace without any additional assumptions:

$$\frac{d\langle\,\hat{S}^{-}\,\rangle}{dt} = -i(\Delta - i\gamma/2)\langle\,\hat{S}^{-}\,\rangle + i\sqrt{N}g\langle\,\hat{a}\hat{S}^{z}\,\rangle \tag{2.52}$$

$$\frac{d\langle\,\hat{a}\,\rangle}{dt} = -i(\delta - i(\kappa+\kappa_{\mathrm{in}})/2)\langle\,\hat{a}\,\rangle - i\sqrt{N}g\langle\,\hat{S}^{-}\,\rangle + \sqrt{\kappa}\langle\,\hat{a}_{\mathrm{in}}\,\rangle \tag{2.53}$$

$$\frac{d\langle\,\hat{S}^{z}\,\rangle}{dt} = -\gamma(\langle\,\hat{S}^{z}\,\rangle + 1) - i\frac{2g}{\sqrt{N}}\left(\langle\,\hat{a}\hat{S}^{+}\,\rangle - \langle\,\hat{a}^{\dagger}\hat{S}^{-}\,\rangle\right) \tag{2.54}$$

$$\hat{a}_{\mathrm{in}} + \hat{a}_{\mathrm{out}} = \sqrt{\kappa}\hat{a} \tag{2.55}$$

The presented equations describe interaction of the cavity mode with an ensemble of non-interacting two-level atoms. For the exact solution we need to write an infinite system of couple equations, as nonlinear terms $\langle\,\hat{a}\hat{S}^{+}\,\rangle$ and $\langle\,\hat{a}^{\dagger}\hat{S}^{-}\,\rangle$ require additional equations, which will not make the system complete. Below we truncate the chain under the assumption of a

weak classical probe $\langle\, \hat{a}\hat{S}^{+}\,\rangle \approx \langle\, \hat{a}\,\rangle\langle\, \hat{S}^{+}\,\rangle$, $\langle\, \hat{a}^{\dagger}\hat{S}^{-}\,\rangle \approx \langle\, \hat{a}^{\dagger}\,\rangle\langle\, \hat{S}^{+}\,\rangle$ [66]. It means, that we are neglecting the entanglement between light and matter.

2.3.3 Weak probing

We probe atoms with a weak coherent field by sending it through the cavity mode. For the classical field we change the field operators in the system of equations (2.52)–(2.55) for the complex numbers and search for a steady-state solution ($\langle\, \hat{a}\,\rangle = \alpha$ and $\langle\, \hat{a}_{\mathrm{in(out)}}\,\rangle = \alpha_{\mathrm{in(out)}}$):

$$-i(\Delta - i\gamma/2)\langle\, \hat{S}^{-}\,\rangle + i\sqrt{N}g\alpha\langle\, \hat{S}^{z}\,\rangle = 0 \tag{2.56}$$

$$(-i\delta - \kappa/2 - \kappa_{\mathrm{in}}/2)\alpha - i\sqrt{N}g\langle\, \hat{S}^{-}\,\rangle + \sqrt{\kappa}\alpha_{\mathrm{in}} = 0 \tag{2.57}$$

$$-\gamma(\langle\, \hat{S}^{z}\,\rangle + 1) - i\frac{2g}{\sqrt{N}}\left(\alpha\langle\, \hat{S}^{+}\,\rangle - \alpha^{*}\langle\, \hat{S}^{-}\,\rangle\right) = 0 \tag{2.58}$$

$$\alpha_{\mathrm{in}} + \alpha_{\mathrm{out}} = \sqrt{\kappa}\alpha \tag{2.59}$$

We resolve this system of equations (2.56)–(2.58) and find the expectation values of atomic operators:

$$\langle\, \hat{S}^{z}\,\rangle = -\frac{1}{\frac{2g^{2}|\,\alpha\,|^{2}}{\Delta^{2}+\gamma^{2}/4} + 1} \quad \text{and} \quad \langle\, \hat{S}^{-}\,\rangle = -\frac{\sqrt{N}g\alpha}{(\Delta - i\gamma/2)\left(\frac{2g^{2}|\,\alpha\,|^{2}}{\Delta^{2}+\gamma^{2}/4} + 1\right)}. \tag{2.60}$$

Substituting expressions (2.60) in the same system (2.56)–(2.58) we obtain an equation for the field inside the cavity:

$$(i\delta + \kappa/2 + \kappa_{\mathrm{in}}/2)\alpha - i\frac{Ng^{2}}{(\Delta - i\gamma/2)\left(\frac{2g^{2}|\,\alpha\,|^{2}}{\Delta^{2}+\gamma^{2}/4} + 1\right)}\alpha = \sqrt{\kappa}\alpha_{\mathrm{in}}. \tag{2.61}$$

The second term on the left hand side carries information about nonlinear susceptibility of two-level atoms. This equation is nonlinear and could be linearized assuming a weak input

light in comparison with atomic saturation intensity or $I_c \sim g^2 \mid \alpha \mid^2 \ll \gamma^2/2$ [3]. The linearized solution for the field inside a cavity is

$$\alpha \approx \frac{\sqrt{\kappa}\alpha_{\text{in}}}{(i\delta + \kappa/2 + \kappa_{\text{in}}/2) - i\frac{Ng^2}{(\Delta - i\gamma/2)}}. \tag{2.62}$$

In the experiment we measure the intensity of the reflected field, for this reason we find the field outside of the cavity in terms of the incident field by applying the input-output formalism (2.59). After mathematical simplifications we can write the ratio between reflected $I_{\text{out}} \propto |\alpha_{\text{out}}|^2$ and incident $I_{\text{in}} \propto |\alpha_{\text{in}}|^2$ intensities as:

$$\frac{I_{\text{out}}}{I_{\text{in}}} = 1 - \frac{\frac{4C(\epsilon\kappa+1)}{(1+4\Delta^2/\gamma^2)} + \epsilon\kappa}{(\epsilon\kappa+1)^2\left(\left(\frac{\delta}{\kappa+\kappa_{\text{in}}} - \frac{4C\Delta}{\gamma(1+4\Delta^2/\gamma^2)}\right)^2 + \frac{1}{4}\left(\frac{4C}{1+4\Delta^2/\gamma^2}+1\right)^2\right)} \tag{2.63}$$

where $\epsilon\kappa = \frac{\kappa_{\text{in}}}{\kappa}$, $C = \frac{Ng^2}{(\kappa+\kappa_{\text{in}})\gamma}$ is a cooperativity parameter. The cooperativity parameter characterizes the strength of collective atom-cavity interaction. Its definition could vary from source to source by a multiplicative factor, although the essence stays: it is an enhancement factor for emission into the cavity multiplied by a number of atoms of N. From its definition we can say that it is a ratio between coherent and incoherent processes for an atom interacting with cavity mode.

As we can see from denominator of (2.63) the presence of atoms acts in the following manner:

1. Atomic spectral dispersion shifts the cavity resonance with respect to the bare one by $\frac{4C\Delta}{\gamma(1+4\Delta^2/\gamma^2)}$ in the units of cavity linewidth κ.

2. Meanwhile, absorption of light by atoms broadens the cavity resonance by an additional factor of $\frac{C}{1+4\Delta^2/\gamma^2}$ again in the units of κ.

[3] In the case of Rubidium 87 the saturation intensity is $I_{\text{sat}} = 4.484$ mW/cm^2 $= 0.048$ nW/μm^2 [67]. The light is focused into 100 μm, which is the cavity waist. Thus the saturation power is 1.4 μW. The result should be additionally divided by a finesse of the cavity, which amplifies internal signal. In our experiment finesse is 100 and the resulting power is 14 nW.

The dependence of the reflected intensity on cooperativity is most clearly seen for the resonance condition for atoms, cavity, and driving field ($\delta = 0$, $\Delta = 0$) and for the small internal losses ($\epsilon\kappa \ll 1$), then the ratio (2.63) is approximated by

$$\frac{I_{\rm out}}{I_{\rm in}} \approx 1 - \frac{4C}{(1+C)^2}. \tag{2.64}$$

We could imagine that we vary cooperativity by adding more atoms into the cavity mode. We begin with a bare cavity, when the total field is reflected ($I_{\rm out} = I_{\rm in}$). With an increase of atom number the cooperativity reaches the value $C = 1$, when the input field fully enters the cavity ($I_{\rm out} = 0$). This is so-called impedance matching, which we discuss in more detail in Section 4.4. With the further increase of atom's number reflected field asymptotically increases to $I_{\rm in}$ at large cooperativity. The same qualitative behaviour happens at nonzero detuning and internal losses with the corresponding spectral corrections.

2.4 Two-mode squeezing in a cavity

In Section 2.2 we worked in a semiclassical model, where we kept the fields quantized in order to study their nonclassical properties. Even richer dynamics are guided by a quantized three-level atom, e.g., atomic population trapping [53], electromagnetically-induced transparency (EIT) [68]. To quantify the effects of finite gain bandwidth and dispersion of three-level atoms we have to construct a theory that includes both the atomic dynamics and quantum properties of light.

2.4.1 System

We are considering an ensemble of N atoms with energetic levels forming a Λ scheme, which is presented in Figure 2.6. Two metastable levels $|\,1\,\rangle$ and $|\,2\,\rangle$ are coupled to the upper excited state $|\,3\,\rangle$ by two coherent pump fields with Rabi frequencies Ω_1 and Ω_2 and central frequencies $\omega_{\rm c1}$ and $\omega_{\rm c2}$. These fields have different detunings Δ_2 and Δ_1 from the

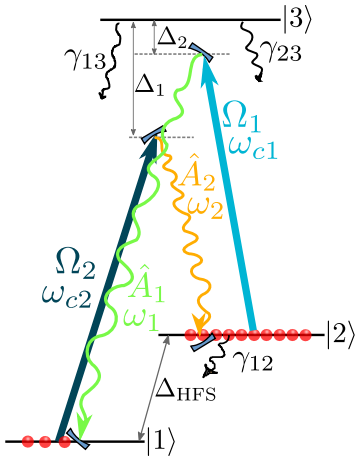

Figure (2.6) The Λ-type atomic structure with all fields involved in the FWM process. The three-level atoms have two metastable levels $|\,1\,\rangle$ and $|\,2\,\rangle$. The excited state $|\,3\,\rangle$ decays with the rates γ_{13} and γ_{23}. Two optical pumps Ω_1 and Ω_2 induce FWM process, where two quantum fields $\hat{A}_1$ and $\hat{A}_2$ are emitted into the cavity modes. FWM process is non-degenerate, since two pumps have two different detunings Δ_2 and Δ_1 from the upper level.

atomic resonance and thus induce a non-degenerate FWM process. The two quantized fields generated as a result have two new central frequencies ω_1 or ω_2, which in turn are two longitudinal modes of one cavity. The annihilation operators of these intracavity fields are $\hat{A}_1$ and $\hat{A}_2$.

Together with the creation of photons in the cavity modes, the atoms will transition from level to level. To build our model we introduce an atomic projection operator $\hat{S}^j_{nm} = |\,n\,\rangle^j\,\langle\,m\,|^j$, which transfers the j-th atom from level $|\,m\,\rangle$ onto level $|\,n\,\rangle$. The summation of this operator over all atoms in an ensemble gives the population of a level of interest $\sum_j \hat{S}^j_{nn}$ and a macroscopic dipole moment $\sum_j \hat{S}^j_{nm}$. Atoms interact with light via the dipole interaction, as was discussed in Subsection 2.3.1, the dipole allowed transitions are $|\,1\,\rangle \leftrightarrow |\,3\,\rangle$ and $|\,2\,\rangle \leftrightarrow |\,3\,\rangle$. All of the above together with the rotating-wave approximation [53, Ch. 5]

brings us to a Hamiltonian of the form:

$$\begin{aligned}\hat{\mathcal{H}} =&\hbar\omega_1\hat{A}_1^\dagger\hat{A}_1 + \hbar\omega_2\hat{A}_2^\dagger\hat{A}_2 + \hbar\sum_j\left(\omega_{33}\hat{S}_{33}^j + \omega_{22}\hat{S}_{22}^j + \omega_{11}\hat{S}_{11}^j\right) + \\ &+ \hbar\sum_j\left(\hat{S}_{31}^j(g_1^j\hat{A}_1 + \Omega_2 e^{-i\omega_{c2}t}) + \hat{S}_{32}^j(g_2^j\hat{A}_2 + \Omega_1 e^{-i\omega_{c1}t})\right) + \text{h.c.}\end{aligned} \tag{2.65}$$

The sum is taken over all atoms in the ensemble. In addition to the coherent dynamics described by the Hamiltonian (2.65), incoherent processes take place. The state $|\,3\,\rangle$ can radiatively decay to $|\,1\,\rangle$ and $|\,2\,\rangle$ with the corresponding decay rates γ_{13} and γ_{23}, while the coherence between levels $|\,1\,\rangle$ and $|\,2\,\rangle$ exhibits dephasing at the rate γ_{12}.

2.4.2 Equations of motion

To include the decoherence we apply the Heisenberg-Langevin formalism [53, Ch. 9] and derive corresponding equations of motion for the atomic system:

$$\begin{aligned}\frac{d\hat{S}_{13}^j}{dt} =& -(i\omega_{13} + \gamma_{13}/2)\hat{S}_{13}^j - i(g_1^j\hat{A}_1 + \Omega_2(z_j)e^{-i\omega_{c2}t})(\hat{S}_{11}^j - \hat{S}_{33}^j) \\ &- i(g_2^j\hat{A}_2 + \Omega_1(z_j)e^{-i\omega_{c1}t})\hat{S}_{12}^j + \hat{\Phi}_{13}^j,\end{aligned} \tag{2.66}$$

$$\begin{aligned}\frac{d\hat{S}_{23}^j}{dt} =& -(i\omega_{23} + \gamma_{23}/2)\hat{S}_{23}^j - i(g_2^j\hat{A}_2 + \Omega_1(z_j)e^{-i\omega_{c1}t})(\hat{S}_{22}^j - \hat{S}_{33}^j) \\ &- i(g_1^j\hat{A}_1 + \Omega_2(z_j)e^{-i\omega_{c2}t})\hat{S}_{21}^j + \hat{\Phi}_{23}^j,\end{aligned} \tag{2.67}$$

$$\begin{aligned}\frac{d\hat{S}_{12}^j}{dt} =& -(i\omega_{12} + \gamma_{12}/2)\hat{S}_{12}^j - i(g_2^{*j}\hat{A}_2^\dagger + \Omega_1^*(z_j)e^{i\omega_{c1}t})\hat{S}_{13}^j \\ &+ i(g_1^j\hat{A}_1 + \Omega_2(z_j))e^{-i\omega_{c2}t}\hat{S}_{32}^j + \hat{\Phi}_{12}^j,\end{aligned} \tag{2.68}$$

In contrast to the Langevin noise operators used in description of the OPO (Section 2.2.1), atomic Langevin noise operators $\hat{\Phi}_{nm}$ are the product of δ correlated bosonic bath operator at zero temperature and corresponding atomic population operator. These operators are introduced in order to conserve commutation relationships for the atomic operators at all times and their properties are dictated by the fluctuation-dissipation theorem [53]. According

to the theorem the operators have zero mean values, and their second-order correlators are represented by the generalized diffusion coefficients D_{nmkl}: $\langle \hat{\Phi}^i_{nm} \hat{\Phi}^j_{kl} \rangle = \delta^i_j \delta(t-t') D_{nmkl}$ [69]. These coefficients are calculated in the rotating frame introduced further and presented in Appendix A.

For the intracavity field we write the quantum stochastic differential equations [61, Ch. 7] in the same manner as it was done for the two-level atom (Subsection 2.3.2), where the cavity losses κ enter together with a noise term in the form of the input field:

$$\frac{d\hat{A}_1}{dt} = -(i\omega_1 + \kappa/2)\hat{A}_1 - i\sum_j g_1^{*j} \hat{S}^j_{13} + \sqrt{\kappa}\hat{A}_{\text{in},1} \tag{2.69}$$

$$\frac{d\hat{A}_2}{dt} = -(i\omega_2 + \kappa/2)\hat{A}_2 - i\sum_j g_2^{*j} \hat{S}^j_{23} + \sqrt{\kappa}\hat{A}_{\text{in},2} \tag{2.70}$$

Since we have two strong control pumps and two cavity modes, it is natural to introduce two atomic coherences and two cavity modes rotating with the central frequencies of the corresponding pumps $\omega_{\text{c}1}$ and $\omega_{\text{c}2}$:

$$\hat{S}^j_{13} = \hat{R}^j_{13} e^{-i\omega_{\text{c}2}t}; \qquad \hat{S}^j_{23} = \hat{R}^j_{23} e^{-i\omega_{\text{c}1}t}; \qquad \hat{S}^j_{12} = \hat{R}^j_{12} e^{-i(\omega_{\text{c}2}-\omega_{\text{c}1})t}; \tag{2.71}$$

$$\hat{\Phi}^j_{13} = \hat{F}^j_{13} e^{-i\omega_{\text{c}2}t}; \qquad \hat{\Phi}^j_{23} = \hat{F}^j_{23} e^{-i\omega_{\text{c}1}t}; \qquad \hat{\Phi}^j_{12} = \hat{F}^j_{12} e^{-i(\omega_{\text{c}2}-\omega_{\text{c}1})t}; \tag{2.72}$$

$$\hat{A}_1 = \hat{a}_1 e^{-i\omega_{c2}t}; \qquad \hat{A}_2 = \hat{a}_2 e^{-i\omega_{c1}t}. \tag{2.73}$$

We note that two detunings Δ_1, Δ_2 are the difference between pump frequencies $\omega_{\text{c}1}$, $\omega_{\text{c}2}$ and atomic resonances ω_{13}, ω_{23}. Physically they represent one photon detuning between corresponding atomic transition and laser pumps. The detunings $\delta_{1,2}$ correspond to the mismatch between cavity mode and pump frequencies acting on the same transition, meaning

detuning from the Raman two-photon transition. These new notations are listed below:

$$\Delta_1 = \omega_{13} - \omega_{c2}; \quad \Delta_2 = \omega_{23} - \omega_{c1}; \tag{2.74}$$

$$\delta_1 = \omega_1 - \omega_{c2}; \quad \delta_2 = \omega_2 - \omega_{c1}; \tag{2.75}$$

$$\delta = \omega_{21} - \omega_{c2} + \omega_{c1} = \Delta_1 - \Delta_2. \tag{2.76}$$

We rewrite the system of equations (2.66)–(2.70) in new notations and in the rotating reference frame (2.71)–(2.73):

$$\frac{d\hat{a}_1}{dt} = -(i\delta_1 + \kappa/2)\hat{a}_1 - i\sum_j g_1^{*j}\hat{R}_{13}^j + \sqrt{\kappa}\hat{a}_{\text{in},1} \tag{2.77}$$

$$\frac{d\hat{a}_2^\dagger}{dt} = -(-i\delta_2 + \kappa/2)\hat{a}_2^\dagger + i\sum_j g_2^j\hat{R}_{32}^j + \sqrt{\kappa}\hat{a}_{\text{in},2}^\dagger \tag{2.78}$$

$$\frac{d\hat{R}_{13}^j}{dt} = -(i\Delta_1 + \gamma_{13}/2)\hat{R}_{13}^j - i(g_1^j\hat{a}_1 + \Omega_2(z_j))(\hat{R}_{11}^j - \hat{R}_{33}^j) - i\Omega_1(z_j)\hat{R}_{12}^j + \hat{F}_{13}^j \tag{2.79}$$

$$\frac{d\hat{R}_{32}^j}{dt} = (i\Delta_2 - \gamma_{23}/2)\hat{R}_{32}^j + i(g_2^{*j}\hat{a}_2^\dagger + \Omega_1^*(z_j))(\hat{R}_{22}^j - \hat{R}_{33}^j) + i\Omega_2^*(z_j)\hat{R}_{12}^j + \hat{F}_{32}^j \tag{2.80}$$

$$\frac{d\hat{R}_{12}^j}{dt} = -(i\delta + \gamma_{12}/2)\hat{R}_{12}^j - i\Omega_1^*(z_j)\hat{R}_{13}^j + i\Omega_2(z_j)\hat{R}_{32}^j + \hat{F}_{12}^j \tag{2.81}$$

We partially linearized the system of equations by neglecting nonlinear terms $\propto g_1\hat{A}_1\hat{S}_{21}^j$ and $\propto g_2\hat{A}_2\hat{S}_{12}^j$ in a comparison with terms $\Omega_2\hat{S}_{21}^j$ and $\Omega_1\hat{S}_{13}^j$, since the pumping Rabi-frequencies are larger than the Rabi frequency of the generated quantum fields ($\Omega_i \gg g_i\langle\,\hat{A}_i\,\rangle$) [70]. This condition is fulfilled if the numbers of photons in each mode is smaller than $|\,\Omega_i\,|^2\,/\,|\,g_i\,|^2$, that corresponds to $\sim 10^4$ of photons being measured[4]. These terms become important for larger signal and idler powers and are needed to be included for system operating near and above the threshold, when the pump is depleted.

To simplify further analysis, we can consider a quasistationary regime for the atomic population, where the atomic system is assumed in a steady state determined primarily by pumps Ω_1 and Ω_2 (see Appendix C.1). Since we have two strong control pumps and two

[4]The parameters used in experiment: Rabi frequencies of pumping fields 2-10 MHz and $|\,g_{1,2}\,| \sim 1$ kHz.

cavity modes, we assume that the dynamics of the system is mainly dictated by the pumps with other processes acting perturbatively. Assuming population difference operators to be real numbers $\hat{P}^j_{23} = \langle \hat{R}^j_{22} - \hat{R}^j_{33} \rangle$ and $\hat{P}^j_{11} = \langle \hat{R}^j_{11} - \hat{R}^j_{33} \rangle$, the system of equations become linear with respect to operator's powers. We should note that the approximation is valid, while the population difference is determined by the pumps, which corresponds to the conditions $|g^j_1|^2 \langle \hat{a}^\dagger_1 \hat{a}_1 \rangle \ll |\Omega_2|^2$ and $|g^j_2|^2 \langle \hat{a}^\dagger_2 \hat{a}_2 \rangle \ll |\Omega_1|^2$ and excludes the above-threshold regime. Operating in this regime allows us to find the analytic solution for the system of equations (2.77)–(2.81), therewith the experiment on TMS runs in a quasistationary regime.

2.4.3 Collective operator approach

One way to prove validity of the given above approximation of a steady-state population is to consider the exact numerical solution of the system (2.77)–(2.81). Unfortunately, the large number of atoms ($\sim 10^6$) and nonlinearity makes such calculation problematic. However if atoms experience the same coupling constants, pump Rabi frequencies, and detunings, we can use collective operators in the similar fashion as it was done for a two-level atom in Section 2.3.1. Such conditions can be realized in the travelling wave (ring) optical cavity [71] with pumps having large beam cross-section to exclude nonuniformity of the pumping beams. Following the analogy, we introduce normalized collective coherence operators and normalized collective population operators:

$$\hat{R}_{13} = \frac{1}{\sqrt{N}} \sum_{j=1}^{N} \hat{R}^j_{13} e^{-i\boldsymbol{k}_1 \boldsymbol{r}_j}, \qquad \hat{R}_{32} = \frac{1}{\sqrt{N}} \sum_{j=1}^{N} \hat{R}^j_{32} e^{i\boldsymbol{k}_2 \boldsymbol{r}_j}, \tag{2.82}$$

$$\hat{R}_{12} = \frac{1}{\sqrt{N}} \sum_{j=1}^{N} \hat{R}^j_{12} e^{-i(\boldsymbol{k}_1 - \boldsymbol{k}_{\mathrm{c}1}) \boldsymbol{r}_j}, \qquad \hat{R}_{nn} = \frac{1}{N} \sum_{j=1}^{N} \hat{R}^j_{nn}. \tag{2.83}$$

Moreover, we assume the phase-matching approximation

$$e^{i(\boldsymbol{k}_2 - \boldsymbol{k}_{\mathrm{c}2}) \boldsymbol{r}_j}, \;\; e^{i(\boldsymbol{k}_2 - \boldsymbol{k}_{\mathrm{c}1}) \boldsymbol{r}_j}, \;\; e^{i(\boldsymbol{k}_{\mathrm{c}1} - \boldsymbol{k}_1) \boldsymbol{r}_j}, \;\; e^{i(\boldsymbol{k}_2 - \boldsymbol{k}_{\mathrm{c}1}) \boldsymbol{r}_j} \approx 1. \tag{2.84}$$

All these assumptions ensure that atoms interact collectively (or coherently) with optical fields. Under these conditions FWM will generate the maximum number of photons in two quantum modes, while the inhomogeneities and non-ideal phase matching decreases the generation rate. Thus with these assumptions being made we are considering the upper bound of generated photons for a system with a given cooperativity. Even in this situation we prove to have a steady-state population unperturbed by the generated fields after the transient time. The transient time is the time needed for the system to converge to a steady-state population.

We arrive at the system of equations that takes similar form as equations (2.77)–(2.81), only written for collective operators, and is given in Appendix C.2. All these equations are parameterized by number of atoms N, although we use cooperativity as the parameter, which is directly proportional to N ($C_i = \frac{Ng_i^2}{\kappa\gamma_{i3}}$).

$\boldsymbol{\kappa}$	$\boldsymbol{\gamma}_{13}, \boldsymbol{\gamma}_{23}$	$\boldsymbol{\gamma}_{12}$	$\boldsymbol{g}_1, \boldsymbol{g}_2$	$\boldsymbol{\Omega}_1$	$\boldsymbol{\Omega}_2$	$\boldsymbol{\Delta}_1$	$\boldsymbol{\Delta}_2$
30	6	0.1	10^{-3}	3.53	10	90	30

Table (2.1) Parameters used for numerical simulation of the transient populations regime. All values are in MHz/(2π), cooperativity is $C = 10$.

Numerical simulations are depicted in Figure 2.7. They demonstrate that in the range of low to moderate cooperativities the discrepancy between the exact solution and the stationary approximation is negligible and our approximation is valid. Besides proving our hypothesis the numerical solution provides us with an estimate of the transient time, which depends on the pump power and the detuning roughly as an optical pumping time $\sim \left(\frac{\Omega_1^2}{\Delta_2} + \frac{\Omega_2^2}{\Delta_1}\right)^{-1}$.

Taking into account the results of collective operator simulations we may proceed further with the model for single atom equations (2.77)–(2.81) and stationary population to get the analytical treatment of the emitted light and take into account inhomogenities of the ensemble.

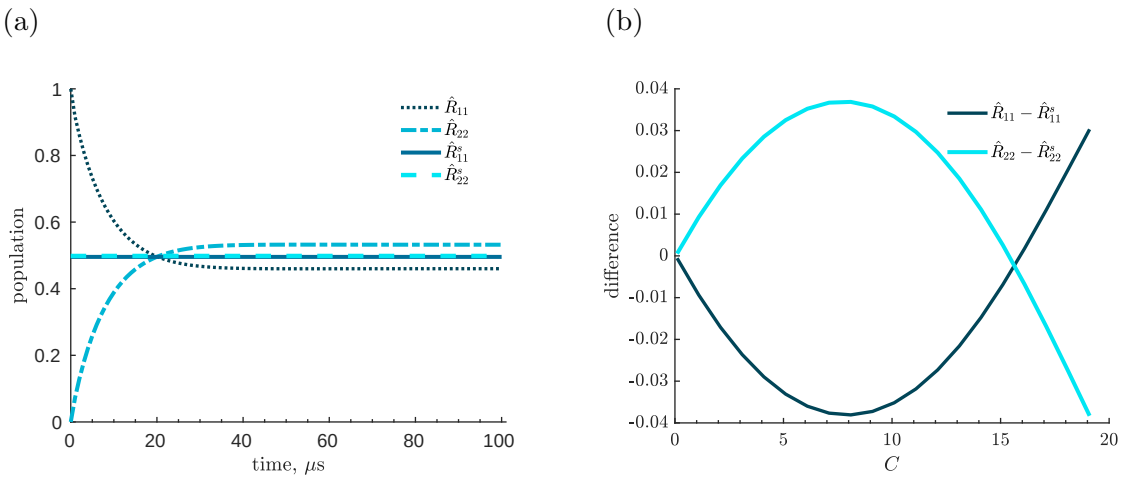

Figure (2.7) (a) Dynamics of the atomic populations $R_{11}(t)$, $R_{22}(t)$ for numerical solution of equations (C.8–C.15) and the respective steady-state solutions R^{s}_{11}, R^{s}_{22} used in further analysis. The parameters are summarized in Table 2.1. (b) Difference between numerical and analytic solutions as a function of cooperativity parameter taken at the time after evolution stops (time $> 50\mu$s). Assuming the same cooperativity $C = 10$ for both cavity modes.

2.4.4 Intracavity field spectrum

For further analysis we apply the Fourier transform $\hat{a}_1(t) = \int \tilde{a}_1(\omega)e^{-i\omega t}d\omega$, $\hat{a}_2^\dagger(t) = \int \tilde{a}_2^\dagger(-\omega)e^{-i\omega t}d\omega$ [5]. Remarkably, the assumption of a constant population leads to a delta function in the frequency domain. However, if the pump's intensity is not high $\Omega_{1,2}^2/\Delta_{2,1} \ll \gamma_{13}+\gamma_{23}$ the population exhibits fluctuation with a characteristic time of $(\gamma_{13}+\gamma_{23})^{-1}$. Thus instead of a delta function a Lorentzian spectrum can be used $I(\omega) = \frac{\Gamma}{\omega^2+\Gamma^2}$.

We assume homogeneity of our atomic cloud and pumps, so both coupling constants and pumping strengths are uniform over an atomic cloud: $g_{1,2}^j = |\, g_{1,2}\,| e^{i\boldsymbol{k}_{1,2}\boldsymbol{r}_j}$ and $\Omega_{1,2}(z_j) = |\,\Omega_{1,2}\,| e^{i\boldsymbol{k}_{\mathrm{c1,c2}}\boldsymbol{r}_j}$. We have explicitly included wavevectors of the pumping fields $\boldsymbol{k}_{\mathrm{c1,c2}}$ and the cavity modes $\boldsymbol{k}_{1,2}$ to monitor an effect of the phase-matching conditions on the generation process. Equations (2.79)–(2.81) are resolved to find coherences, which are substituted into equations (2.77)–(2.78). The final system of equations for two intracavity fields in the Fourier

[5] Tilde symbolizes the dependence on ω. Throughout the section we use the short substitution: $\tilde{a}_1(\omega) \to \tilde{a}_1$, $\tilde{a}_2(-\omega) \to \tilde{a}_2$, etc.

domain is

$$-\left(i(\delta_1-\omega)+\kappa/2+\frac{\kappa C_1\langle P_{13}\rangle}{\tilde{\Delta}(\omega)/\gamma_{13}}\right)\tilde{a}_1+\tilde{\chi}(\omega)\,\phi\,\langle P_{23}\rangle\tilde{a}_2^\dagger+\tilde{L}_1+\sqrt{\kappa}\tilde{a}_{\mathrm{in},1}=0, \tag{2.85}$$

$$\left(i(\delta_2+\omega)-\kappa/2-\frac{\kappa C_2\langle P_{23}\rangle}{\tilde{\delta_2}(\omega)/\gamma_{23}}\tilde{c}(\omega)\right)\tilde{a}_2^\dagger+\tilde{\chi}(\omega)\,\phi^*\langle P_{13}\rangle\tilde{a}_1+\tilde{L}_2+\sqrt{\kappa}\tilde{a}_{\mathrm{in},2}^\dagger=0, \tag{2.86}$$

where the parameters are

$$C_1=\sum_j\frac{|g_1|^2}{\kappa\gamma_{13}},\quad C_2=\sum_j\frac{|g_2|^2}{\kappa\gamma_{23}},\quad \tilde{c}(\omega)=1-\frac{|\Omega_2|^2}{\tilde{\delta}_1(\omega)\tilde{\delta}_2(\omega)}+\frac{|\Omega_1|^2|\Omega_2|^2}{\tilde{\Delta}(\omega)\tilde{\delta}_1^2(\omega)\tilde{\delta}_2(\omega)}, \tag{2.87}$$

$$\tilde{\Delta}(\omega)=i(\Delta_1-\omega)+\gamma_{13}/2+\frac{\Omega_1^2}{i(\delta-\omega)+\gamma_{12}/2+\frac{\Omega_2^2}{-i(\Delta_2+\omega)+\gamma_{23}/2}}, \tag{2.88}$$

$$\tilde{\delta}_1(\omega)=i(\delta-\omega)+\gamma_{12}/2+\frac{\Omega_2^2}{\gamma_{23}/2-i(\Delta_2+\omega)},\quad \tilde{\delta}_2(\omega)=\gamma_{23}/2-i(\Delta_2+\omega), \tag{2.89}$$

$$\tilde{\delta}_3(\omega)=\gamma_{12}/2+i(\delta-\omega)+\frac{\Omega_1^2}{\gamma_{13}/2+i(\Delta_1-\omega)}. \tag{2.90}$$

C_1 and C_2 are collective atomic cooperativities on transitions $|1\rangle\rightarrow|3\rangle$ and $|2\rangle\rightarrow|3\rangle$, respectively. Detunings (2.88)–(2.90) represent the sum of experimental detunings and AC-Stark shifts induced by applied pump fields, which scale as $\propto\Omega^2/\Delta$. Together with these parameters we introduced functions $\tilde{L}_{1,2}=\tilde{F}_{1,2}+\delta\tilde{F}_{1,2}$, which characterize uncorrelated

spontaneous scattering, and $\tilde{\chi}$ is an effective nonlinearity akin to one from Section 2.2.

$$\tilde{\chi}(\omega) = \frac{|\,g_1\,||\,g_2\,||\,\Omega_1\,||\,\Omega_2\,|}{\tilde{\delta}_1(\omega)\tilde{\delta}_2(\omega)\tilde{\Delta}(\omega)}, \quad \phi = \sum_j e^{i(\boldsymbol{k}_{c1}+\boldsymbol{k}_{c2}-\boldsymbol{k}_1-\boldsymbol{k}_2)\boldsymbol{r_j}}, \tag{2.91}$$

$$\tilde{F}_1 = \frac{|\,g_1\,||\,\Omega_2\,|}{\tilde{\Delta}(\omega)}\left(-\langle\, P_{13}\,\rangle + \frac{|\,\Omega_1\,|^2\,\langle\, P_{23}\,\rangle}{\tilde{\delta}_1(\omega)\tilde{\delta}_2(\omega)}\right)\sum_j e^{i(\boldsymbol{k}_{c2}-\boldsymbol{k}_1)\boldsymbol{r}_j} I(\omega), \tag{2.92}$$

$$\tilde{F}_2 = -\frac{|\,g_2\,||\,\Omega_1\,|}{\tilde{\delta}_2(\omega)}\left(\tilde{c}(\omega)\langle\, P_{23}\,\rangle - \frac{|\,\Omega_2\,|^2\,\langle\, P_{13}\,\rangle}{\tilde{\Delta}(\omega)\tilde{\delta}_1(\omega)}\right)\sum_j e^{i(\boldsymbol{k}_{2}-\boldsymbol{k}_{c1})\boldsymbol{r}_j} I(\omega), \tag{2.93}$$

$$\delta\tilde{F}_1 = \sum_j \frac{|g_1|e^{-i\boldsymbol{k}_1\boldsymbol{r}_j}\left(\tilde{\delta}_1(\omega)\hat{F}^j_{13}(\omega) + \frac{|\Omega_1\Omega_2|}{\tilde{\delta}_2(\omega)}e^{i(\boldsymbol{k}_{c1}+\boldsymbol{k}_{c2})\boldsymbol{r}_j}\hat{F}^j_{32}(\omega) - i|\Omega_1|e^{i\boldsymbol{k}_{c1}\boldsymbol{r}_j}\hat{F}^j_{12}(\omega)\right)}{(\gamma_{13}/2 + i\,(\Delta_1-\omega))\left(\tilde{\delta}_1(\omega) + \frac{|\Omega_1|^2}{\gamma_{13}/2+i(\Delta_1-\omega)}\right)}, \tag{2.94}$$

$$\delta\tilde{F}_2 = \sum_j \frac{|g_2|e^{i\boldsymbol{k}_2\boldsymbol{r}_j}\left(i|\Omega_2|e^{-i\boldsymbol{k}_{c2}\boldsymbol{r}_j}\hat{F}^j_{12}(\omega) + \tilde{\delta}_3(\omega)\hat{F}^j_{32}(\omega) + e^{-i(\boldsymbol{k}_{c1}+\boldsymbol{k}_{c2})\boldsymbol{r}_j}\frac{|\Omega_1\Omega_2|}{\gamma_{13}/2+i(\Delta_1-\omega)}\hat{F}^j_{13}(\omega)\right)}{\tilde{\delta}_2(\omega)\left(\tilde{\delta}_1(\omega) + \frac{|\Omega_1|^2}{(\gamma_{13}/2+i(\Delta_1-\omega))}\right)} \tag{2.95}$$

The nonlinearity coefficient $\tilde{\chi}$ describes a four-photon process [72], where absorption of one photon from each pump is accompanied by emission of idler and signal photons. The FWM is a phase-sensitive process that is reflected in the multiplier ϕ, which contains information on phase matching. The sum over all atoms leads to a sharp sinc function with a maximum set by the phase-matching condition $(\boldsymbol{k}_{c1} + \boldsymbol{k}_{c2} - \boldsymbol{k}_1 - \boldsymbol{k}_2)\boldsymbol{r}_j = 0$. We explicitly demonstrate this in Subsection 5.1.2 together with estimates for three different pump configurations. Here we are limiting our discussion to the preferable direction of photon emission. If both pumps have the same wavevector direction, then the directions for signal and idler photons are identical too. When the pumps are counter-propagating, the counter-propagating signal and idler photons are emitted with collective enhancement. If we assume that phase matching is held and coupling constants are only different by a coefficient $\alpha = |\,g_2\,|\,/\,|\,g_1\,|$, the effective nonlinearity can be expressed in more experimentally accessible parameters:

$$\tilde{\chi} \approx \frac{\kappa\gamma_{13}\alpha C_1\,|\,\Omega_1\,||\,\Omega_2\,|}{\tilde{\delta}_1(\omega)\tilde{\delta}_2(\omega)\tilde{\Delta}(\omega)} \tag{2.96}$$

From equations (2.92)–(2.93) we conclude that terms $\tilde{F}_{1,2}$ represent the Rayleigh scattering, i.e. reemission of pump photons into the cavity mode. In other words, after the pump with frequency ω_{c1} (ω_{c2}) is absorbed by an atom, it emits a photon with the same frequency ω_{c1} (ω_{c2}). On the other hand, since the pump is detuned from the cavity resonance by an amount of $\Delta_1 - \Delta_2$, the Rayleigh emission is suppressed. One more condition for collective enhancement of this process is phase matching: the pumps and generated photons should propagate in the same direction $\boldsymbol{k}_{c1} = \boldsymbol{k}_2$ and $\boldsymbol{k}_{c2} = \boldsymbol{k}_1$.

2.4.5 Optimization of generated fields

The solution of the linear system of equations (2.85)–(2.86) is

$$\tilde{a}_1 = \frac{\tilde{\chi}\,\langle P_{23}\rangle\left(\sqrt{\kappa}\tilde{a}^{\dagger}_{\mathrm{in},2} + \tilde{L}_2\right) + \left(\sqrt{\kappa}a_{\mathrm{in},1} + \tilde{L}_1\right)\left(\frac{\kappa C_2}{\tilde{\delta}_2/\gamma_{23}}\tilde{c}\langle P_{23}\rangle + \frac{\kappa}{2} - i(\delta_2+\omega)\right)}{\left(\frac{\kappa C_1\langle P_{13}\rangle}{\tilde{\Delta}/\gamma_{13}} + \frac{\kappa}{2} + i(\delta_1-\omega)\right)\left(\frac{\kappa C_2}{\tilde{\delta}_2/\gamma_{23}}\tilde{c}\langle P_{23}\rangle + \frac{\kappa}{2} - i(\delta_2+\omega)\right) - \langle P_{23}\rangle\langle P_{13}\rangle\tilde{\chi}^2} \tag{2.97}$$

$$\tilde{a}^{\dagger}_2 = \frac{\tilde{\chi}\,\langle P_{13}\rangle\left(\sqrt{\kappa}\tilde{a}_{\mathrm{in},1} + \tilde{L}_1\right) + \left(\sqrt{\kappa}a^{\dagger}_{\mathrm{in},2} + \tilde{L}_2\right)\left(\frac{\kappa C_1\langle P_{13}\rangle}{\tilde{\Delta}/\gamma_{13}} + \frac{\kappa}{2} + i(\delta_1-\omega)\right)}{\left(\frac{\kappa C_1\langle P_{13}\rangle}{\tilde{\Delta}/\gamma_{13}} + \frac{\kappa}{2} + i(\delta_1-\omega)\right)\left(\frac{\kappa C_2}{\tilde{\delta}_2/\gamma_{23}}\tilde{c}\langle P_{23}\rangle + \frac{\kappa}{2} - i(\delta_2+\omega)\right) - \langle P_{23}\rangle\langle P_{13}\rangle\tilde{\chi}^2} \tag{2.98}$$

This system of equations takes the same form as the derived system of equations for the OPO (2.34)–(2.35), although in this case the dynamics of the system includes the response of the atomic system. The analogy with the OPO is very close, except that now the parametric gain $\chi(\omega)$ has limited bandwidth and is different for two fields by a population difference. Furthermore, each cavity mode exhibits an additional refractive index change and absorption due to the atoms. The refractive index manifests itself as a shift of the resonant frequency by $\sim \frac{\kappa C_1 \Delta_1 \langle P_{13}\rangle}{(\Delta_1^2+\gamma_{13}^2/4)/\gamma_{13}}$, while absorption introduces additional losses $\sim \frac{\kappa C_1 \gamma_{13}\langle P_{13}\rangle}{(\Delta_1^2+\gamma_{13}^2/4)/\gamma_{13}}$ and hence broadens the cavity linewidth.

As was discussed in Section 2.2, to obtain maximum squeezing the intracavity losses should be minimized. Together with that the OPO should operate close to the threshold with symmetric gain for both modes. Thus in theory we optimize the squeezing by finding the global maximum in the range of accessible parameters. However in the experiment some

parameters are not easy to control (e.g., cooperativity) and some are fixed (e.g., cavity linewidth), the only parameters we can manipulate are the power of the pumps and their detunings. Taking into account these principles, we can roughly formulate a strategy for getting maximal squeezing for the atomic OPO. For the given cooperativities C_1 and C_2 and the cavity linewidth κ, the following conditions should be fulfilled:

1. Minimizing losses for both modes $\frac{\kappa C_1 \langle P_{13} \rangle}{\tilde{\Delta}(\omega)/\gamma_{13}}$ and $\frac{\kappa C_2 \langle P_{23} \rangle}{\tilde{\delta}_2(\omega)/\gamma_{23}} \tilde{c}(\omega)$
2. Minimizing disbalance in gain by minimizing $|\langle P_{23} \rangle - \langle P_{13} \rangle|$
3. Maximizing the OPO gain $\langle P_{23} \rangle \langle P_{13} \rangle \tilde{\chi}^2$

2.4.6 Observables

We once again resort to the input-output formalism ($a_{\text{out}} = \sqrt{\kappa} a - a_{\text{in}}$) to find the field outside of the cavity. To simplify representation we introduce new notations:

$$\tilde{C}_1 = \left(\frac{\kappa C_1 \langle P_{13}^j \rangle}{\tilde{\Delta}/\gamma_{13}} + \frac{\kappa}{2} + i\delta_1 \right) \quad \text{and} \quad \tilde{C}_2 = \left(\frac{\kappa C_2}{\tilde{\delta}_2/\gamma_{23}} \tilde{c} \langle P_{23}^j \rangle + \frac{\kappa}{2} - i\delta_2 \right), \tag{2.99}$$

thus:

$$\tilde{a}_{\text{out},1} = \sqrt{\kappa} \frac{\tilde{\chi} \cdot \langle P_{23} \rangle \left(\sqrt{\kappa} \tilde{a}_{\text{in},2}^\dagger + \tilde{L}_2 \right) + \left(\sqrt{\kappa} \tilde{a}_{\text{in},1} + \tilde{L}_1 \right) \tilde{C}_2}{\tilde{C}_1 \tilde{C}_2 - \langle P_{23} \rangle \langle P_{13} \rangle \tilde{\chi}^2} - \tilde{a}_{\text{in},1} \tag{2.100}$$

$$\tilde{a}_{\text{out},2}^\dagger = \sqrt{\kappa} \frac{\tilde{\chi} \cdot \langle P_{13} \rangle \left(\sqrt{\kappa} \tilde{a}_{\text{in},1} + \tilde{L}_1 \right) + \left(\sqrt{\kappa} \tilde{a}_{\text{in},2}^\dagger + \tilde{L}_2 \right) \tilde{C}_1}{\tilde{C}_1 \tilde{C}_2 - \langle P_{23} \rangle \langle P_{13} \rangle \tilde{\chi}^2} - \tilde{a}_{\text{in},2}^\dagger \tag{2.101}$$

Knowing this, we can construct expressions for observables and second-order correlators of interest. The spectrum of the number of generated Stokes and anti-Stokes photons in each

channel is given by

$$\langle \hat{n}_{\text{out},1}(\omega) \rangle = \kappa \frac{|\tilde{\chi}|^2 \langle P_{23} \rangle^2 \kappa + \left| \tilde{\chi} \langle P_{23} \rangle \tilde{F}_2 + \tilde{F}_1 \tilde{C}_2(\omega) \right|^2}{\left| \tilde{C}_1(\omega)\tilde{C}_2(\omega) - \langle P_{23} \rangle \langle P_{13} \rangle \tilde{\chi}^2 \right|^2}, \tag{2.102}$$

$$\langle \hat{n}_{\text{out},2}(\omega) \rangle = \kappa \frac{|\tilde{\chi}|^2 \langle P_{13} \rangle^2 \kappa + \left| \tilde{\chi} \langle P_{13} \rangle \tilde{F}_1 + \tilde{F}_2 \tilde{C}_1(\omega) \right|^2}{\left| \tilde{C}_1(\omega)\tilde{C}_2(\omega) - \langle P_{23} \rangle \langle P_{13} \rangle \tilde{\chi}^2 \right|^2}. \tag{2.103}$$

We can see that contribution into the intensity can be decomposed into the "useful" coherent $\propto |\tilde{\chi}|^2 \langle P_{i3} \rangle^2$ and incoherent parts with $\tilde{F}_{1,2}$. Moreover the incoherent part is decomposed into the spontaneous emission from the "real" level $|3\rangle$ and incoherent Raman scattering. The former effect arises as a contribution from the Langevin noise operator and its emission goes into the same mode as the signals from four-wave mixing. The details of the noise contribution are presented in Appendix A.1.

We demonstrate the behaviour of the spectrum of generated photons in two channels in Figure 2.8. For small pump powers Ω_1 most of the population stays on level $|2\rangle$ and the generated signal in the second channel is smaller than in the first (Fig. 2.8(a)). With an increase of pump power the population on two levels evens, and the generation is close in both modes (Fig. 2.8(b)). Even higher pumping power unbalances signals, so the signal mode in the second exceeds the signal in the first (Fig. 2.8(c)–(d)).

$\boldsymbol{\kappa}$	$\boldsymbol{\gamma}_{13}, \boldsymbol{\gamma}_{23}$	$\boldsymbol{\gamma}_{12}$	$\boldsymbol{\Omega}_2$	$\boldsymbol{\Delta}_1$	$\boldsymbol{\Delta}_2$
30	6	0.1	6	80	20

Table (2.2) Parameters used for calculations if not stated otherwise; all values are in MHz/(2π), cooperativity is $C = 15$.

2.4.7 Threshold condition

It is well known [61], that OPO has a feature of coherent generation once the gain exceeds the losses within the cavity (Fig. 2.9). This point is usually called the threshold

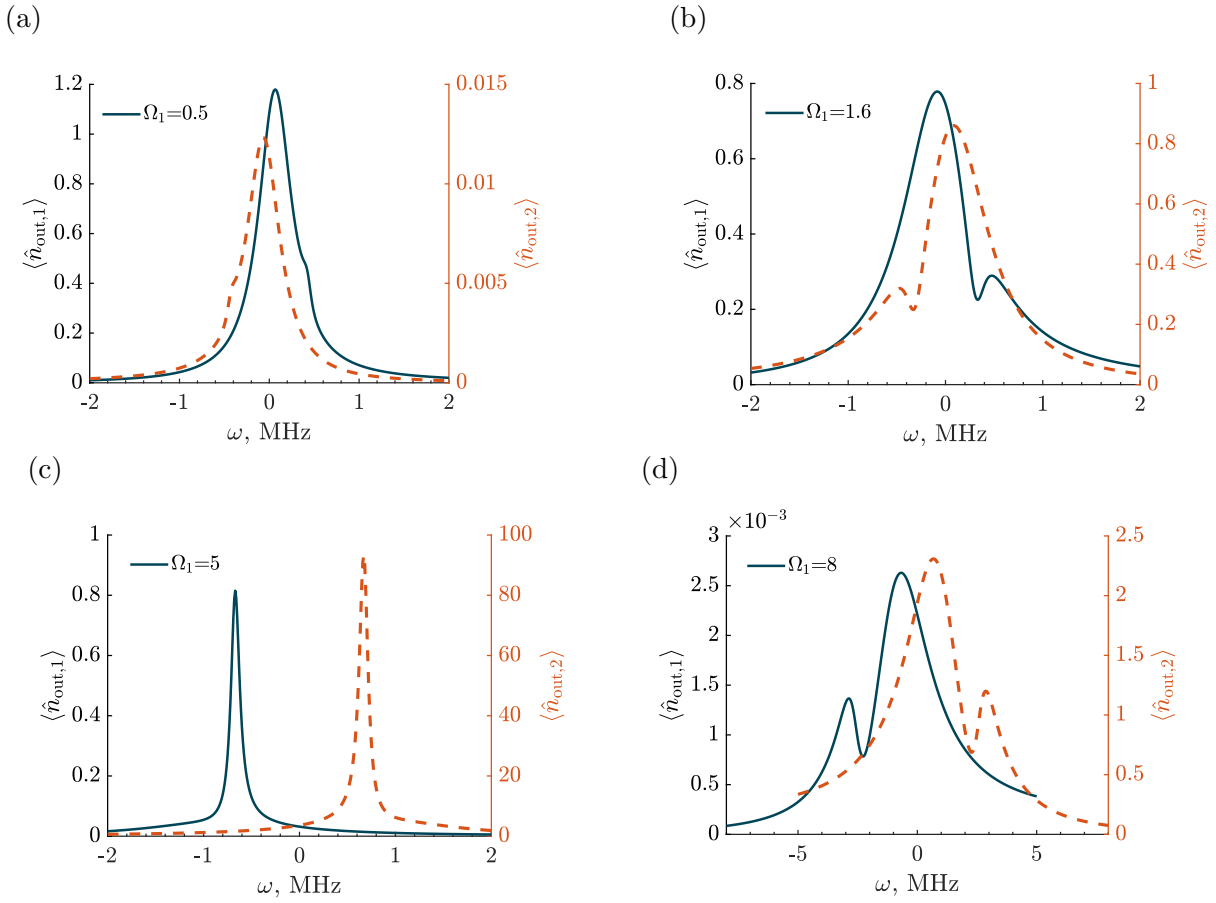

Figure (2.8) Spectrum of number of photons generated in each quantum mode via formulas (2.102)–(2.103). The left axis (dark blue solid) represents number of photons in the first mode, the right axis (red dashed)–in the second. The parameters used in the calculations are given in Table 2.2. Power of the first pump is varied for (a)–(d) and written in the left upper corner.

or coherent generation. At the threshold and above, the generated Stokes and anti-Stokes photons stimulate subsequent emission into the same modes, this amplifies and narrows the output radiation.

In Figure 2.9(b) we plot the difference between the gain and losses to reveal regions of the above threshold generation. The region shifts to higher frequencies due to AC-Stark shift and it broadens with an increasing power. In Figure 2.9(b) we can see narrowing of the spectrum with an increasing number of photons, as it was demonstrated earlier for the OPO model.

Despite the fact that our model is valid for description below the threshold, we can still find this point. According to (2.100)–(2.101) at the threshold the common denominator of equations equals zero, which corresponds to phase transition towards coherent generation:

$$\left(\frac{\kappa C_1 \langle\, P_{13}\,\rangle}{\tilde{\Delta}/\gamma_{13}} + \frac{\kappa}{2} + i(\delta_1 - \omega)\right)\left(\frac{\kappa C_2}{\tilde{\delta}_2/\gamma_{23}}\tilde{c}\langle\, P_{23}\,\rangle + \frac{\kappa}{2} - i(\delta_2 + \omega)\right) - \langle\, P_{23}\,\rangle\langle\, P_{13}\,\rangle\tilde{\chi}^2 = 0, \tag{2.104}$$

In general, the equation (2.104) can be solved numerically as the function of experimental parameters to check the existence of the threshold at the given frequency component. However condition of double Raman resonance fixes cavity frequency detunings $\omega = \delta_1$, $\delta_1 = -\delta_2 = \delta$, and one pumps's detuning $\Delta_1 = \Delta_2 + \delta$. From symmetrical consideration we may notice, that better squeezing occurs for equal gain for both modes, this dictates the equal population on level $|\,1\,\rangle$ and $|\,2\,\rangle$ ($P_{13} = P_{23} = 1/2$). Further assumption such as slow coherence decay $\gamma_{12} \approx 0$ and relatively large single photon detuning $\Delta_2 > \gamma_{13}, \gamma_{23}$ helps to derive simpler expression for threshold conditions:

$$\left(\frac{C_1}{\tilde{\Delta}/\gamma_{13}} + 1\right)\left(\frac{\kappa C_2}{\tilde{\delta}_2/\gamma_{23}}\tilde{c} + 1\right) - \left(\frac{\tilde{\chi}}{\kappa}\right)^2 = 0, \tag{2.105}$$

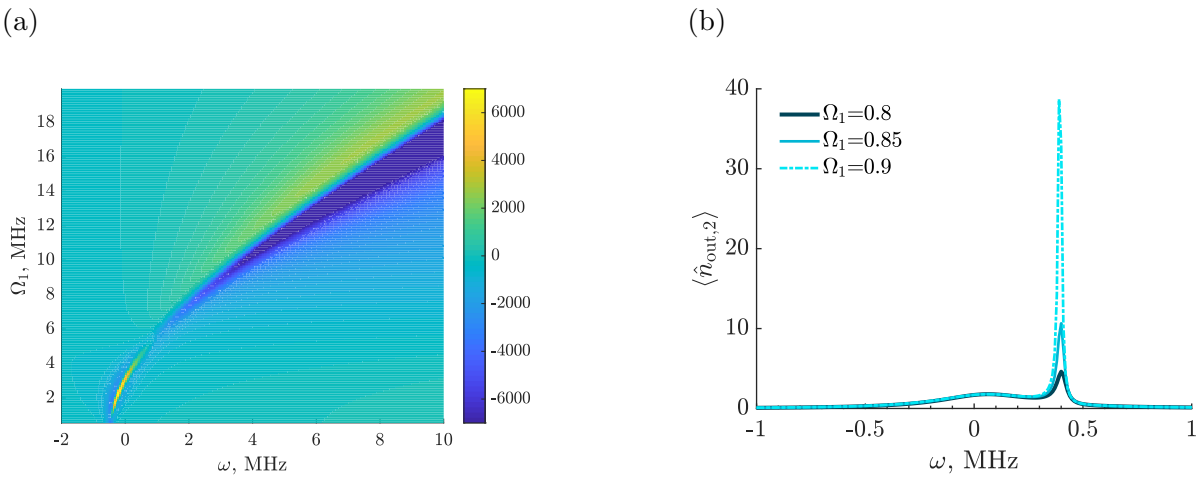

Figure (2.9) (a) Spectrum of difference between gain and loss as a dependence on power of the first power. If the quantity coded by the color is more than zero then gain exceeds losses and vice versa. (b) Spectrum of photons generated in one mode depending on the power of the first pump as the system approaches the threshold. For both calculations we use parameters from Table 2.2 and $C = 15$ and $\Omega_2 = 6$.

taking into account the simplification of the detuning we arrive at the expression:

$$\left(\frac{\Omega_1^2}{\Omega_2^2 \Delta_2} - \frac{1}{\Delta_2 + \omega} \right) = \frac{\Delta_2}{C_1 C_2 \gamma_{13} \gamma_{23}}. \tag{2.106}$$

Remarkably the expression is similar to that for the N-level atomic optical parametric oscillator [73], where cooperativity is replaced by an ensemble's optical depth.

2.5 Conclusion

We develop the model for describing four-wave mixing in the Λ atomic system, where both optical fields and atoms are treated quantum-mechanically. This model is similar to the optical parametric oscillator having both narrow band gain and arbitrary portion of losses and gain in each channel. Our model enables us to find the properties of the emitted Stokes and anti-Stokes photons, such as intensity and second-order correlators, and find the appropriate values of the control parameters.

The simulation predicts that four-wave mixing exhibits three regimes. In the first regime,

when the far detuned pump's intensity is large, the strong Stokes generation is accompanied by an order of magnitude weaker anti-Stokes emission. For the second, when the opposite pump is stronger, the picture reverses, i.e., anti-Stokes emission could be a few orders of magnitude more powerful than the Stokes. Moreover, in both cases the spectrum of emitted photons becomes narrower than the Raman emission linewidth. The third regime is found for the narrow range of pump powers and detunings, when the generated number of photons for two modes is balanced, and the conditions are preferable for squeezing. This regime corresponds to the symmetrical OPO and utilized in experiment. This agrees with the intuitive idea, that the gain for both modes of optical parametric oscillator operating below the threshold should be balanced.

Chapter 3

Darkness of two-mode squeezed light in the Λ-type atomic system

The concept of dark state is used intensively for describing a plethora of phenomena, to name a few: sub-recoil optical cooling [74], coherent population trapping, electromagnetically induced transparency [53], and slow and stopped light [75]. The mentioned phenomena usually take place in an atomic system with Λ transitions between the ground $|\,1\,\rangle$, metastable $|\,2\,\rangle$ and the excited $|\,3\,\rangle$ levels. The dark state is a special superposition of two ground levels [53]. Due to destructive quantum interference, the total dipole moment of the interaction with two phase-locked light fields on the optical transitions vanishes. Dark states, discovered initially in atomic physics, have recently been observed in circuit quantum electrodynamics [76, 77] and semiconductors [78, 79].

In the present work we demonstrate the existence of a set of optical dark (OD) states that are distinct from the states described above, as they are fully separable from the atomic state. These states require all atoms to be in the ground level, in contrast to a preparation of atomic superposition for a coherent population trapping. We explicitly show that while propagating through the resonant absorbing medium OD states do not evolve. Rather surprising, these belong to a family of nonclassical, entangled states or more specifically to

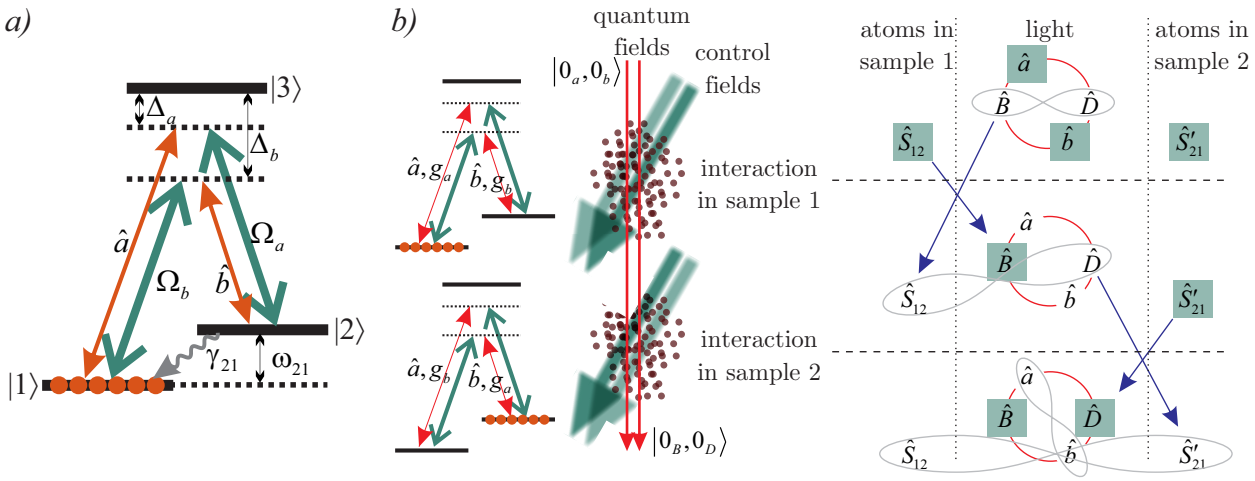

Figure (3.1) a) The atomic level scheme. The two quantum modes $\hat{a}$ and $\hat{b}$, in which the OD state is present, are in two-photon resonance with the strong classical fields Ω_a and Ω_b, respectively. b) Generating the two-mode squeezed OD state $|\,0_B, 0_D\,\rangle$ from vacuum input $|\,0_a, 0_b\,\rangle$ in two atomic samples. Left: scheme of the experiment and energy level diagrams. The coupling constants and the populations of the two samples are exchanged with respect to the two ground states. Right: Exchange of entanglement among the optical modes and atomic coherences. Red circles symbolize the Bogoliubov transformation that relate the pairs of optical modes $(\hat{a}, \hat{b})$ and $(\hat{B}, \hat{D})$. Shading marks the modes that are in the vacuum state, infinity symbols denote the TMSV state. Top: at the entrance of the first sample, the atomic ensembles and the physical modes $\hat{a}$ and $\hat{b}$ are in their ground states, which means that the Bogoliubov modes $\hat{B}$ and $\hat{D}$ are TMSV entangled as per Eq. 3.8. Center: the interaction in the first sample swaps the optical Bogoliubov mode $\hat{B}$ and the atomic coherence $\hat{S}_{12}$. Bottom: in the second sample, the contents of $\hat{D}$ and $\hat{S}'_{12}$ are swapped. Now the atomic samples are TMSV entangled while the Bogoliubov modes are in the vacuum state, which means that the physical light modes are in the TMSV state as well according to Eq. 3.6.

the two-mode squeezed states, whose quantum properties are vulnerable to attenuation [60]. While propagating through an attenuator (a lossy channel), the quantum features of an optical state are shared with the environment and lost when the environment is traced over. Here we demonstrate that TMSV can not only propagate through an attenuating medium without being affected by losses, but in fact is created thanks to these losses.

3.1 System

Similar to the atomic dark state, the OD state arises in Λ-shaped atomic systems. Two hyperfine levels $|\,1\,\rangle$ and $|\,2\,\rangle$ are coupled in pairs with coherent pumps and quantum modes

(Fig. 3.1(a)), where two pumping fields, having Rabi-frequencies Ω_a and Ω_b, are in two-photon resonance with the corresponding quantum fields, called signal and idler. Annihilation (creation) operator $\hat{a}_k$ ($\hat{a}_k^\dagger$) of optical field is introduced inside the 'large enough' optical resonator that its modes are closely spaced and become quasi-continuous [80]. As the result the discrete commutation relationship can be replaced with continuous: $[\hat{a}_k, \hat{a}_{k'}^\dagger] = \delta_{k'}^k \to \delta(k-k')$ [1].

In contrast with the previous chapter, where the quantum fields were localized inside an optical cavity, here we consider a one-dimensional system, where the fields propagate along the z direction and an atomic ensemble has a cigar-shape with length L along this z axis. To take into account the propagating nature of the fields it is convenient to introduce the continuous spatial Fourier transform of annihilation (creation) operators $\hat{a}(z) = (2\pi)^{-1/2} \int \hat{a}_k e^{ikz}\, dk$. Thus for a given problem we consider two quantum fields, which are defined by annihilation operators $\hat{a}(z)$ and $\hat{b}(z)$ and obey commutation relations $[\hat{a}(z), \hat{a}^\dagger(z')] = [\hat{b}(z), \hat{b}^\dagger(z')] = \delta(z-z')$.

The ensemble is comprised of N atoms and initially is polarized to one of the lowest levels $|\,1\,\rangle$. The atomic system is described by collective continuous atomic operators $\hat{S}_{nm}(z) = \frac{L}{N}\sum_{j=1}^{N} \hat{S}_{nm}^j \delta(z-z_j)$, where the single atom operator $\hat{S}_{nm}^j$ transfers the jth atom from level $|\,m\,\rangle$ to $|\,n\,\rangle$. The commutation relations for the collective operators are $\left[\hat{S}_{nm}(z'), \hat{S}_{mn}(z'')\right] = \frac{L}{N}\delta(z'-z'')\left(\hat{S}_{nn}(z') - \hat{S}_{mm}(z')\right)$.

The interaction Hamiltonian driving the system from the above in the RWA is [81, 70]:

$$\begin{aligned}\hat{H} =& \hbar n_0 \int_0^L \Big\{ \left(g_{31}\hat{a}(t,z)e^{-i\omega_a t} + \Omega_b e^{-i\omega_{\Omega_b} t}\right)\hat{S}_{31}(t,z) \\ &+ \left(g_{32}\hat{b}(t,z)e^{-i\omega_b t} + \Omega_a e^{-i\omega_{\Omega_a} t}\right)\hat{S}_{32}(t,z) + \text{ h.c.}\Big\}\, dz, \end{aligned} \tag{3.1}$$

where $n_0 = N/L$ is a linear atomic density, g_{31} and g_{32} are photon-atom coupling constants for the corresponding optical transitions [82], $\omega_{a,b}$ and $\omega_{\Omega_{a,b}}$ are the carrier frequencies of the

[1] where $\delta_{k'}^k$ is the Kronecker delta and $\delta(k-k')$ is Dirac delta-function

quantum and control fields, respectively.

We are assuming that the signal and control fields are far detuned from the excited state $|\,3\,\rangle$ (i.e., $\Delta_{a,b} \gg \gamma_{13}, \gamma_{23}, \Omega_{a,b}$), where γ_{13} and γ_{23} are the spontaneous decay rates from the excited level $|\,3\,\rangle$. This allows us to adiabatically eliminate level $|\,3\,\rangle$. Moreover, if $\Delta_{a,b} > \omega_{21}$, then two quantum fields experience an almost identical dispersion. This ensures the phase-matching condition, so that the both modes $\hat{a}$ and $\hat{b}$ experience the same dispersion throughout the sample. With these approximations being made we arrive at the following effective interaction Hamiltonian:

$$\hat{V}_{\text{eff}} = \hbar n_0 \int_0^L \left(g_a^* \hat{a}^\dagger + g_b \hat{b} \right) \hat{S}_{12}\, dz + \text{h.c.}, \tag{3.2}$$

where $g_a = \frac{g_{31}\Omega_a^*}{\Delta_a}$ and $g_b = \frac{g_{32}\Omega_b^*}{\Delta_b}$ are the effective coupling constants of the signal and idler modes with the spin wave. Without loss of generality we choose the coupling constants in a way that $|g_b| < |g_a|$, hereafter we set the phase convention for $\hat{a}$ and $\hat{b}$ to be chosen such that g_a and g_b are real and positive.

Equation (3.2) is valid if the respective control and quantum field pairs are in a two-photon resonance with the ground states that are ac Stark shifted by the control fields, which we assume to be the case. Another important assumption is that the majority of the atomic population is in state $|\,1\,\rangle$, which is valid on time scales that are small compared to the inverse optical pumping rate associated with the control field Ω_b: $\frac{|\,\Omega_b\,|^2 \gamma_3}{\Delta_b^2} t \ll 1$. In this case, $n_0[\hat{S}_{12}(z'), \hat{S}_{21}(z'')] \approx \delta(z' - z'')$ the Hilbert space associated with the collective atomic excitation becomes isomorphic to that of the harmonic oscillator under the Holstein-Primakoff transformation [82, 83].

3.2 Optical dark state

To reveal an appearance of the OD state, we perform a Bogoliubov transformation of the signal and idler modes into new modes $\hat{B}$ and $\hat{D}$:

$$\hat{B} = \alpha_0^{-1}(\hat{a} + \epsilon\hat{b}^\dagger) \quad \text{and} \quad \hat{D} = \alpha_0^{-1}(\hat{b} + \epsilon\hat{a}^\dagger), \tag{3.3}$$

where $\alpha_0 = \sqrt{1 - |\,\epsilon\,|^2}$ and $\epsilon = g_b/g_a$. Under this transformation the Hamiltonian (3.2) takes form:

$$\hat{V}_{\text{eff}}(t) = \hbar\alpha_0 g_a n_0 \int_0^L \left(\hat{B}^\dagger \hat{S}_{12} + \hat{B}\hat{S}_{12}^\dagger\right) dz. \tag{3.4}$$

We notice that the atomic system is coupled only to the "bright" mode $\hat{B}$, while the Hamiltonian commutes with mode $\hat{D}$ ($[\hat{D}, \hat{V}_{\text{eff}}] = 0$). Obviously, the field in the "dark" mode $\hat{D}$ is decoupled from the interaction and subsequently from evolution. We can easily find the full class of eigenvectors of this Hamiltonian with the zero eigenvalue:

$$\hat{V}_{\text{eff}}(t)\,|\,0_B, \Phi_D\,\rangle \otimes |\,\mathbb{G}\,\rangle_{\text{at}} = 0, \tag{3.5}$$

where $|\,\Phi_D\,\rangle$ is an arbitrary state of dark mode $\hat{D}$ and $|\,\mathbb{G}\,\rangle_{\text{at}} = |\,1_1...1_j...1_N\,\rangle$ is a collective atomic ground state. Thus atoms prepared in the ground state will not interact with an optical state $|\,0_B, \Phi_D\,\rangle$, where the dark mode is not necessarily in the vacuum state. We call this state an optical dark state.

Here I would like us to stop and spotlight the difference between the proposed Hamiltonian and the commonly used FWM Hamiltonian for generation of TMSV [15, 27]. The effective parametric Hamiltonian (Section 2.2) excludes the media from the evolution, limiting its effect to the nonlinear susceptibility. It results in an exponential growth of squeezing as the field is propagating through the sample (albeit with vulnerability to losses). In the current chapter keeping the dynamics of atomic state and polarizing the atomic population

to one ground level we arrive to the beam-splitter type Hamiltonian (3.4). In Holstein-Primakoff approximation the beam-splitter form of coupling defined by the Hamiltonian (3.4) in an optically deep medium leads to the swapping of the states between the optical mode $\hat{B}$ and the atomic coherence $\hat{S}_{12}$. The decay of atomic coherence will dissipate the energy from the system bringing the optical state into darkness [84].

3.3 Darkness of two-mode squeezed state

Of particular interest among the OD states is the vacuum state $|\, 0_B, 0_D \,\rangle$ of modes $\hat{B}$ and $\hat{D}$. Because the original modes ($\hat{a}$, $\hat{b}$) are related to ($\hat{B}$, $\hat{D}$) via the Bogoliubov transformation, the state $|\, 0_B, 0_D \,\rangle$ in the eigenbasis of ($\hat{a}$, $\hat{b}$) is a TMSV. Analogously to definitions given in Section 2.1, we can write the vacuum state:

$$|\, 0_B, 0_D \,\rangle = \exp\left[-r(\hat{a}^\dagger \hat{b}^\dagger - \hat{a}\hat{b})\right] |\, 0_a, 0_b \,\rangle = \alpha_0 \sum_n (-\epsilon)^n \,|\, n_a, n_b \,\rangle\,, \tag{3.6}$$

where $r = \frac{1}{2}\log\frac{1-\epsilon}{1+\epsilon}$ is the squeezing parameter and $|\, n_{a,b} \,\rangle$ denotes number states. This state is characterized by the mean photon numbers $\langle\, \hat{n}_a \,\rangle = \langle\, \hat{n}_b \,\rangle = \epsilon^2/\alpha_0^2$ and the position/momentum quadrature correlation

$$\langle\, (X_a \pm X_b)^2 \,\rangle = \langle\, (P_a \mp P_b)^2 \,\rangle = e^{\pm 2r} = \frac{1 \pm \epsilon}{1 \mp \epsilon}, \tag{3.7}$$

with $\epsilon = r = 0$ corresponding to the standard quantum limit [85]. The squeezing becomes infinite in theory for $\epsilon \to 1$.

State (3.6) coincides with the vacuum state $|\, 0_a, 0_b \,\rangle$ if $\epsilon = 0$. This case corresponds to the idler control field being absent, so in accordance with interaction (3.4) the signal field can experience Raman absorption, decaying into the vacuum state while propagating through the sample. On the other hand, for $\epsilon \neq 0$, the physical vacuum is not an OD state. To see this, we notice that this state is two-mode squeezed in the basis of the Bogoliubov bright

and dark modes:

$$|\, 0_a, 0_b \,\rangle = \exp\left[r(-\hat{B}\hat{D} + \hat{B}^\dagger \hat{D}^\dagger)\right] |\, 0_B, 0_D \,\rangle\,. \tag{3.8}$$

If this state is injected into our atomic sample, the bright mode will be absorbed by the atoms, decaying into $|\, 0_B \,\rangle$. With the atomic coherence dissipating into the environment, mode $\hat{D}$ becomes thermal, with the quadrature variance $\langle\, X_D^2 \,\rangle = \langle\, P_D^2 \,\rangle = \frac{1}{2}\cosh 2r = \frac{1+\epsilon^2}{1-\epsilon^2}$:

$$\hat{\rho}_{B,D} = |\, \alpha_0 \,|^2\, |\, 0_B \,\rangle\langle\, 0_B \,| \otimes \sum_n \epsilon^{2n}\, |\, n_D \,\rangle\langle\, n_D \,|\,. \tag{3.9}$$

State (3.9), albeit unpure, is two-mode squeezed in the basis of modes $\hat{a}$ and $\hat{b}$ by no more than a factor of 2 with respect to the standard quantum limit:

$$\begin{aligned} \langle\, (X_a \pm X_b)^2 \,\rangle &= \langle\, (P_a \mp P_b)^2 \,\rangle \\ &= \frac{1}{2} e^{\mp 2r}(1 + \cosh 2r) = (1 \pm \epsilon)^{-2}. \end{aligned} \tag{3.10}$$

This squeezing can be experimentally observed by performing a homodyne measurement on the signal and idler modes upon exiting the sample.

The fact that an entangled state remains unchanged while propagating through an absorbing medium, while the vacuum state loses its purity and becomes entangled, is highly counterintuitive. We explain this by observing that the interaction of the light with the environment occurs via the bright mode $\hat{B}$. The pair of modes $(\hat{B}, \hat{D})$ therefore defines the decoherence-preferred basis. States that are entangled in this basis do decohere. However, because this basis is itself entangled in terms of the physical modes $(\hat{a}, \hat{b})$, this decoherence presents itself as growth of entanglement of the latter modes.

3.4 Optical dark states in the presence of dissipation

To explicitly show that OD state is preserved in an ensemble with incoherent decay, we study the evolution of the modes by taking into account the effective Hamiltonian (3.4) with the free Hamiltonians of atoms, dark and bright fields, we have the following Heisenberg-Langevin equations:

$$(\partial_t + c\partial_z)\,\hat{B} = -i\alpha_0 n_0 g_a \hat{S}_{12}, \quad (\partial_t + c\partial_z)\,\hat{D} = 0, \tag{3.11}$$

$$\frac{d\hat{S}_{12}}{dt} = -\frac{\gamma_{12}}{2}\hat{S}_{12} - i\alpha_0 g_a \hat{B} + i\sqrt{\gamma_{12}}\hat{F}_{12}(t,z) + \delta(t-t_0)\hat{S}_{12}(t_0,z), \tag{3.12}$$

where γ_{12} is the ground state coherence decay constant, $\langle\, \hat{F}_{12}\,\rangle$ are the Langevin forces with the correlation functions $\langle\, \hat{F}^{\dagger}_{12}(t,z)\,\rangle = \langle\, \hat{F}_{12}(t',z')\,\rangle = 0$, $n_0\langle\, \hat{F}_{12}(t,z)\hat{F}^{\dagger}_{12}(t,z')\,\rangle = c\cdot\delta(z-z')$. A general solution to Eq. (3.12) can be found similarly to Ref. [86]. Using the Fourier transformation $\hat{B}(\omega,Z) = \frac{1}{\sqrt{2\pi}}\int \hat{B}(\tau,Z)e^{i\omega\tau}d\tau$ in the co-moving reference frame $\tau = t - z/c$, $Z = z$ and parameterizing the optical depth via $\kappa = \alpha_0^2 n_0 \mid g_{\rm s} \mid^2/(c\gamma_{12})$, we arrive at:

$$\begin{aligned}
&\hat{B}(\omega,Z) = e^{-\frac{2\kappa\cdot Z}{(1-2i\omega/\gamma_{12})}}\hat{B}(\omega,0) + \\
&+ 2\int_0^Z \frac{\sqrt{n_0\kappa/(c\gamma_{12})}}{(1-2i\omega/\gamma_{12})} e^{\frac{2\kappa(Z'-Z)}{(1-2i\omega/\gamma_{12})}}\left(\sqrt{\gamma_{12}}\hat{F}_{12}(\omega,Z') + \frac{ie^{i\omega(t_0-Z'/c)}}{\sqrt{2\pi}}\hat{S}_{12}(t_0,Z')\right)dZ',
\end{aligned} \tag{3.13}$$

$$\hat{D}(\omega,Z) = \hat{D}(\omega,0). \tag{3.14}$$

Mode $\hat{B}$ exhibits usual Beer's absorption and tends to the vacuum state $\mid 0_B\,\rangle$ in the limit of infinite optical depth, while mode $\hat{D}$ stays unchanged. As an example of such an evolution we input in our media physically vacuum state $\mid 0_a, 0_b\,\rangle$:

$$\langle\, \hat{n}_B\,\rangle = \frac{\mid \epsilon \mid^2}{1-\mid \epsilon \mid^2} e^{-\frac{2\kappa\cdot Z}{1+(2\omega/\gamma_{12})^2}} \quad \text{and} \quad \langle\, \hat{n}_D\,\rangle = \frac{\mid \epsilon \mid^2}{1-\mid \epsilon \mid^2}. \tag{3.15}$$

Solution (3.13) allows us to monitor nonclassical correlations in the position and momentum quadratures of mode $\hat{B}$ and $\hat{D}$ as they propagate through the sample (Fig. 3.2 (a)). Once

again for the initial state being in a physical vacuum, we have variances of quadratures:

$$\langle\, \Delta \hat{X}_B^2(\omega, Z)\,\rangle = \langle\, \Delta \hat{P}_B^2(\omega, Z)\,\rangle = \left(\frac{1}{2} + \frac{\epsilon^2}{1-\epsilon^2} e^{-\frac{4\kappa Z}{1+(2\omega/\gamma_{12})^2}}\right). \tag{3.16}$$

We see that the quadrature variance of the bright field evolves to the value of $\frac{1}{2}$, which is characteristic of the vacuum state. If the storage protocol is not used, the atomic states are traced out and we obtain the thermal state in the OD-mode:

$$\hat{\rho}_{B,D} = |\,\alpha_0\,|^2\,|\,0_B\,\rangle\langle\,0_B\,| \otimes \sum_n |\,\epsilon\,|^{2n}\,|\,n_D\,\rangle\langle\,n_D\,|\,. \tag{3.17}$$

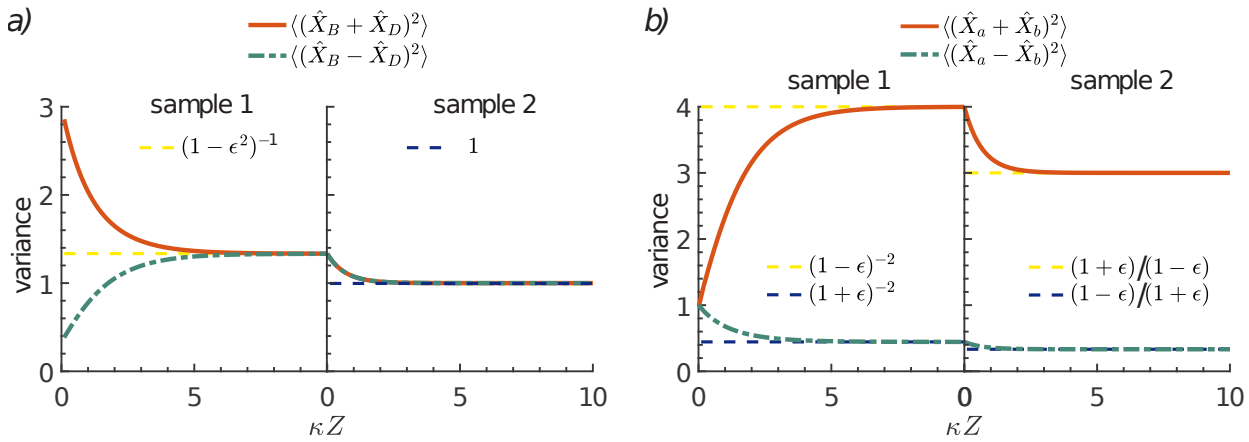

Figure (3.2) (a) Development of entanglement of the optical modes as they propagate through the two samples for the vacuum input $|\,0_a, 0_b\,\rangle$ and $\epsilon = 0.5$. a) Bogoliubov $(\hat{B}, \hat{D})$ modes; b) Physical modes $(\hat{a}, \hat{b})$. The variances of the individual position quadratures as well as their sum and difference are displayed. At the entrance of the first sample, the Bogoliubov modes are in the TMSV state. Between the samples, the state is mixed and described by Eqs. (3.9) and (3.10). After the second sample, the Bogoliubov modes are in the vacuum state, and the physical modes are in TMSV described by Eqs. (3.6) and (3.7)

3.5 Preparation of two-mode squeezed state via dissipation

We now show how our scheme can be extended to prepare the two mode squeezed vacuum state (3.6) from physical vacuum input. To that end, we send the optical modes through an additional, similar atomic sample (Fig. 3.1(b)) with the atomic population prepared in state $|\,2\,\rangle$. In addition, we invert the ratio ϵ, which is equivalent to exchanging the values of the coupling constants g_a and g_b on the atomic transitions. This is done by adjusting the amplitudes and phases of the Rabi frequencies Ω_a and Ω_b. In this case the effective Hamiltonian is

$$\hat{V'}_{\rm eff} = \hbar\alpha_0 g_a n_0 \int_0^L \left(\hat{D}^\dagger \hat{S}'_{21} + \hat{D}(\hat{S}'_{21})^\dagger\right) dz, \tag{3.18}$$

where the primes mark the second sample. Now mode $\hat{D}$ becomes bright and experiences absorption, while mode $\hat{B}$ is dark and does not evolve. Since, after the first sample, mode $\hat{B}$ is already in the vacuum state, propagation through the second sample will yield the double-vacuum state (3.6) of modes $\hat{B}$ and $\hat{D}$.

In Figure 3.2 we demonstrate evolution of quadratures passing through two inversely polarized ensembles in both bases. If we start with the TMSV state in the ($\hat{B}$, $\hat{D}$) basis after the first sample the mode $\hat{B}$ is absorbed and in mode $\hat{D}$ we have thermal state (3.17). After the second sample the mode $\hat{D}$ is absorbed and we have vacuum in both modes $|\,0_B, 0_D\,\rangle$. At the same time in a physical basis ($\hat{a}$, $\hat{b}$) the evolution starts with vacuum $|\,0_a, 0_b\,\rangle$, after the first ensemble two modes are in a partially mixed state. The second ensemble finishes preparation of TMSV state through a dissipative (absorptive) process (Fig. 3.2(a)).

In addition to robustness to losses, our technique permits easy control of the squeezing parameter $r(\epsilon)$ by adjusting the strengths of the control fields. Potential detrimental factors such as nonlinearities caused by a finite population in level $|\,2\,\rangle$ can be suppressed by reducing

the interaction time and working at sufficiently large one-photon detunings.

3.6 Dynamical preparation of optical dark state

It is interesting to analyze the emergence of OD states in the context of gradient echo memory setting [87, 88], in which the frequency of the ground state transition varies along the sample. Figure 3.3 shows the the number of photons in the signal mode as it propagates through the sample. When the fields enter the atomic sample, the two-photon detuning for each pair of control and quantum fields is significant, so a four-wave mixing process develops, leading to amplification. At the center of the sample, with the onset of two-photon resonance, the bright mode is absorbed; its optical state becomes vacuum $|\,0_B\,\rangle$.

Curiously, with further propagation, this state remains unchanged in spite of the reemergence of the two-photon detuning. This can be intuitively explained as follows. In the presence of two-photon detuning $\delta_{12}(Z)$, the Hamiltonian (3.4) acquires an additional position-dependent term $\int \delta_{12}(Z)\hat{S}_{22}(Z)dZ$ [89]. When this detuning is significant, it dominates the light-atom interaction and results in the evolution of the dark field according to the phase shift $B(\omega, Z) = e^{-i\phi(Z,\omega)}B(\omega, 0)$ with $\phi(Z,\omega) \propto \frac{\kappa dZ}{\delta_{12}(Z)-\omega}$. In the Schrödinger picture, this

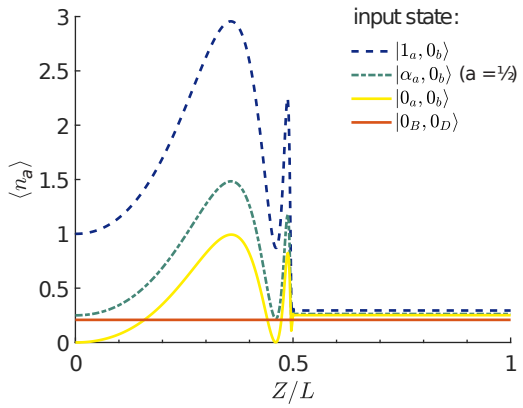

Figure (3.3) Photon number of the signal mode propagating through an atomic sample with a longitudinal inhomogeneous broadening of the ground state transition according to $\omega_{21}(z) = \omega_{21}(0) + \beta(Z - L/2)$, where β is gradient constant. The optical depth normalized by the inhomogeneous broadening is $\kappa\gamma_{12}/\beta = 5$.

phase shift corresponds to the evolution operator $\hat{U} = e^{-i\int d\omega\, \phi(Z,\omega)\hat{B}^\dagger(\omega,0)\hat{B}(\omega,0)}$. If the bright mode is in the vacuum state, this operator equals identity, so no evolution is present.

3.7 Conclusion and discussion

The OD state formalism proposed here introduces a unified theoretical framework for a whole range of recent theoretical and experimental studies of different quantum systems of various nature. In addition to the aforementioned application to light-atom interfacing [90, 91, 29], this mechanism can be used to interpret the emergence of entangled states of the collective spin and the mecahnical motion of an atomic cloud interacting with a dissipative common cavity mode [92, 93, 94]. Similar physics occurs in optomechanics, where two cavity modes are weakly coupled with a single mechanical oscillator [95, 96]. By proper choice of the detunings of the driving optical fields (e.g., one field being blue-detuned with respect to the first cavity mode the other is red with respect to the second), one can obtain an interaction of the form (3.2), which can again be treated by introducing the dark and bright modes of the cavities.

In this work, we concentrated on the regime of $\epsilon < 1$, which describes a beamsplitter-like interaction (3.4). The special case $\epsilon = 1$ results in the so-called quantum mechanics free subsystem [97], providing a way to evade quantum-measurement backaction [98]. For the case of $g_b > g_a$, a transformation analogous to Eq. (3.3) can be applied, resulting in the interaction of the parametric form $\hat{V}_{\text{eff}} \sim \hat{D}\hat{S}_{12} + \hat{D}^\dagger\hat{S}_{12}^\dagger$. The associated physics will be studied elsewhere.

In conclusion, we have shown the existence of optical dark two-color field states in Λ atomic ensemble accompanied by FWM. These dark states—the special two-mode squeezed states—do not evolve while propagating through an ensemble. They can be expressed in terms of dark and bright mode as a product of bright mode in vacuum and arbitrary state of the dark mode. Based on this, we propose the generation method for the dark states via

either dissipative or purely dynamic interactions. We note that the OD state picture and the generation method gives us a bridge to the physics of the recently proposed schemes of macroscopic entanglement generation with atomic [91] and optomechanical [95] systems.

The paper relevant to this chapter is accepted for publication in New Journal of Physics. The current version is uploaded to arXiv, see [84].

Chapter 4

Experimental tools and techniques

In this chapter we describe the experimental tools and techniques used in our experiment. Two essential ingredients required for the two-mode squeezed state generation are a nonlinear medium and pumping fields. We have chosen to induce the FWM process in Rubidium atoms. These atoms are cooled via optical molasses to achieve a dense yet cold species. Low temperature reduces Doppler broadening below the natural linewidth, and their level structure becomes effectively three-level or lambda-type (see Fig. 4.1(a)). Two lower hyperfine levels are coupled to an excited state with two lasers inducing emission of two squeezed modes. The atomic cloud is overlapped with a cavity mode to enhance light-atom interaction. Since the cavity determines the spatial mode, it also requires to be stabilized to keep it in resonance with both emitted photonic modes.

In this chapter we will describe all required apparatuses for the experiment. We start with a description of our vacuum system in Section 4.1, which is necessary to reduce collisions with background gases and to cool gas to low temperatures. In the next Section 4.2 we talk about the lasers used at all stages of the experiment. We set constraints on their frequency stability and discuss the locking techniques used. With the laser system defined, we move on to the atomic cooling methods and characterization of the cloud (Section 4.3). Section 4.4 is dedicated to the cavity's assembly, its characteristics and stabilization. The last missing tool

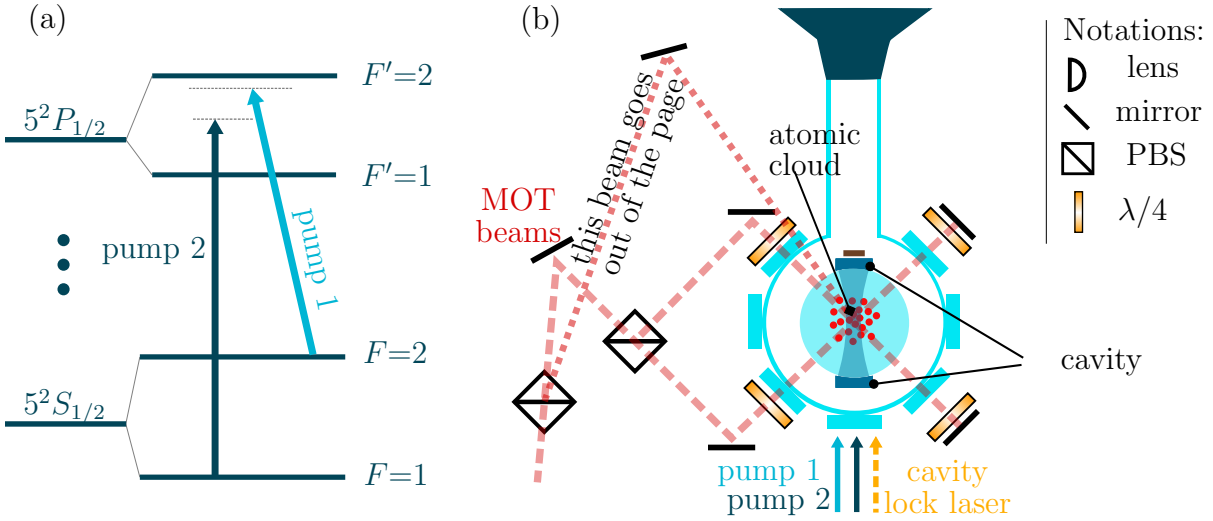

Figure (4.1) (a) D_1 line of Rubidium 87. Two pumps are closely tuned to the upper $F' = 2$ transition. (b) The simplified experimental setup with only essential parts included: optical molasses (red dashed lines), two pumps for 4WM (two solid blue lines) and the cavity lock laser (dashed orange). Both pumps and cavity lock laser enter from the same input cavity port. An atomic cloud is prepared with optical molasses, which includes two more lasers. It is overlapped with the mode of the resonator to have an effective coupling.

is a measurement of non-classical light. We utilize a homodyne detection, which acquires a quadrature of the electromagnetic field. In the last section we consolidate all parts and divide an experiment into time stages.

4.1 Vacuum system

A home-made glass chamber is the central part of the vacuum chamber. The idea of using the commercially produced chambers was rejected in order to avoid Eddy currents. The chamber was blown in the science workshop and has height of 5.5 cm and diameter of 7 cm. Another student then glued to it seven windows in a horizontal plane (⌀ 2.5 cm) and two larger viewports (⌀ 5 cm) on the top and bottom. In total the center of the chamber is optically accessible from five different directions. Three of them are used for an optical molasses, one is an optical cavity output, and the last one could be used for the initial optical pumping or for pumping at ninety degrees. To reach a high vacuum (HV) we use three pumping stages. The pumping process starts with a rotational mechanical pump (*SH-*

(a)

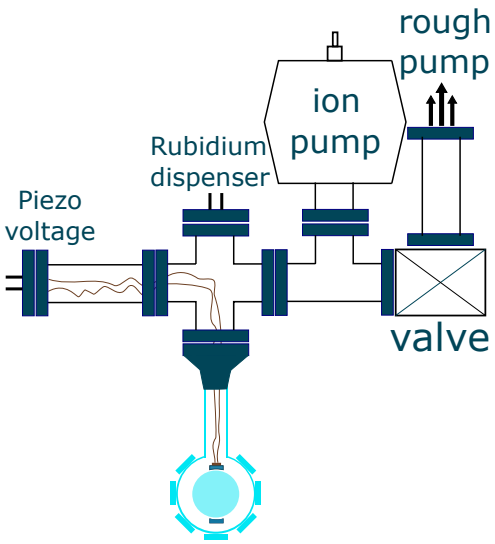

(b)

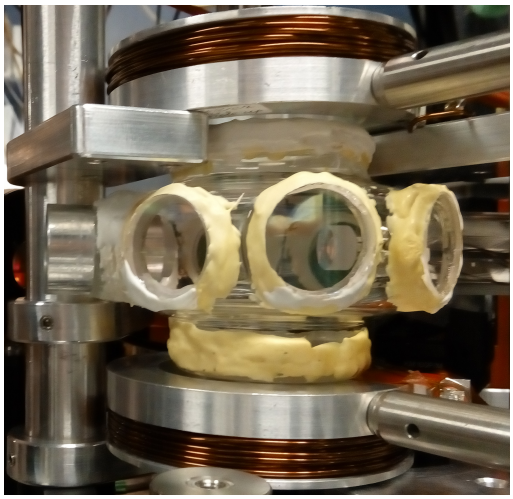

Figure (4.2) (a) Vacuum system consists of a rough pump, which works on an initial stage of a process. After it follows a valve isolating main vacuum chamber, where an ion pump maintains HV pressure. A Rubidium atom dispenser directly faces the glass vacuum chamber, where a magneto-optical trap works. One extra feedthrough on the left is used to control cavity length with a piezo-actuator. The glass vacuum chamber (light blue color) has 7 view ports in a horizontal plane. Two larger windows from top an bottom fulfill a requirement of three orthogonal directions for an optical molasses. (b) Photo of a glass vacuum chamber, two-mirrors forming the resonator are visible. Two coils from the top and bottom are placed close to the vacuum chamber and form a magnetic quadrupole trap.

110 Dry scroll, Agilent), which reaches a pressure of 10^{-2} Torr. Secondly, a turbo pump (*V-81M, Agilent*) reduces pressure to 10^{-6} Torr. At this stage, a bake-out is performed to speed up water desorption, material outgassing, and diffusion rates. Our home-made glass vacuum chamber is glued with a vacuum epoxy (*Torr Seal*). This significantly limits the upper temperature that we can reach without causing damage. The melting point from the datasheet is 120°C, although in the experiment we uncovered that we should not exceed 100°C.

After we cool down our system, we start an ion pump (*varian, VacIon* 8 l/s) and shut off a valve thereby isolating the vacuum chamber from the rough pumps. The ion pump runs continuously in order to compensate for an overall leakage of the vacuum chamber and to pump out excessive Rubidium atoms used in experiments. Due to heating and cooling processes and due to age, the glass part of the vacuum chamber does not allow us to enter the ultra-high vacuum (UHV) regime. For this reason leaving us with pressure $1 \cdot 10^{-8}$ Torr on the border between UHV and HV.

As a source of natural Rubidium we use alkali metal dispensers from SAES (*RB/NF/4.8/17 FT10+10*). We asked the University of Calgary science workshop to weld three of them in row to a gasket with a feedthrough. We run a controllable current of 2.5–3 A, which heats the dispensers to a certain temperature when a reduction reaction between a chromate and the St 101 alloy starts and frees pure Rubidium. In our system we encountered that the amount of alkali atoms lasts only two to three years, after which we were forced to repeat a pumping procedure. A good solution is to use a flange with a few sets of feedthroughs each with its own set of dispensers, which would allow us work continuously without opening the vacuum.

4.2 Lasers and locks

In our experiment we work with Rubidium 87. There are two transitions from its ground state $5^2S_{1/2}$ to its nearest excited levels $5^2P_{1/2}$ and $5^2P_{3/2}$ lying in a near infrared, usually called D1 and D2 lines respectively [67]. There are many coherent sources existing for the required wavelength: cheap GaAs diodes, tunable Ti-Sapphire lasers, fiber lasers with frequency doubling, dye lasers and others. To optically cool atoms we use two lasers (Section 4.3) and to achieve primary atom-light interaction we require two more. An additional laser is used to preset and keep constant the central frequency of the cavity. Three of these lasers are home-made external-cavity diode lasers in the so-called Littrow configuration [99, 100]. Two other lasers were available when I arrived, one of them is a commercial Toptica *DL-100* and the other is an *MBR-110* Titanium-Sapphire laser.

Each laser is playing a different role and has different constraints on the maximum allowable frequency shift, although the upper limit for all of them is 5 MHz. The range is estimated from two main scales in our experiment: the natural linewidth of Rubidium (6 MHz) and the cavity linewidth (30 MHz). In reality wavelengths of ECDL lasers drift by at least 10 MHz per minute. Thus, we have to have good frequency references. There are three typical optical frequency standards: high-Q reference cavities, certain electronic transition of atoms, or actively stabilized frequency combs. We combine both the cavity and atomic approaches in our work. It seems natural to use a saturated absorption spectroscopy of Rubidium 87 and it indeed works for two cooling lasers (Subsections 4.2.1, 4.2.2). However, the cavity lock laser must be far-detuned from an atomic resonance for two reasons. First, it follows the same path as the signal and pump do (Fig. 4.1), and it would inevitably have reached detectors and interfered with the measurement. Secondly, being close to resonance it would have induced unwanted atomic transitions, introducing noise photons. Therefore, we detune the laser away from the atomic transition and lock its frequency to the master laser (Subsection 4.2.3).

To control a laser frequency and lock it to the references mentioned above, we have to

familiarize ourselves with the way it operates. The central core of a home-made ECDL laser is a semiconductor laser diode, whose faces are polished and act as a small Fabry-Perot cavity. Its gain bandwidth is as wide as 5–10 nm, and the emission will happen on one of many longitudinal modes having maximum gain. If we adjust the temperature of the diode we change the effective length of the cavity, thus changing the resonant longitudinal mode. This method is versatile to have access to a wide range of wavelengths, typically we observe around $\Delta\nu$ =1 GHz change per $\Delta T = 0.1°$. Of course, this tremendous sensitivity sets a high demand on the temperature controller. While the temperature stability of the controller of 0.001° is easily obtainable, the temperature setting accuracy is less precise, e.g., only 0.1° for *ITC102, Thorlabs*. Moreover, the setting process is very slow, with the proportional–integral–derivative controller's oscillation period being a few seconds. For these reasons the temperature is not used to compensate fast frequency fluctuations. The second and the fastest adjustment of emitted frequency is a change of the injection current, which affects both the temperature of the diode and the refractive index [101]. It enables a high-frequency modulation (up to 1 GHz) at a cost of a small mode-hop free range (200 MHz).

A laser diode chip is already a fully functional laser, however, its frequency tunability and stability is not enough for probing cold alkali atoms. To narrow the emission line an external resonator is used. If the resonator's linewidth is narrower than that of the laser, it will bind the laser emission to its own frequency. The design of the external cavity we use has an additional holographic diffraction grating, which is set on an angle to send the first order of diffraction back into the diode. The diode laser and the grating form an external cavity approximately 4 cm long. A piezo-actuator is mounted behind the grating and an applied voltage slightly tilts it, causing lasing frequency changes. Summarizing all of the above, there are three ways to set the required wavelength of ECDL: temperature, injection current, and piezo-actuator (or grating angle).

Additionally to this short term change (due to temperature fluctuations, current ripples and vibrations), ECDL is strongly affected by the ambient temperature. Unfortunately,

there is no thermostat in the room, and the temperature could change by two to five degrees per day. This leads to a necessity of a rough adjustment of the laser's wavelength every few hours and makes an experiment extremely tedious.

In the preceding discussion we focused our attention on the drift of the mean value of the central frequency, although coherent processes in atoms additionally demand the narrow linewidth of the pumping lasers and local oscillators. Furthermore, both pumps are supposed to be phase-locked to each other with minimal relative phase noise (Subsection 5.1.4). The linewidth of the MBR laser is <75 kHz. The Toptica claims to have 100 kHz to 1 MHz at 5 μs integration time, when we measure it on longer integration times and it becomes comparable with our home-made lasers with $\Delta\nu = 5$ MHz. We use phase-locking techniques described in Subsections 4.2.3 and 4.2.4 to narrow the linewidth of the second pump (Toptica).

4.2.1 Lock-in and Saturated absorption

Laser's frequency should be stabilized within a MHz from the desired value for laser cooling. The natural way of stabilization is to use an atomic absorption line as the reference. Unfortunately, the Doppler broadening of an atomic line at a room temperature makes an optical transition a few orders of magnitude larger than its natural linewidth (500 MHz versus $\gamma = 6$ MHz), that is unacceptable for stabilization. Thankfully, there is a simple and elegant way to overcome this obstacle, which is called the saturated absorption [102]. By applying counter-propagating strong pump and weak probe beams one can see the reduction of the probe's absorption due to saturation by the pump, if only the pump and the probe are interacting with the same atoms. The former is valid for atoms with zero velocity, and it can be easily explained if we consider an atom with velocity v (projection of on the propagation axis) and transition frequency ν_0 in 1D. In the laboratory reference frame both probe and pump have frequency ν_0 and opposite $\pm\boldsymbol{k}$ wavevectors, which leads to an opposite Doppler shift in the atomic reference frame and frequencies $\nu_0 \pm \nu_0 v/c$. Evidently both fields interact simultaneously only with atoms with zero velocity, making it possible to resolve the natural

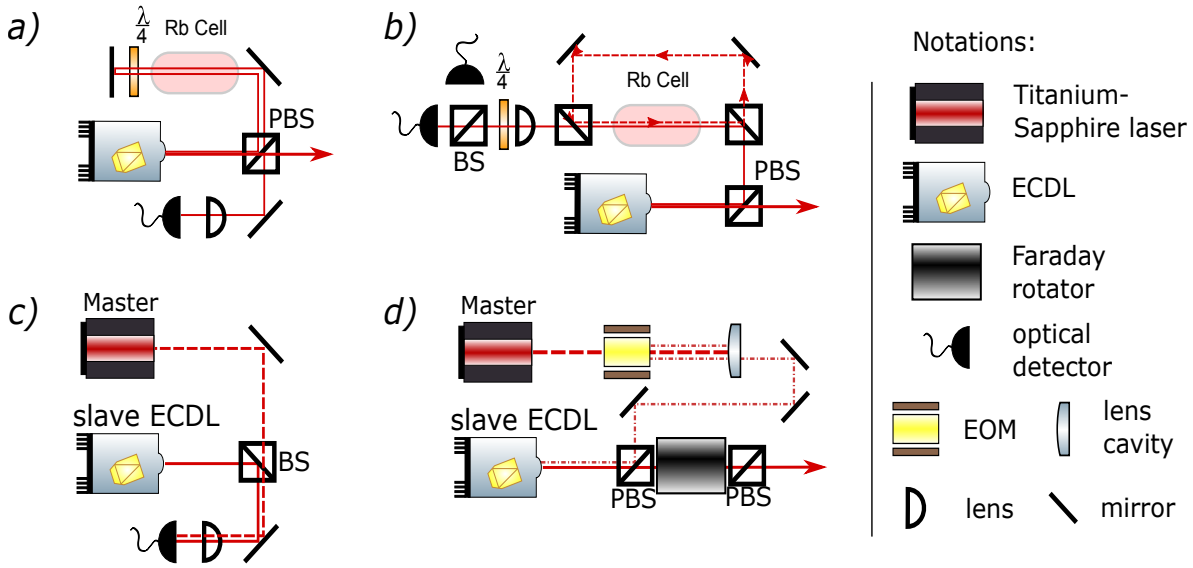

Figure (4.3) Optical diagrams of laser locks we use. a) A double-pass spectroscopy is sent to a photodetector to generate an error signal, which is sent into a lock-in amplifier. b) DAVLL lock. The beam is split in to two parts, a weak linearly polarized probe experiences a circular dichroism in an atomic cell. Right and left circularily polarized portions of the beam go to two separate detectors. More powerful part of the beam counter-propagates through the cell to induce a saturated absorption. c) OPLL. Two lasers to be locked are mixed on a BS, for a maximal beating signal the mode-matching should be well optimized. The ultra-fast detector's converts high frequency beating signal in an oscillating current, which is fed to a PLL. d) Injection lock uses a modulated beam of a master laser. This beam bypasses a Faraday isolator, and enters an internal resonator of a slave ECDL by reflecting from the first PBS.

(a) (b)

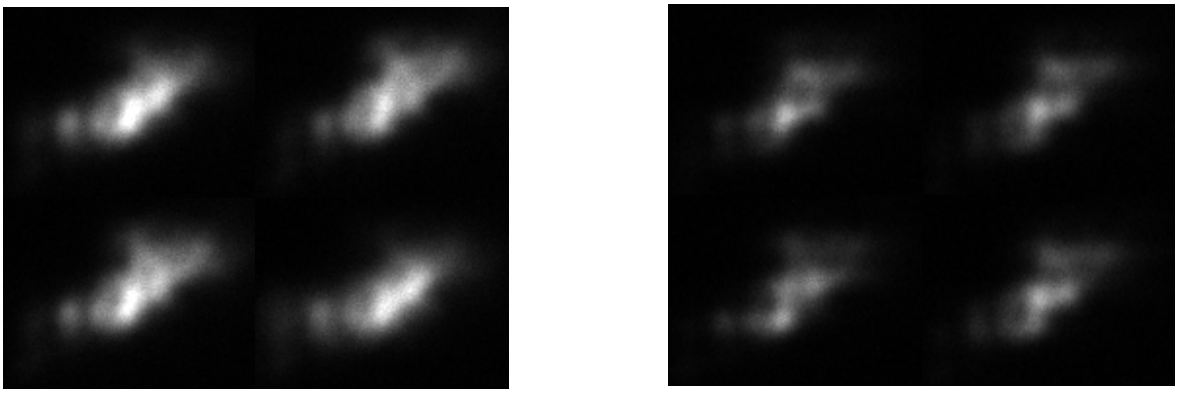

Figure (4.4) Striped and dim cold atomic cloud due to applied dithering (b) versus unlocked laser (a).

linewidth of the transition.

Therefore Doppler broadening is reduced ideally to a natural linewidth of an excited level (see Fig. 4.6(b)) and it is possible to lock a laser on it. We lock on a peak of $|\, F = 2\,\rangle \rightarrow |\, F = 3\,\rangle$ cross-over by means of a lock-in amplifier and a feedback loop. For this purpose the laser's frequency is modulated with a frequency Ω generated inside our homemade lock. If the laser's frequency is on the atomic peak, the probe's intensity has a modulation with twice the modulation frequency. In turn, when the laser is on a side, the modulation has a frequency Ω. In this case the error signal can be derived through the phase detection as the small laser's frequency deviation produces a positive or negative phase shift depending on a deviation direction. The phase detection is realized via a phase detector, where the signal from a detector is multiplied by an initial modulation signal and low pass filtered after.

Using this method the laser can be stabilized on a peak for days. However there is still one drawback. The built-in laser's modulation affects the magneto-optical trap density, as the laser dithers across the resonance. As we can see from Figure 4.4, the presence of modulation makes the atomic ensemble spatially modulated introducing inhomogeneity. The former can be mitigated by modulating atomic reference frequency. As an option one can apply a magnetic field to the atomic cell and modulate the current through magnetic coils instead of the laser current.

4.2.2 Dichroic atomic vapor laser lock

The method is called dichroic atomic vapor laser lock (DAVLL) and is based on the circular dichroism of an atomic vapour in the presence of a longitudinal magnetic field [103]. A linearly polarized light is sent through a Rubidium cell placed inside a solenoid (Fig. 4.3(b)). The degenerate hyperfine energy levels are split with an applied magnetic field in a particular way, namely that atoms will preferably absorb σ^- (σ^+) component from a red-detuned (blue-detuned) laser beam. The signals corresponding to different polarizations are separated on a circular polarizer. It consists of a quarter wave plate set to 45° and a polarizing beam splitter (PBS). Two outputs are sent on two separate photodetectors with similar responses. Their currents are subtracted from each other, generating a linear error signal for the small deviations of the laser frequency.

This method has a few salient advantages. First, it does not require to modulate a laser's current in contrast to lock-in. Moreover, there is no need to center the laser exactly on the absorption dip, since one can assign different weights to each photodetector's current before subtraction. The choice of any locking point is useful, in the case of the cooling process, as the optimal detuning of the laser is strongly connected to the number of atoms in the trap. Especially, the repumping transition is not well resolved compared to cooling (Fig. 4.6), and we choose the locking point based upon the brightness of the cloud.

We combined the DAVLL technique together with a saturated absorption in a single atomic cell (Fig. 4.3(b)). We built a simple feedback loop to control the central frequency of the ECLD via a piezo-actuator (circuit diagram is in Appendix E).

4.2.3 Optical phase-lock loop

The optical phase-lock loop (OPLL) keeps the frequencies locked, also it narrows the linewidth of the laser [104, 105], and this is crucial in phase-sensitive experiments. The operation of OPLL is based on a microwave phase-lock loop (PLL) chip, *ADF4107* is used here [105]. It compares phases between two radio-frequency signals and produces an error

proportional to their difference. For the phase locking of two independent optical sources they are mode-matched on a BS and sent on an ultrafast photodiode (*Hamamtsu G-4176*, Fig. 4.3(c)). The high frequency beating signal produced on a photodetector contains both the frequency and phase difference of two lasers: $\propto \sin(\Delta\omega \cdot t + \Delta\phi)$. We preamplify it to 0 dBm and send it together with the frequency reference in a PLL box. The frequency is divided by an adjustable factor, N(R), so the resultant frequency lies in an operational range of the chip *ADF4107* from 0 to 100 MHz. An error signal is split in two components: fast and slow, each modifies the corresponding feedback mechanism: an injection current and a voltage for a piezo-electric actuator.

This method establishes master-slave relations between two lasers. Keeping in mind the narrow line of *MBR-110*, the choice of Master laser is obvious. The second, cavity lock laser becomes phase locked to a master and could be at most 7 GHz detuned from the atomic resonance. The Raman strength of interaction is proportional to Ω^2/Δ, which produces significant coupling between the laser and atoms. We find it necessary to switch the laser off for the time of experiment. Another approach to overcome this coupling issue would be to design an experiment, where the role of the optical reference is taken by an ultra-stable cavity with all other lasers being locked to it [39]. The detuning could differ by many FSRs and is limited only by the coating of the mirrors.

The OPLL is easy to operate for two reasons: one, it does not require a high radio-frequency source due to frequency pre-scaling, two, it has a good stability, the laser can stay locked for hours. At the same time it has significant limitations: phase noise is too high for our purposes (Subsection 4.2.4) and the beating signal is limited by 7 GHz. I want to accentuate that these restrictions are related to the high phase noise sensitivity of our experiment, but it will perfectly suit many other experiments. In addition there are better analogs [106].

(a) (b)

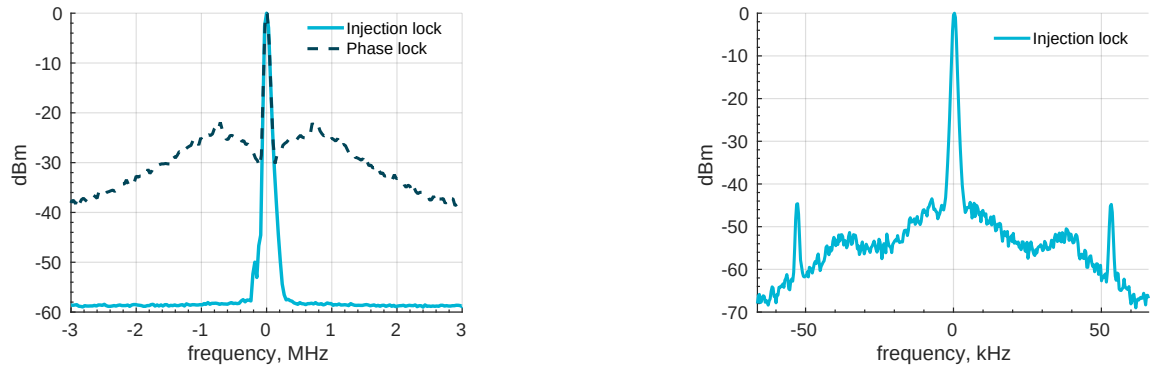

Figure (4.5) (a) Comparison of phase lock performance (dahed dark blue) versus injection lock (solid blue). The beating signal spectrum is offset to zero from the 6834 MHz, the spectrum analyzer settings are RBW=30 kHz, VBW=0.3 kHz. (b) The spectrum of a beating signal between *MBR-110* and ECDL *DL-100* set by means of the injection lock. RBW=1 kHz, VBW=30 Hz.

4.2.4 Optical injection locking

We have found that the phase noise of an ECDL laser locked with a PLL described above is too high to measure two-mode squeezing with two independent lasers as pumps. Its performance is presented in an original paper and in Figure 4.5(a), we estimate that the square of relative phase variation is 1.17 rad^2 (more details in Subsection 5.1.4). To reduce it further we implemented an injection locking technique.

We modulate the Master laser (*MBR-110*) with a fiber-coupled traveling wave EOM (*NIR-MPX800-LN-10, iXblue*), to achieve a sideband at exactly the frequency of the second pump. The 6.8 GHz microwave driving signal is derived from the PLL frequency synthesizer *ADF5355*, and subsequently amplified by MiniCircuits *ZVE-3W-83+* to achieve optimal sideband power. At the output of the modulator three frequencies are present: the original frequency or zeroth sideband and $\pm$ 1 sidebands, frequencies of which are different from the central by the amount of modulation frequency. The zeroth and -1 sidebands are filtered by the lens cavity [107], while the +1 sideband passes through the cavity and is sent into a slave laser (Fig. 4.3(d)).

The injection power should be high enough to saturate the gain of the slave diode, so it

will not amplify its own free running frequency [108]. Rather convenient for our purposes, we are able to establish the lock with only 20 μW of power, since we can have a significant drift of the lens cavity's central frequency and still remain the lock. The resulting linewidth of the ECDL is much narrower than the one obtained with the phase lock (Fig. 4.5(a)), and the central peak width is not resolvable with our spectrum analyzer (Fig. 4.5(b)). We expect it to coincide with the linewidth of the Master laser.

The astute reader will doubt if the second laser is necessary, since the +1 sideband has the correct frequency and the linewidth of the source already. The complication comes from the maximum obtainable power of this sideband, while the input power into the phase modulator should not exceed 20 mW. We have no more than a 1 mW of power, if we account for the insertion losses (20%), modulation depth (a side peak is approximately 35% of the zeroth), and lens cavity transmission (55%). Noting that this beam serves not only as a pump, but also as a local oscillator for the homodyne detection, thus it demands at least 15 mW of power.

4.3 Atomic system

Our experimental setup consists of a cold atomic Rubidium 87 with the key parameters summarized in Table 4.1. These alkali atoms have one valence electron and their spectrum follows the hydrogen-like formula (Balmer series). Their spectrum lies in a near infrared and has a simple structure with two optically-addressable lines, D_1 and D_2. All these properties make them favourable for various quantum optical experiments, such as quantum memories [109] and quantum simulators [110].

$\boldsymbol{n}$	$\boldsymbol{Z}$	$\boldsymbol{\lambda}_2$, nm	$\boldsymbol{\lambda}_1$, nm	$\boldsymbol{\gamma}/2\pi$, MHz	$\boldsymbol{\Delta}_{\mathrm{HFS}}$, MHz	$\boldsymbol{T}_{\mathrm{D}}, \mu$ K	$\boldsymbol{m}$, kg
5	37	780.24	794.979	6	6834.7	146	$1.44 \cdot 10^{-25}$

Table (4.1) Most important parameters of ^{87}Rb, where n is a principal number, Z an atomic number, $\lambda_{1,2}$ central wavelength of $D_{1,2}$ line, γ is an atomic linewidth, Δ_{HFS} is a hyperfine splitting, Doppler cooling temperature T_{D}, atomic mass m.

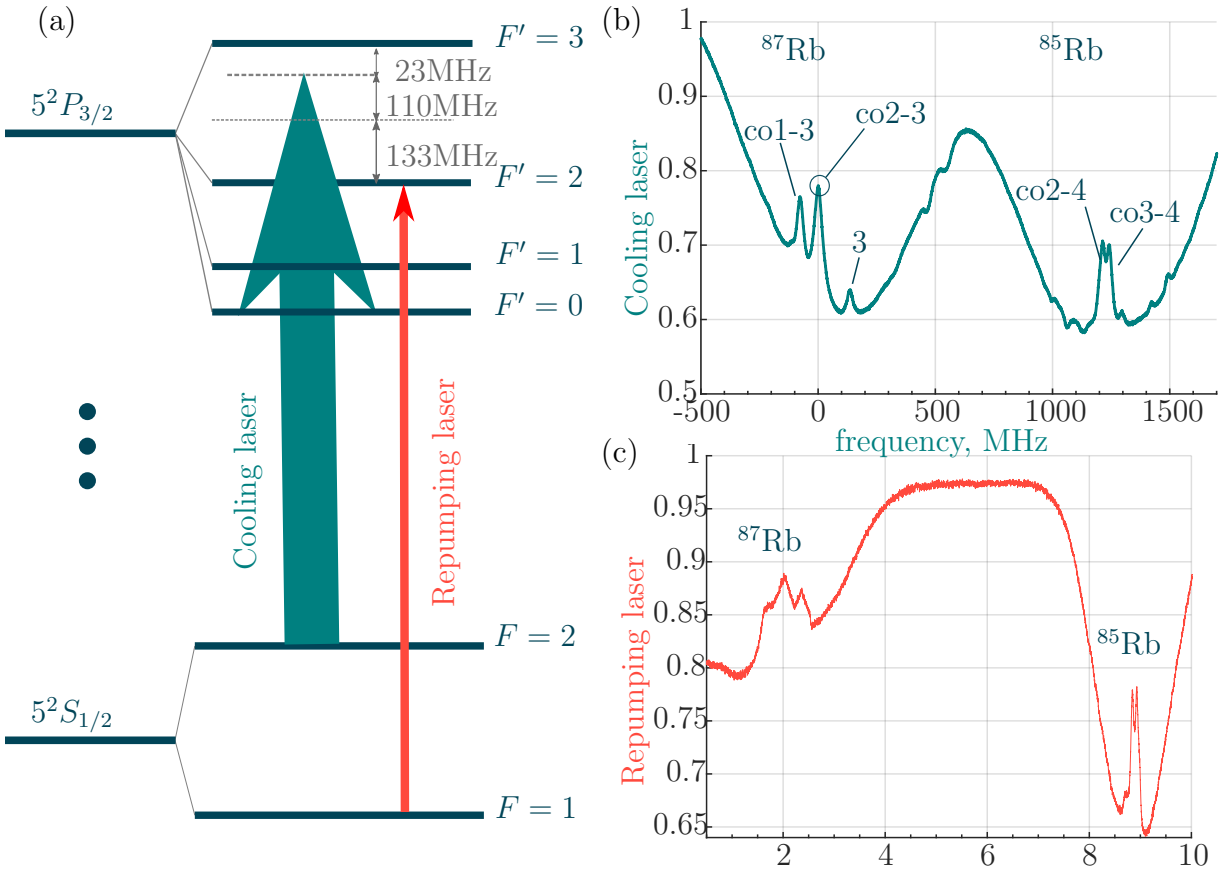

Figure (4.6) (a) D_2 Rubidium line is used for optical molasses. Six counter-propagating beams of cooling and repumping act on the corresponding $|\, F = 2\,\rangle \rightarrow |\, F' = 3\,\rangle$ and $|\, F = 1\,\rangle \rightarrow |\, F' = 2\,\rangle$ transitions. (b)–(c) Spectroscopy of D_2 line of the natural abundance of Rubidium isotope with 72.2% of ^{85}Rb and 27.8% of ^{87}Rb. Absorption peaks corresponding to each isotope are labeled. (b) Two transitions are present $|\, F = 2\,\rangle \rightarrow |\, F' = 1, 2, 3\,\rangle$ for ^{87}Rb and $|\, F = 3\,\rangle \rightarrow |\, F' = 2, 3, 4\,\rangle$ for ^{85}Rb. "co" means cross-over between two corresponding transitions. (c) The transition $|\, F = 1\,\rangle \rightarrow |\, F' = 0, 1, 2\,\rangle$ of ^{87}Rb

The cold atomic cloud is obtained via Doppler cooling inside a magneto-optical trap. There are a few motivations why we are going to the trouble of operation at ultra-high vacuum to prepare atoms. The first negative factor we want to avoid is the Doppler broadening, which is proportional to the square root of temperature and it drops below the natural linewidth at the Doppler temperature. The full-width at half-maximum (FWHM) is given by $\Delta\nu = \nu_0\sqrt{\frac{8\ln 2 k_\mathrm{B}T}{mc^2}}$ [111, Ch. 1, p. 6]. The second negative effect is the time of flight, meaning that an atom will escape the area of interaction before the experimental sequence is finished. We work with a cavity mode with a diameter of 100 μm. The velocity of a hot gas ranges from 100 to 1000 m/s, for the Doppler cooled atoms it is as low as $v_\mathrm{rms} = \sqrt{\frac{3k_\mathrm{B}T}{m}} \approx 20$ cm/s. The resulting time an atom will stay in the interaction zone is 1 μs versus 0.5 ms for cooled atoms. This time is estimated from the residual movement of atoms not including the gravitational acceleration.

We utilize the standard magneto-optical trap (MOT), which is well described in textbooks such as [112, 113]. MOT includes two lasers working on the D_2 line and two magnetic coils creating a quadrupole trap. Six counter-propagating beams of cooling and repumping act on the corresponding $|\,F=2\,\rangle \rightarrow |\,F'=3\,\rangle$ and $|\,F=1\,\rangle \rightarrow |\,F'=2\,\rangle$ transitions, as can be seen in Figure 4.6. The Doppler temperature is determined by the linewidth of cooling transition γ and is given by $T_\mathrm{D} = \frac{\hbar\gamma}{2k_\mathrm{B}}$, and equal to 146 μK for ^{87}Rb.

4.3.1 Optical molasses

Typically ^{87}Rb is cooled on the D_2 line, since it has a closed transition $|\,F=2\,\rangle \rightarrow |\,F'=3\,\rangle$. Atoms excited by the resonance beam are prohibited to spontaneously decay on a dark $|\,F=1\,\rangle$, due to selection rules for the dipole transitions $\Delta F = \pm 1$. The cooling laser is centered on the corresponding wavelength $\sim$ 780.246 nm. By monitoring the saturated absorption spectroscopy we lock the laser frequency to a strong cross-over peak between $|\,F'=2\,\rangle$ and $|\,F'=3\,\rangle$ (see Fig. 4.6). An additional AOM with a central frequency 110 MHz decreases detuning to an approximately optimum value of $\gamma/2$. Despite that the spontaneous

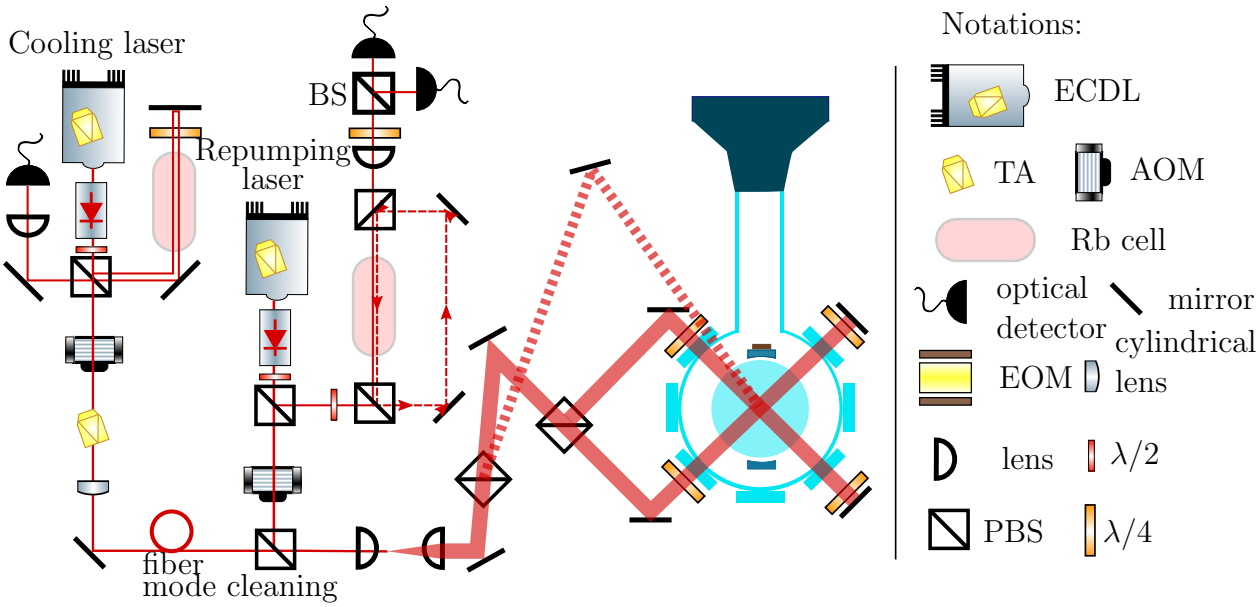

Figure (4.7) A simplified layout for the optical molasses. Each laser is locked to a corresponding rubidium transition. After that they are modulated with AOM to perform switching. Cooling laser additionally passes through a TA, it generates an elliptical mode, which we compensate with a cylindrical lens and a stage of a fiber mode cleaning. We use a polarization maintaining fiber, as we require a certain polarization for the cooling process. Beams from both lasers are combined on a BS, their sizes are expanded in a telescope, they are split into three beams: two horizontal (solid red) and one vertical (dashed red). Polarizations of the lasers are changed from linear to $\sigma_{\pm}$ with QWP. Three mirrors from the opposite side of the vacuum chamber produce reflected beams for a complete optical molasses.

decay from $|\, F = 3 \,\rangle$ on $|\, F = 1 \,\rangle$ is prohibited, atoms can fall into this "dark" state through the detuned transition $|\, F = 2 \,\rangle \rightarrow |\, F' = 2 \,\rangle$ induced by the strong cooling laser [111]. Thus, the repumping laser is required for the cooling process to succeed. It is centered at wavelength ~ 780.232 nm to address $|\, F = 1 \,\rangle$ on $|\, F' = 2 \,\rangle$ transition. We adjust the central wavelength via saturated absorption spectroscopy (Fig. 4.6) and we lock this laser at the brightest point of our cloud via DAVLL (see subsection 4.2.2).

In order to produce six counter-propagating beams, we mode-match both laser beams on a BS. We send them through the same telescope in order to expand the diameters up to 1 cm. Larger diameter keeps the power homogeneous in the central area and allows easier alignment. We split the combined beam into three and send it into three orthogonal directions through the center of the vacuum chamber (Fig. 4.6). These beams are back reflected from the mirrors on the opposite side of the chamber and form the three dimensional optical molasses.

The repumping laser power should be kept above the saturation ($I_{\text{sat}} = 1.6$ mW/cm^2 [67]), and is equal to 17 mW. We noticed that by increasing the power of cooling laser, we see brighter fluorescence until we hit the limit of the ECDL power, which is 50–60 mW of continuous-wave power. We use a tapered amplifier (*EYP-TPA-0780-0100-3006-CMT03-0000*) to increase the ECDL power further. We have experimentally found that an optimum brightness of the cloud corresponds to 60 mW of cooling laser near the vacuum chamber (20 mW in each beam).

4.3.2 Magnetic trap

Two magnetic coils, with a diameter of 8 cm and 63 turns each, are used to form a quadrupole trap. We position them 10 cm apart to leave a 1 cm gap between each coil and the vacuum chamber. Their resistance is 0.4 Ω and inductance 900 μH. Our power supplies are limited by 10 A of a constant current, and we set the current through each coil to approximately 9 A not to hit the maximum power available while the coils heat. This

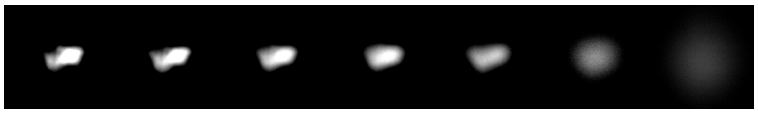

Figure (4.8) Free expansion of a cold atomic cloud viewed with a camera with a certain delay: 0, 100μs, 500μs, 750μs, 1000μs, 2000μs, 3500μs.

results in the magnetic field gradient around 20 G/cm.

Besides creating a magnetic trap, coils help us to move the cooled atomic cloud in six directions. We power the coils independently with a separate constant current supply, and this gives us control over the cloud's vertical position. We rigidly fix them adjacent to a dovetail optical rail and place it on top of two orthogonal translation stages. We will reposition an atomic cloud having all this three degrees of freedom and optimizing overlap between cavity mode (see Section 5.2).

These coils have no water cooling to dissipate generated 32 W of heat, thus we installed two small fans in order to slow down the temperature growth at 50°C. These temperature changes strongly affect our cavity length and in a long term its alignment. As a further possible improvement of our setup would be installing water cooling system. Another option of a slight modification, which can improve significantly the performance is exchanging these coils with rectangular-shaped. This is a way to generate a cigar-shape cloud, which can have very high atomic densities [44] and will have better overlap with a cavity mode due to its elongated shape.

4.3.3 Temperature measurement

We visualize our atomic cloud with a camera (*UI-2230SE-M-BG*) collecting fluorescence photons. This camera has an option of an external triggering. We measured an expansion of our atomic cloud by switching off both lasers and sending a trigger signal to a camera after an adjustable delay (Fig. 4.8). We fitted the captured density distribution with a Gaussian function $e^{-\frac{(x-x_0)^2}{\sigma_x^2}} + e^{-\frac{(z-z_0)^2}{\sigma_z^2}}$ and knowing pixel per mm, we found the actual atomic sizes σ_x and σ_z. We have modeled our atomic cloud to have velocities to follow Maxwell-Boltzmann

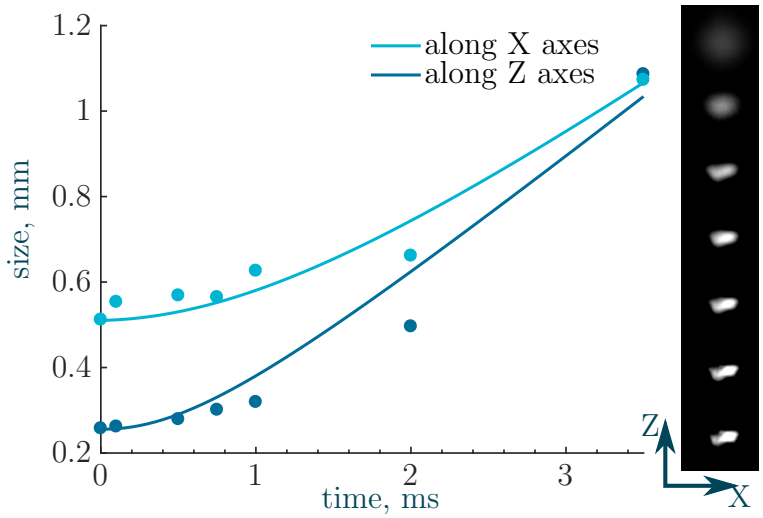

Figure (4.9) Free expansion of an atomic cloud. We averaged over 100 images to obtain each point for a certain delay. The fitted curves are found numerically and correspond to temperatures of 37 and 60 μK. The acceleration of free fall is collinear with z axes and points in opposite direction.

distribution (Fig. 4.9). For two directions we had to use slightly different temperatures for the best fit of experimental data: $T_z = 37 \pm 5\mu\text{K}$ and $T_x = 60 \pm 7\mu\text{K}$. We attribute this difference to the initial shape of the cloud. We intentionally mismatch the cooling beams to obtain an elongated shape, since it maximizes overlap between atoms and a cavity mode. A disbalanced molasses force in a horizontal plane leads to a higher temperature compared to vertical direction. It is worth noticing that these temperatures are well below the Doppler limit and this is not surprising as a sub-Doppler cooling mechanism is present [114]. This is the so-called Sisyphus cooling [115] with a temperature limit of $T_\text{R} = \frac{(\hbar k)^2}{2mk_\text{B}}$.

4.4 Cavity

To enhance light-atom interaction we use a Fabry-Perot cavity which consists of two plano-concave mirrors. The enhancement comes from the multipass nature of the resonator, where light bounces back and forth between the mirrors and hence interacts with the media multiple times till it escapes the cavity. Below we present a simple model for internal/reflected electric field amplitudes within/from the cavity. The model allows us to calcu-

late the cavity spectrum and how it depends on mirror reflectances.

4.4.1 Cavity spectrum

The simplest model to describe energy relations in the cavities with a lossy medium inside are derived by summing up contributions of infinite round trips [116, p. 36]. We consider a cavity consisting of two mirrors with reflection and transmission coefficients r_1, r_2 and t_1, t_2. They are separated by a distance L. Between them we place a lossy medium with transmission coefficient t (Fig. 4.10(a)). The incident field E_{in} is partially transmitted $E_{\text{in}}t_1$ and reflected $-E_{\text{in}}r_1$. After the first round trip we add to the reflected field a portion of $E_{\text{in}}t_1^2t^2r_2e^{i\phi}$, and generalizing it to the nth round-trip $E_{\text{in}}t_1^2r_1^{n-1}t^{2n}r_2^ne^{in\phi}$. Thus the total reflected field is the sum of a geometric progression:

$$E_{\text{refl}} = -E_{\text{in}}r_1 + \frac{E_{\text{in}}t_1^2}{r_1}\sum_{n=1}^{\infty} r_1^n t^{2n} r_2^n e^{in\phi} = E_{\text{in}}\frac{r_2t^2e^{i\phi} - r_1}{1 - r_1r_2t^2e^{i\phi}}, \tag{4.1}$$

where ϕ is a round trip phase obtained by a field. The reflected intensity is the squared modulus of the field:

$$I_{\text{refl}}(\phi) = I_{\text{in}}\frac{(r_1 - r_2t^2)^2 + 4r_1r_2t^2\sin^2(\phi/2)}{(1 - r_1r_2t^2)^2 + 4r_1r_2t^2\sin^2(\phi/2)}. \tag{4.2}$$

Extrema of this function give minima at $\phi/2 = \pi l$ and maxima at $\phi/2 = \pi/2 + l\pi$, where l is an integer. The minimum for the reflected intensity corresponds to the resonant condition, when transmission and circulating power are maximum. The phase obtained by a wave during the round trip could be rewritten in quantifiable notations: $\phi/2 = \frac{2\pi\nu}{c}(n_1(L - d) + n_2d) = \frac{2\pi\nu}{c}L^*$, where n_1 (n_2) is a complex refractive index of a bare cavity (inserted medium), ν is a central frequency of an incident electromagnetic field. The period of this function in the frequency domain is $\Delta\nu = \frac{c}{2L^*}$, for the empty resonator it has a more recognizable form: FSR $= \frac{c}{2Ln}$. The free spectral range (FSR) is the frequency spacing between two adjacent longitudinal modes.

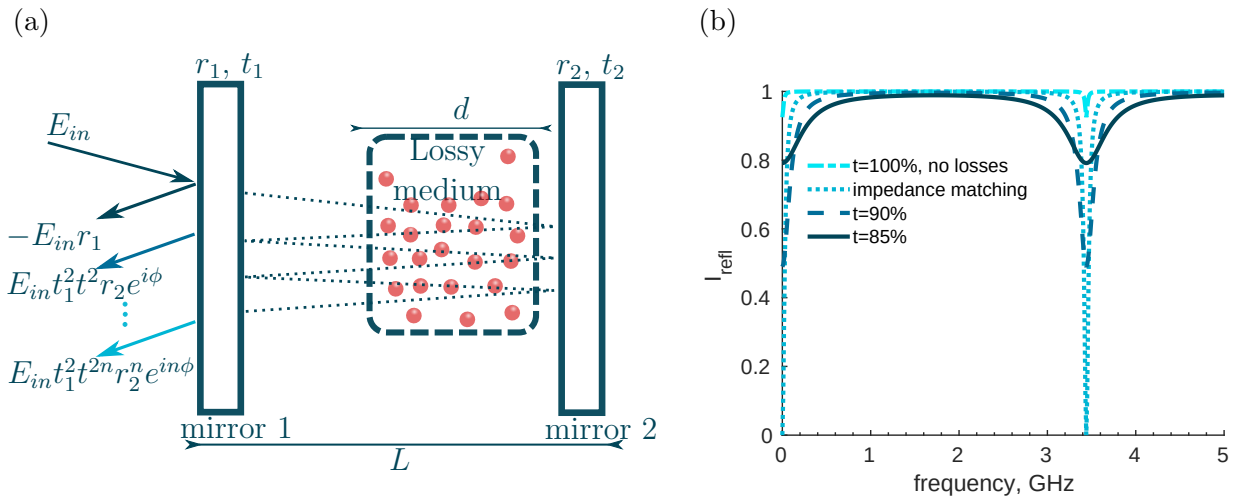

Figure (4.10) (a) Schematically shown a cavity. Two mirrors are spaced at the distance L, the lossy medium inside occupies part of the cavity d (b) Reflected spectrum for different medium transmission coefficients.

We can notice a special regime, when the resonance $\phi/2 = \pi l$ coincides with a condition $r_1 = r_2t^2$, from formula (4.2) follows that the reflected intensity is zero. This phenomena is called impedance matching and it is an optical analog to a well-known effect in electronics. In electronics the maximum power transfer or minimal reflection from the load is achieved if the impedances of the load and the source are matched. The close analogy is pertinent for the optical resonators, as could be easier seen if we rewrite the condition above as follows: $1-r_1^2 = 1-(r_2t^2)^2$. The left hand side is the energy entering the system, the right hand side is a sum of losses inside the cavity and through the second mirror. All told, by matching the rate at which we pump the cavity to the overall losses, the circulating power is maximum and the reflection is zero.

Analogously to a reflected field we can find the field inside the cavity including the dependence on the coordinate x along the cavity mode. The superposition of two counter-propagating fields is:

$$\begin{aligned} E_c &= t_1E_{\text{in}}e^{ikx}\sum_{m=0}^{\infty} r_1^m r_2^m e^{2imkL} + t_1r_2E_{\text{in}}e^{-ik(2L-x)}\sum_{m=0}^{\infty} r_1^m r_2^m e^{-2imkL} \\ &= t_1E_{\text{in}}e^{ikx}\left(\frac{1}{1-r_1r_2e^{2ikL}} + r_2e^{-2ikL}\frac{1}{1-r_1r_2e^{-2ikL}}\right) \end{aligned} \tag{4.3}$$

The wavevector $k = \frac{2\pi(\nu+\delta)}{c}$, where $\nu = m \cdot \mathrm{FSR}$ is a frequency resonant with the cavity, δ is a detuning from resonance, m is an integer, the length of the cavity in terms of FSR $L = \frac{c}{2\mathrm{FSR}}$. Thus, $e^{2ikL} = e^{2\pi i \frac{\delta}{FSR}}$:

$$E_\mathrm{c} = t_1 E_\mathrm{in} e^{ikx} \left(\frac{1}{1 - r_1 r_2 e^{2\pi i \frac{\delta}{FSR}}} + r_2 e^{-2\pi i \frac{\delta}{FSR}} \frac{1}{1 - r_1 r_2 e^{-2\pi i \frac{\delta}{FSR}}} \right) \tag{4.4}$$

If we consider the resonant condition with $\delta = 0$, then the resultant field forms a standing wave:

$$E_\mathrm{c} = 2t_1 \cos kx \frac{1 + r_2}{1 - r_1 r_2} E_\mathrm{in}, \quad \text{and} \quad I_\mathrm{c} = 4t_1^2 \cos^2 kx \left(\frac{1 + r_2}{1 - r_1 r_2} \right)^2 I_\mathrm{in}. \tag{4.5}$$

One more commonly used parameter to describe a cavity is finesse, by a definition it is a ratio between FSR and a cavity linewidth κ: $\mathcal{F} = \frac{\mathrm{FSR}}{\kappa}$. It is fully described by the cavity losses: $\mathcal{F} = \frac{\pi\sqrt{r_1 r_2 t^2}}{1 - r_1 r_2 t^2}$ and gives an average number of photon's round trips before it escapes the cavity. This brief introduction to the cavity spectrum lays the sufficient basis for our forthcoming discussion.

4.4.2 Parameters for the cavity

After we have introduced all the basic characteristic of the cavity, we can intelligently choose them. We deduce three restrictions on the parameters: both emitted photons must be simultaneously in resonance with a cavity, photons should leave the cavity from one most likely port, and an atom-light coupling constant is maximized. The last requirement can be addresses if we exclude all the constants from the definition of cooperativity[1] to observe the major dependencies: $C \propto \rho l_\mathrm{a} \mathcal{F} \lambda^2$, where ρ is an atomic density, l_a is a length of an atomic ensemble, λ is a central wavelength of an atomic transition. Assuming the atomic transition to be fixed, we have to target for the highest finesse and atomic density. As was mentioned

[1]The definition of cooperativity is $C = \frac{4Ng_0^2}{\kappa\gamma} \propto N\frac{\mathcal{F}}{w_0^2}\lambda^2 = \rho l_\mathrm{a}\mathcal{F}\lambda^2$, where w_0 is the waist of the cavity, N is a number of atoms interacting with a cavity mode, γ is an atomic decay rate.

previously, the ultra-high atomic densities are achieved in a cigar-shape cloud [44], while an effective 2D shape makes overlap between atomic cloud and a cavity mode optimal.

First of all, the FSR of the cavity is selected in such a way that the cavity is simultaneously in resonance with the Stokes and anti-Stokes photons (Fig. 2.6). This condition can be fulfilled when integer number n of FSR is equal to their frequency difference: $n \cdot \mathrm{FSR} = \omega_1 - \omega_2$. At the same time our Λ-scheme dictates this frequency difference to be $\Delta_{\mathrm{HFS}} + \delta$, in notations from Section 2.4. The detuning δ is the variable parameter, which could easily be in a range from 20 MHz to 1 GHz. In our final version $\delta = 59$ MHz and the condition to fulfill is $n \cdot \mathrm{FSR} \approx \Delta_{\mathrm{HFS}}$ (Subsection 4.4.3). Although the length of the cavity is dictated by our vacuum chamber. So it possible to have it in a range of 2–10 cm. One more thing to consider is the phase difference between two modes. Two standing waves for photonic modes will have a phase difference at the center of the cavity $\Delta\phi = \frac{2\pi n \cdot \mathrm{FSR}}{c}\frac{L}{2} = \frac{\pi}{2}n$. For even n two standing waves have simultaneously antinodes at the center of the cavity, for odd n one will be maximum, while the second wave is zero. Thus to ensure phase-matching we set $\mathrm{FSR} = (\Delta_{\mathrm{HFS}} + \delta)/2$ and the length of the cavity equal to 4.4 cm.

We used the mirrors with different reflectances $R_1 = 95\%$ and $R_2 > 99.99\%$ for the purpose of collecting the signal from one most likely port. If we assume no losses inside the cavity, then the finesse depends only on reflectances and is $\mathcal{F} = \frac{\pi \sqrt[4]{R_1 R_2}}{1-\sqrt{R_1 R_2}} = 122$. Knowing this we find the linewidth of the cavity, $\kappa = 30$ MHz, which dominates both atomic decay rate and collective Rabi frequency $\kappa > \sqrt{N} g_0, \gamma_{13}$. These time scales are attributed to the bad cavity regime, which is desirable in our experiment, as the fast cavity decay guarantees that generated photon escapes the cavity, before it gets reabsorbed. The parameters of the cavity are summarized in Table 4.2.

4.4.3 Assembly

We have decided that if we place our cavity mirrors outside of the vacuum chamber, the losses induced by two windows will significantly reduce the repetition rate of photons

$\mathcal{F}$	**FSR,** MHz	**Linewidth,** MHz	**Waist,** μm	**Curvature,** mm	$\boldsymbol{R}_1$, %	$\boldsymbol{R}_2$, %
93	3446	34	86	60	95	99.99

Table (4.2) Summarizing parameters of the cavity. The value for the finesse is measured in an experiment.

generatation. To have a rough estimate of the decline, we assume that each window has an antireflection coating for a B-band, that reduces the reflectance approximately by 0.19% per surface for our wavelengths. Thus, the total reflection for a round trip from two windows is $R_{\text{avg}} = 1.5\%$ and the expected finesse of 120 drops to 93. Moreover, one has to differentiate the spurious losses inside the cavity from the "good" losses from the output port, which leads to an emission of our photonic modes toward the detector. In Section 2.2 we separately include the spurious loss and loss on the output coupler. Please note, that this critique stands, although the best experiments with cold atomic cloud and the cavity, are performed with mirrors being outside of the vacuum chamber [41].

Thus we have designed cavity holders , which were glued inside of the vacuum chamber together with cavity mirrors *#109765* and *#107808* from layertec (Fig. 4.2 and Fig. 4.11). The output coupler mirror is glued to a hollow cylinder, which had a few holes from the sides to evacuate a volume between a cavity mirror and a chamber's window. All parts were machined from stainless steel at the University's workshop.

The second rear mirror should be placed rigidly inside a long glass tube. For this we manufactured a holder consisting of three long rods, screwed together to a wheel type part, so they form a triangle from a side, as shown in Figure 4.11. The vacuum tube has a slightly varying diameter, it gets smaller toward the spherical part, to compensate for that we decided to put springs into rods. The commercially produced spring plungers were installed to face a glass tube and push towards it. One more complication was to be able to set a length of the cavity to a desired value of 4.4 cm (FSR $= \frac{\Delta_{\text{HFS}}}{2}$), to overcome this we put a mirror on a plastic screw, which is reachable by a long screw driver through all the vacuum chamber. This "fine" adjustment is enough as we have free parameter–detuning δ.

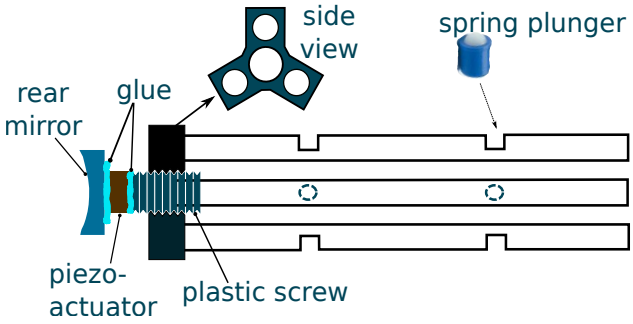

Figure (4.11) A rear mirror holder design.

To put it all together, we started with gluing mirror towards piezoelectric actuator (*TA0505D024 -Thorlabs*). Afterwards we attached them to a screw constantly monitoring the back reflection to keep them all aligned as a piece. Subsequently we placed our complex structure with a front mirror into a mirror holder and on a 3-axis stage, we brought it close to a vacuum chamber, so the front window and the chamber were touching. We aligned the resonator to have one spatial mode, optimized its length and fixed the front mirror in place with a few layers of glue. We precisely measured the free spectral range after bake out with two separate lasers locked to each other with a detuning of two FSR. All the resulting parameters are in the Table 4.2.

4.4.4 Pound-Drever-Hall Lock

We keep the cavity always in resonance with Stokes and Anti-Stokes photons by applying an active stabilization. The stabilization is realized via the well-known Pound-Drever-Hall (PDH) technique [117], which requires a phase-sensitive detector and a feed-back loop. If we modulate the central frequency of our laser, we will have two sidebands outside of the linewidth of a cavity. Since the reflected field from a cavity has a dispersive phase, we can distinguish between "in resonance", where a phase is zero, and "out of resonance," where a phase has different signs depending on length of a cavity mismatch.

To quantitatively describe the PDH locking, let us first consider an input light with amplitude E_{in} and angular frequency ω_0 after phase modulation with depth β and frequency

Ω. Using Jacobi–Anger expansion and ignoring higher frequency sidebands, the light can be expressed as

$$E = E_{\text{in}} e^{i(\omega_o t + \beta \sin \Omega t)} = \sum_n J_n(\beta) e^{in\Omega t} \approx E_{\text{in}} e^{i\omega_0 t} \left(J_0 + J_1(\beta) e^{i\Omega t} + J_{-1}(\beta) e^{-i\Omega t} \right), \tag{4.6}$$

where $J_n(\beta)$ is the nth order Bessel function of the first kind. The reflected light from the cavity is transformed by complex amplitude conversion factor $F(\omega)$:

$$F(\omega) = \frac{-i(\omega - \omega_{\text{c}})}{\kappa + i(\omega - \omega_{\text{c}})}, \tag{4.7}$$

where ω_{c} is the cavity resonant frequency, where κ is cavity inverse photon lifetime.

Taking into account the phase modulation, the light reflected from the cavity takes the form:

$$E_{\text{ref}} = E_{\text{in}} \left(F(\omega_0 + \Omega) J_1(\beta) e^{i\Omega t} + F(\omega_0 - \Omega) J_{-1}(\beta) e^{-i\Omega t} + F(\omega_0) J_0(\beta) \right) \tag{4.8}$$

Resulting interference of the sidebands and zero order are represented by two harmonics with frequency Ω and 2Ω. The first harmonic is

$$\begin{aligned} |\, E_{\text{ref}} \,|^2 = {} & I_{\text{in}} J_1(\beta) J_0(\beta) \left(F^*(\omega_0) F(\omega_0 + \Omega) e^{i\Omega t} + F(\omega_0) F^*(\omega_0 + \Omega) e^{-i\Omega t} \right) \\ & + I_{\text{in}} J_{-1}(\beta) J_0(\beta) \left(F^*(\omega_0) F(\omega_0 - \Omega) e^{-i\Omega t} + F(\omega_0) F^*(\omega_0 - \Omega) e^{i\Omega t} \right), \end{aligned} \tag{4.9}$$

where $I_{\text{in}} = |\, E_{\text{in}} \,|^2$ is the intensity of the incident light. If modulation frequency is much larger than a cavity's linewidth, than $F(\omega_0 \pm \Omega) \approx -1$ and taking into account Bessel's function properties $J_{-1}(\beta) = -J_1(\beta)$, the signal becomes

$$\begin{aligned} |\, E_{\text{ref}} \,|^2 &\approx 2i I_{\text{in}} J_1(\beta) J_0(\beta) \left(F^*(\omega_0) - F(\omega_0) \right) \sin \Omega t \\ &= 4 I_{\text{in}} J_1(\beta) J_0(\beta) \text{Im}(F(\omega_0)) \sin \Omega t. \end{aligned} \tag{4.10}$$

The amplitude of the first sideband provides the dispersion information. Thus the subsequent mixing of the photodetector's output with LO derived from RF modulation extracts frequency depending error signal $\mathrm{Im}(F(\omega_0))$.

The PDH technique is known to be shot noise limited [117], it means, that signal-to-noise ratio scales as square root of applied power. Below we quantify the locking range assuming the experimental parameters. The goal is to determine the change of harmonic's amplitude for cavity frequency deviation. If we assume small frequency displacement from the cavity resonance $\delta\omega = \omega_0 - \omega_s \ll \kappa$, the signal power can be expressed as

$$\mathcal{S} \sim 8 I_{\mathrm{in}} J_1(\beta) J_0(\beta) \frac{\delta\omega}{\kappa} R, \tag{4.11}$$

where R is photodetector responsivity. The main noise source is the shot noise, which has flat spectrum with the density $2eRI_{\mathrm{in}}$, where e is an electron charge. If the lock has bandwidth f, the signal to noise ratio is

$$\frac{\mathcal{S}}{\mathcal{N}} = \frac{8\sqrt{RI_{\mathrm{in}}} J_1(\beta) J_0(\beta)}{\sqrt{2ef}} \frac{\delta\omega}{\kappa}. \tag{4.12}$$

Therefore minimal locking stability range can be derived from Equation (4.12) for $\frac{\mathcal{S}}{\mathcal{N}} = 1$. The modulation for locking laser is achieved via laser diode current modulation through a bias-T circuit. In contrast to "pure" phase modulation via EOM the current modulation is accompanied by stronger amplitude modulation especially for larger β. To keep the laser's amplitude stable small modulation depth $\beta \approx 8 \cdot 10^{-4}$ is used.

We send 10 μW of power into a cavity mode, which is partially reflected and 200 nW reaches a commercial photodetector (*PDA8A*), and then we send it through two stages of amplification (*ZFL-500LN* and *ZFL-500*)[2]. The PI circuit provides averaging over 1 ms, what is reasonable with characteristic response time of cavity piezo transducer. Schematics for locking electronics can be found in Appendix (D.1). Plugging values into (4.12), we

[2]Following the Friis formula [118], the proper order is to place primarily low noise amplifier.

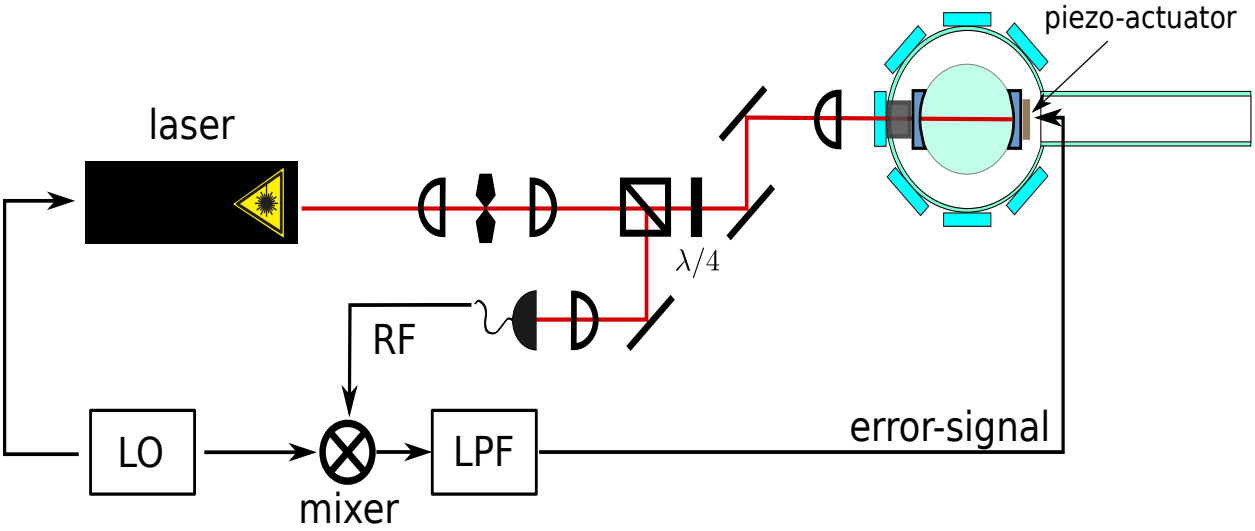

Figure (4.12) A conceptual scheme of Pound-Drever-Hall. A laser is modulated by the frequency lying outside of a cavity linewidth. A laser beam reflects from a cavity and goes on a photodetector, a radio-frequency (RF) signal is sent to a mixer, where it is multiplied by a local oscillator (LO), and after passing through a low pass filter (LPF) voltage is applied to a piezo-actuator.

obtain, that $\mathcal{S}/\mathcal{N} > 1$ for $\delta\omega > 0.5$ MHz.

4.5 Pulse sequencer

4.5.1 Experiment timing

Our experiment runs in stages. We start with an atomic cloud preparation, after switching the magneto-optical trap off we send an optical pumping pulse, which is followed by an experimental sequence. During the last stage we send two pumps either simultaneously or with a variable delay. When the cloud is dispersed, we repeat these stages all over (Fig. 4.13).

To perform such a versatile design cheap we constructed a signal generator of a pair of direct digital synthesizers (*AD9959*) and micro-controllers (*Arduino DUE*). Each direct digital synthesizer has four channels of a sine signal with frequencies up to 200 MHz. One can sweep frequency and amplitude, or switch them between many levels independently. To prepare an optical pulse we use an acousto-optical modulator from *Isomet* in each path.

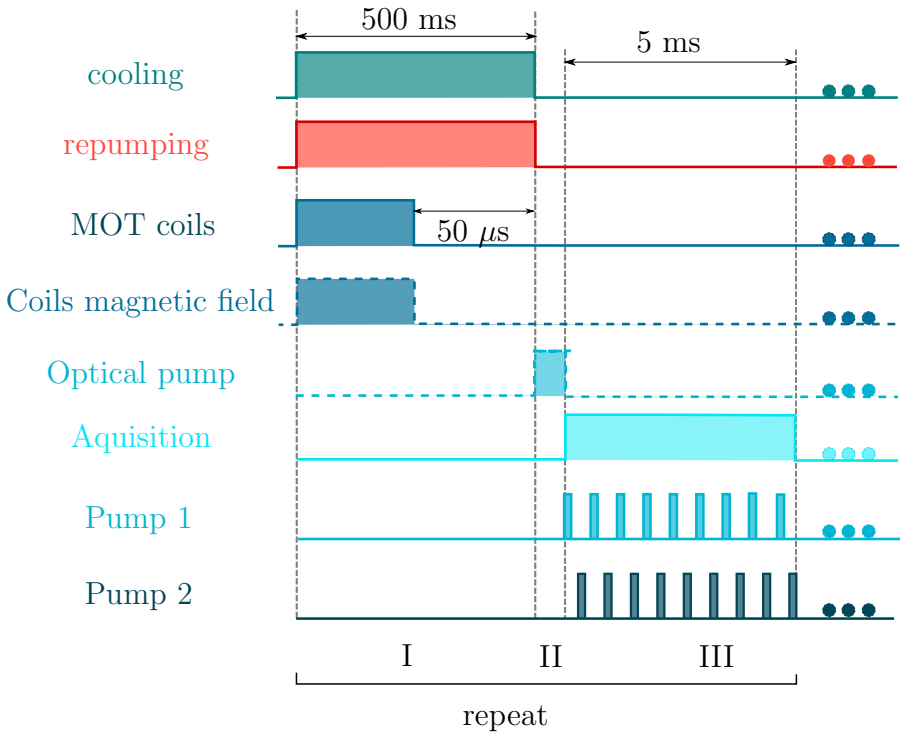

Figure (4.13) Experimental timing stages: (I) preparation of cold atomic cloud, (II) optical pumping, (III) series of pump cycles. Dots mean that this cycle repeats continuously.

The shortest pulse we can obtain is determined by an acoustic wave velocity of the material and the beam size. As an example, model *1205c-X* has a Lead Molybdate crystal with the acoustic velocity is 3.63 mm/μs. The typical focused beam size is 100 μm leads to an estimate rise time of 30 ns. The shortest pulses we have been working with in an experiment were 200 ns long.

The first stage of atomic cloud preparation takes 500 ms, while two lasers and coils work simultaneously. After that we switch off the magnetic coils, wait for 50 μs and switch off one of the cooling lasers. Depending on which level we want to polarize the ensemble, we keep either repumping for an extra 30 μs, thus atoms are pumped on $|\,F = 2\,\rangle$; or we keep the cooling laser longer on, so the atoms are mainly on $|\,F = 1\,\rangle$.

4.5.2 Magnetic coil switch

We employ a magnetic switch with relative fast switching time and suppressed eddy currents. Suppression of Eddy current is important, since the rapid change of current through the coils, such as switching, produces a burst of magnetic field. Such bursts are not desired, since they wash out atoms from the MOT region. The symmetrical electrical circuit employs use of two stage switching of transistor for each coil (see Fig. F.1) and is based on [119].

The switching function for high current going through the coil is realized via *PNP BJT MJ 2955* transistor. The base currents of the transistors are controlled by *TIP31C* NPN transistor. In turn, an input voltage is converted into *TIP31C* base current by a comparator based on operational amplifier *OPA137PA*. It isolates the switching circuit from the pulse controller input impedance. High CMOS level of input voltage saturates the comparator, what changes the emitter-collector resistance of *TIP31C* transistor. Therefore the base of *MJ2955* is shortened on a ground trough 1 Ω resistor opening the emitter-collector path and allowing a current to go through the coils $L_{1,2}$. The low level of the input voltage closes *TIP31C* and consequently put a high voltage on base of PNP, what closes current through the coils.

The performance of this circuit is shown in Figure 4.14. An expected switching time scales as the ratio between inductance and resistance and is 2 μs for our coils. The switching off time is suppressed to 8 μs and could be seen on the inset. We switch off the magnetic coils 50 μs prior to cooling and repumping lasers. The rise time for the coils is 200 μs, although it doesn't affect our experiment, as we are not optimizing a repetition rate.

4.6 Homodyne detection

Currently, there are two common approaches to acquire quantum statistics in optics: it is either in the Fock basis or in continuous quadrature basis. Most of the detectors for measurement in the Fock basis, such as single photon avalanche photodiodes, only distinguish

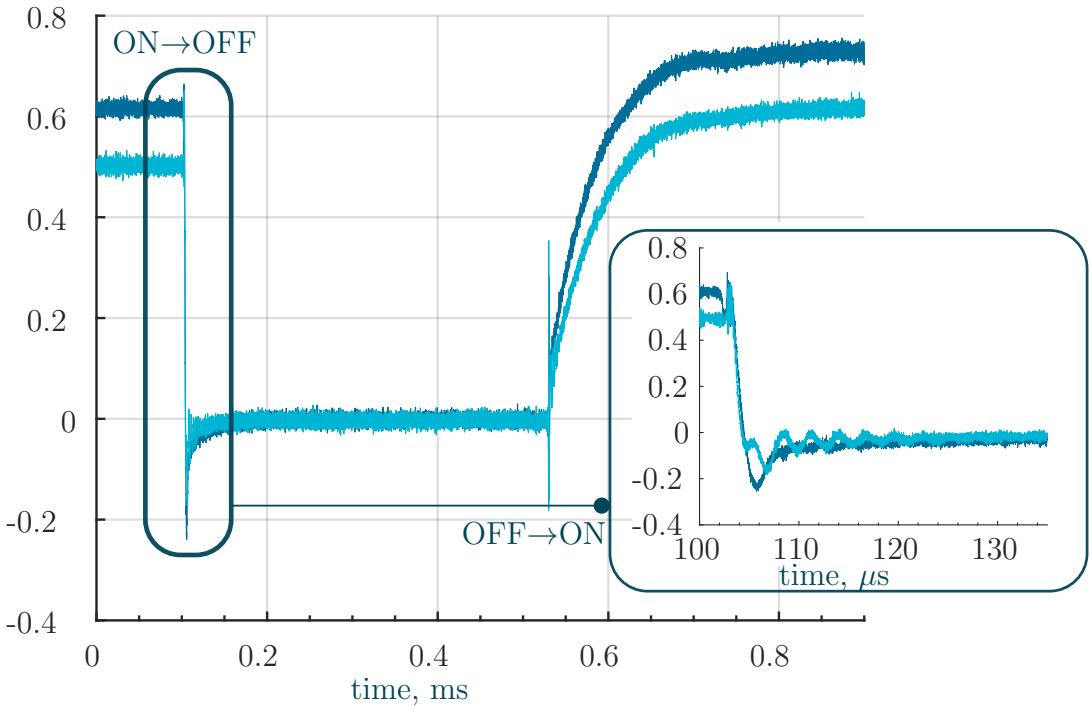

Figure (4.14) In this figure we demonstrate a voltage across a small resistance connected in series with one of the two coils. We switch off (ON→OFF) our coils at 100μs and monitor how quickly the voltage will drop to zero (for enlarged image see inset). We switch the coils back on (OFF→ON) at 500 μs. Two different colors correspond to lower and upper coil.

vacuum from all other possible excitations, meaning that the detector "clicks" for one or any number of photons in a pulse and produces "no click", when there is only a vacuum. In principle, such a system can be extended to resolve two and more excitations by building a tree with beamsplitters, delay lines and linear optics; however, such detection schemes are not robust against detector's imperfections (inefficiency, dark noise) [120]. The recently developed superconducting nanowire detector is capable of distinguishing a number of photons [121, 122]. Yet such a device requires special calibration and only a limited part of the Fock basis is resolvable.

The alternative way is to perform measurement in continuous basis (or the phase space), what corresponds to measurement on a basis spanned on eigenvectors of conjugate position and momenta of the electromagnetic field. This measurement is usually performed with a homodyne detector and allows to characterize the density matrix of the electromagnetic field by reconstructing it from the acquired quadrature's distributions [123].

In this section we describe the basic theory of homodyne detector operation and extend it to the two mode case. The experimental imperfections are presented and quantified. At the end we apply this technique to the detection of TMSV.

4.6.1 Basic theory

The balanced detection is realized via mixing the signal mode $\hat{a}_{\mathrm{sig}}$ with a large amplitude coherent state $|\,\alpha\,\rangle$ ($|\alpha| \gg 1$) on a 50/50 beamsplitter. For generality we assume that these two fields have different central frequencies ω_{LO} and ω_{sig}. Two output channels of the beamsplitter are described by annihilation operators:

$$\hat{c}_1 = \frac{(\hat{a}_{\mathrm{LO}} e^{-i\omega_{\mathrm{LO}} t} + \hat{a}_{\mathrm{sig}} e^{-i\omega_{\mathrm{sig}} t})}{\sqrt{2}}, \qquad \hat{c}_2 = \frac{(\hat{a}_{\mathrm{LO}} e^{-i\omega_{\mathrm{LO}} t} - \hat{a}_{\mathrm{sig}} e^{-i\omega_{\mathrm{sig}} t})}{\sqrt{2}}. \tag{4.13}$$

Each channel of the beamsplitter is sent on the photodetector producing a current proportional to the numbers of photons in the mode with the coefficient of proportionality g:

$$\langle \hat{I}_1 \rangle = g\langle \hat{c}_1^\dagger \hat{c}_1 \rangle = g\frac{\langle (\hat{a}_{\rm LO}^\dagger e^{i\omega_{\rm LO}t} + \hat{a}_{\rm sig}^\dagger e^{i\omega_{\rm sig}t})(\hat{a}_{\rm LO}e^{-i\omega_{\rm LO}t} + \hat{a}_{\rm sig}e^{-i\omega_{\rm sig}t}) \rangle}{2}, \tag{4.14}$$

$$\langle \hat{I}_2 \rangle = g\langle \hat{c}_2^\dagger \hat{c}_2 \rangle = g\frac{\langle (\hat{a}_{\rm LO}^\dagger e^{i\omega_{\rm LO}t} - \hat{a}_{\rm sig}^\dagger e^{i\omega_{\rm sig}t})(\hat{a}_{\rm LO}e^{-i\omega_{\rm LO}t} - \hat{a}_{\rm sig}e^{-i\omega_{\rm sig}t}) \rangle}{2}. \tag{4.15}$$

Assuming the local oscillator to be the large coherent state, we can transfer from operators to classical amplitudes: $\hat{a}_{\rm LO} = |\,\alpha\,|\,e^{-i\phi}$. The currents from the photodetectors are subtracted from each other:

$$\begin{aligned}\langle \hat{i} \rangle = \langle \hat{I}_1 \rangle - \langle \hat{I}_2 \rangle = g\langle \hat{a}_{\rm LO}^\dagger \hat{a}_{\rm sig}e^{-i\delta\omega t} + \hat{a}_{\rm sig}^\dagger \hat{a}_{\rm LO}e^{i\delta\omega t} \rangle = \\ = g\,|\,\alpha\,|\,(\langle\, \hat{a}_{\rm sig}e^{-i(\phi+\delta\omega t)} + \hat{a}_{\rm sig}^\dagger e^{i(\phi+\delta\omega t)}\,\rangle),\end{aligned} \tag{4.16}$$

where the difference between central frequencies of two fields is $\delta\omega = \omega_{\rm sig} - \omega_{\rm LO}$. At the moment $t = 0$ we observe a quadrature $\hat{Q}(\phi)$, at other moments of time Equation (4.16) represents a scanning through all quadratures $\hat{Q}(\phi+\delta\omega\cdot t)$ with a period $1/(\delta\omega)$. If frequencies of two fields are equal, then $\delta\omega = 0$ and the result will be analogous to a measurement at moments $t = \frac{n}{\delta\omega}$, where n is an integer. Such a measurement is called a homodyne detection:

$$\langle \hat{i} \rangle = g\,|\,\alpha\,|\,\langle\, \hat{a}_{\rm sig}e^{-i\phi} + \hat{a}_{\rm sig}^\dagger e^{i\phi}\,\rangle = 2g\,|\,\alpha\,|\,\langle\, \hat{X}_{\rm sig}\cos\phi + \hat{P}_{\rm sig}\sin\phi\,\rangle. \tag{4.17}$$

The measured signal is equal to a quadrature of a field amplified by a LO amplitude $|\,\alpha\,|$. The phase ϕ is defined by the phase of a LO and can be scanned through to obtain different quadratures $\hat{Q}(\phi)$.

4.6.2 Signal-to-noise ratio

Remarkably, an ideal homodyne in contrast to an ideal single photon detector produces an output from every measurement. Thus different states can be distinguished by their statistical distribution for given quadratures. One statistical figure of merit to use is the variance of the output from Equation (4.17). In homodyne detection the vacuum input creates nonzero variance of the output current, and it is natural to compare the signal variance to it. Hence the signal-to-noise ratio is defined as a ratio between the mean square signal current and the mean square noise current fluctuations [52]. In order to find the variance of the noise we average our observable $\hat{i}$ over the vacuum state in a Fock basis $|\,0\,\rangle$:

$$\mathcal{N}_{\mathrm{s}} = \langle\, \hat{i}^2 \,\rangle_{\mathrm{vac}} - \langle\, \hat{i} \,\rangle^2_{\mathrm{vac}} = g^2\, |\,\alpha\,|^2 = g^2 \bar{n}_{\mathrm{LO}}, \tag{4.18}$$

where $\bar{n}_{\mathrm{LO}}$ is an averaged number of photons in a local oscillator. This noise is called a shot noise and it can be interpreted as an uncertainty in number of photons of a strong pump, which follows a Poisson distribution. Fluctuations in a signal, in case the state of interest is a Fock state with a number of photons n_{sig}, is given by:

$$\mathcal{S} = \langle\, n \,|\, \Delta\hat{i}^2 \,|\, n \,\rangle = g^2\, |\,\alpha\,|^2\, (1 + 2n_{\mathrm{sig}}). \tag{4.19}$$

As a result the signal-to-noise ratio is:

$$\frac{\mathcal{S}}{\mathcal{N}_{\mathrm{s}} + \mathcal{N}_{\mathrm{e}}} \approx \frac{\mathcal{S}}{\mathcal{N}_{\mathrm{s}}} = 1 + 2n_{\mathrm{sig}}, \tag{4.20}$$

where we have neglected other noises compared to the shot noise $\mathcal{N}_{\mathrm{e}} \ll \mathcal{N}_{\mathrm{s}}$. We can deduce two important statements from this formula. An assumption that we can infinitely increase our quantum signal by increasing LO power falls apart, because together with a signal we increase noise proportionally. The second conclusion is on a practical side: we need to increase the LO power until this inequality $\mathcal{N}_{\mathrm{e}} \ll \mathcal{N}_{\mathrm{s}}$ is valid, this will maximize the signal-

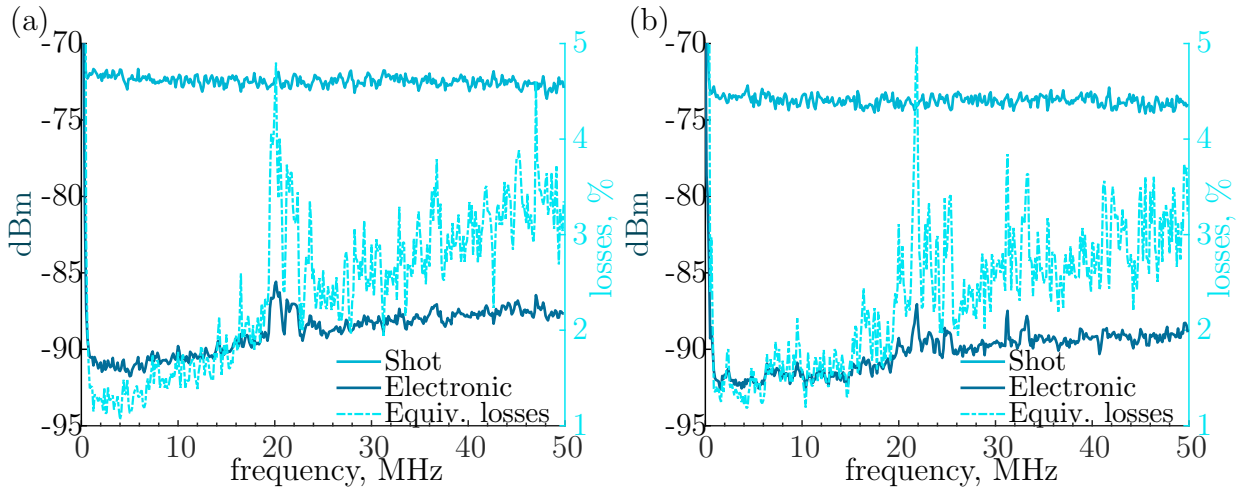

Figure (4.15) Noise spectrum of two homodyne detectors used in the experiment. Only electronic noise - dark blue line, in the presence of 10 mW of LO - blue line. Right axes represent equivalent losses η_e

to-noise ratio.

Besides this fundamental limitation on a signal-to-noise ratio, there are experimental imperfections such as photodiode detection efficiency, spatial and temporal mismatch between the modes, electronic noise of the detector. Such inefficiencies can be taken be into account akin to effective loss for optical signal [124], which effect is well described by the beam-splitter model (2.26). For photodetector inefficiency and spatial mismatch the effective transmission coefficients are straightforward and correspondingly photodetector efficiency and mode matching factor, what is usually expressed as maximal achievable interference visibility for given modes. In turn, the finite ratio between electronic and shot noises of a detector accounted as an effective transmission with analogous losses coefficient $\eta_e = \frac{10^{0.1x}-1}{10^{0.1x}}$, where x is the ratio between shot noise and electronic noise in dB [125]. Summarizing all of the above, signal-to-noise ratio for a weak coherent input state is:

$$\frac{\mathcal{S}}{\mathcal{N}} = \frac{\eta_d \cdot \eta_{vis} \cdot \eta_e \cdot P_{sig}}{h\nu \cdot \delta\nu}. \tag{4.21}$$

There are a few crucial points which follow from the formula and should be kept in mind while working with a homodyne detection in a quantum regime. First and obviously, mode-

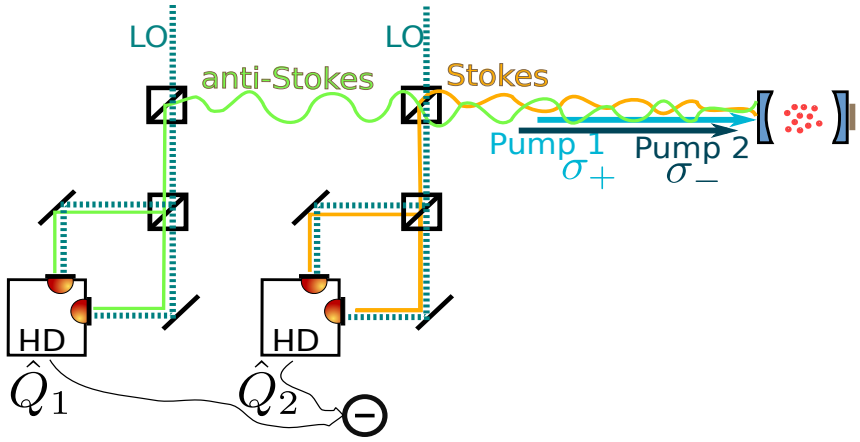

Figure (4.16) Two pumps with orthogonal polarizations enter the cavity through the input mirror. Atomic cloud emits two photonic modes, again with opposite polarizations: Stokes and anti-Stokes. The entangled modes are measured with two separate homodyne detectors. The resultant quadratures are digitized and processed.

matching between LO and signal path is important and should be kept as high as possible. In practice it means that visibility should be larger than 95%. Secondly, quantum efficiency of a photodetector needs to be on the same scale, thus more than 90% corresponds to the photodiode's responsivity > 0.59 A/W at the central wavelength 795 nm.

In our experiment we use two homodyne detectors, which are based on [126]. Each detector basically consists of a pair of *Hamamatsu S5972* photodiodes and transimpedance amplifier *OPA 847*. The fast response time of the diodes and large bandwidth of *OPA 847* allows to achieve -3 dB bandwidth of 100 MHz with 4 $k\Omega$ transimpedance gain. The 50 MHz band of shot noise in comparison with electronic noise are presented in the Figure 4.15 for both detectors. Therefore to attain 98% of an effective transmission in 20 MHz band people use at least 10 mW of LO [101].

4.7 Acquisition

4.7.1 Optical detection path

Our collinear regime of FWM generation has its own complications and advantages. We send two pumps collinear to the cavity mode, and they are detuned from the cavity resonance by 60 MHz. Pumping fields will form a standing wave inside, moreover reflecting back and forth for 100 times they induce both forward and backward FWM (for the phase-matching conditions please see Subsection 5.1.2). Furthemore, the pump fields are strong coherent and they unavoidably are reflected toward the detectors. On one hand, the homodyne/heterodyne detection is a frequency resolved measurement. On the other hand, the beating signal between LO and the pump acting on the same transition has frequency $\delta = 60$ MHz and falls in a bandwidth of a detector. It is strongly amplified and lifts the shot noise level at all operational frequencies. We are minimizing this effect by splitting photons and pumps from the same transition to different detectors via polarization, in particular, anti-Stokes is right-circularly polarized, pump 2 is left-circularly polarized. Similarly, anti-Stokes and Stokes photons are split on a PBS via polarization to follow into different detection arms. They are then mode-matched with a resonant strong coherent beam (LO) and sent to the corresponding detector (Fig. 4.16). The mode matching is performed with a coherent light instead of a photonic mode and is repeated at least every day. The balanced detector measures a quadrature $\hat{Q}(\theta)$, where we can scan the phase difference θ between LO and the quantum mode with a mirror controlled with a piezo actuator.

4.7.2 Data acquisition

While we minimized the back reflection of pumps into detectors, non-ideal polarizational optics will let a noticeable amount to pass. We put a low pass filter to cut the remaining part of the "leakage" electronically. A seemingly easy task had its pitfall: an output impedance of the detector is not fixed, thus, the length of the cable, RF filters, and input impedance of

a digitizer could change feedback loop characteristics. We use the sequence of 200 MHz $\rightarrow$ 100 MHz $\rightarrow$ 50 MHz and 20 MHz LPF, which does minimize the back reflection and keeps the signal undisturbed.

The electrical signal after filtering is sent to either high-speed digitizer *Acqiris* or oscilloscope *Agilent infiniuum*, which are triggered by our pulse sequencer from Section 4.5. The programmable PCI card allows us to see data being processed in real-time. Although, an 8-bit digitizer with a minimum range of 50 mV distorts a few millivolt signal, due to lack of resolution. The final data is collected with an oscilloscope *Agilent infiniuum* (1 GHz highest frequency and 4 GSa/s sampling rate) and processed afterwards.

4.8 Conclusion

In this chapter I have described the experimental tools I have built with my colleagues—all except OPLL and homodyne—during my PhD program. Designing and constructing the experiment from the very beginning enabled me to highlight the limitations of techniques and mention unobvious pitfalls.

In summary, ^{87}Rb atoms are cooled in a MOT. The atomic cloud is overlapped with a cavity mode, which enhances the interaction and sets the preferable direction of the emission of quantum fields. The cavity made has low finesse and its central frequency is locked to an auxiliary laser. The dynamically controlled pumps are sent into an atomic cloud to induce the FWM process. The emitted quantum fields are sent into two separate homodyne detectors that measure their quadratures.

Chapter 5

Two-mode squeezing generated via four-wave mixing in cold atoms

The system built in the previous chapter is a platform for many quantum optical experiments: single photon source [39], quantum memories [127], EIT and stationary light [128], EPR paradox [45], and quantum state engineering [129], to name a few. In this chapter we are discussing and demonstrating its operation as a source of the two-mode squeezing. The first two sections are designated to characterize our system. Section 5.1 is devoted to summarizing the detrimental effects, which affect the squeezing level and even more generally the storage of the quantum state. In Section 5.2 we measure the strength of atom-light coupling enhanced by the cavity. In Section 5.3 we demonstrate the OPO regime of the operation near and above-threshold. Finally, in Subsection 5.3.2 we measure the amount of two-mode squeezing.

5.1 Detrimental effects

Any physical system is far from the ideal model. When some effects are a few orders of magnitude smaller than the measured signal, then they are indeed considered negligible. Other processes generate noises of the same order of magnitude as the signal, thus signif-

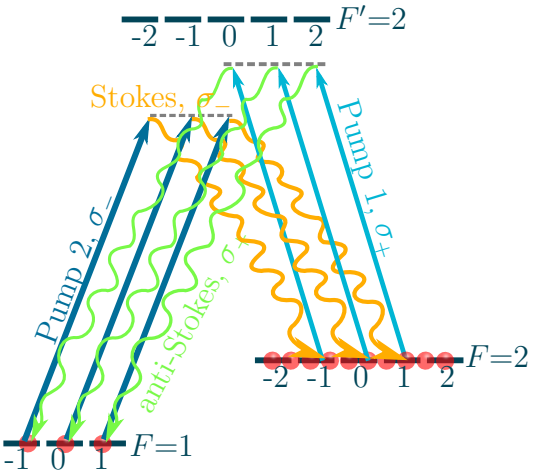

Figure (5.1) Four-wave mixing in a non-polarized atomic ensemble. The pumps and emitted photons with the specified polarizations form three independent Λ schemes.

icantly distorting the result. In this section we make an estimation of how imperfections affect the experiment on two-mode squeezing. Among them are non-ideal Λ scheme, possible phase-matching configurations, phase noise, and detection inefficiencies. One more effect which is inherent to our experiment, specifically, and comes from the geometry of the layout, is the standing wave formed by pumps (Subsection 5.1.3).

5.1.1 Loss of atoms

We have neglected until this time to consider that our Λ system has an internal structure. In reality, the hyperfine metastable levels are degenerate in magnetic quantum number (Fig. 5.1), and we are going to resolve the splitting only when we have above 8 Gauss of an external magnetic field[1]. In Subsection 4.7.1 we reasoned the polarization choice for two pumps and photonic modes to effectively separate both signals to opposite channels and to minimize the leakage. By setting the cavity axis to be our quantization axis and choosing the first pump's polarization arbitrarily to be σ_+, we arrive at all other polarizations to be determined: σ_- for the Pump 2, σ_+ for the anti-Stokes photon, and σ_- for the Stokes.

Above, in Figure 5.1 the paths returning the atom back to its initial sublevel are included.

[1]The hyperfine Landé g_F factor is 0.7MHz/G for ^{87}Rb [67]. As an example, the Earth's magnetic field is 0.25–0.65 G, and it induces 0.1–0.5 MHz level splitting.

A simple consideration would demonstrate that only atoms returning back to their initial Zeeman sublevel experience a collective enhancement. For the sake of simplicity, we consider a single excitation to be involved in the DLCZ process. After the first pump acted and a spontaneously emitted anti-Stokes photon was detected, the atomic wavefunction is

$$|\,\Psi\,\rangle = \frac{1}{\sqrt{N}} \sum_{j=1}^{N} e^{i(\boldsymbol{k}_{c1}-\boldsymbol{k}_1)\boldsymbol{r}_j}\,|\,2\ldots 1_j \ldots 2\,\rangle\,. \tag{5.1}$$

The second strong pump excites the atom to level $|\,3\,\rangle$ ($|\,F'=2\,\rangle$):

$$|\,\Psi_{\text{initial}}\,\rangle = \frac{1}{\sqrt{N}} \sum_{j=1}^{N} e^{i(\boldsymbol{k}_{c1}+\boldsymbol{k}_{c2}-\boldsymbol{k}_1)\boldsymbol{r}_j}\,|\,2\ldots 3_j \ldots 2\,\rangle\,. \tag{5.2}$$

Now we would like to compare the strength of two transitions: the atom returns to the same sublevel (P_{same}) or different (P_{diff}) by emitting the Stokes photon. We apply the Fermi's golden rule for both cases:

$$\begin{aligned} P_{\text{same}} &\propto |\langle\,\Psi_{\text{final}}\,|\sum_{j=1}^{N} \hat{d}_j^{32}\hat{a}_2^{\dagger} e^{-i\boldsymbol{k}_2\boldsymbol{r}_j}\,|\,\Psi_{\text{initial}}\,\rangle|^2 = \\ &= \left|\frac{1}{\sqrt{N}}\sum_{j,k}\langle\,2\ldots 2\ldots 2\,|\,e^{i(\boldsymbol{k}_{c1}+\boldsymbol{k}_{c2}-\boldsymbol{k}_1)\boldsymbol{r}_k} e^{-i\boldsymbol{k}_2\boldsymbol{r}_j}\,|\,2_j\,\rangle\,\langle\,3_j\,|\cdot|\,2\ldots 3_k\ldots 2\,\rangle\right|^2 = N, \end{aligned} \tag{5.3}$$

where we consider perfect phase matching, and notations are the same as in Section 2.4. If we consider the initial level to differ from the final state $\frac{1}{\sqrt{N}}\sum_k |\,2\ldots X_k\ldots 2\,\rangle$, then:

$$P_{\text{diff}} \propto \left|\frac{1}{N}\sum_{i,j,k}\langle\,2\ldots X_k\ldots 2\,|\,e^{i(\boldsymbol{k}_{c1}+\boldsymbol{k}_{c2}-\boldsymbol{k}_1)\boldsymbol{r}_i} e^{-i\boldsymbol{k}_2\boldsymbol{r}_j}\,|\,X_j\,\rangle\,\langle\,3_j\,|\cdot|\,2\ldots 3_i\ldots 2\,\rangle\right|^2 = 1. \tag{5.4}$$

In summary, the collective enhancement is proportional to the number of atoms and manifests itself when the atom returns to the initial sublevel. This result means that the second process is incoherent and will not result in generation of the correlated photonic pairs. In Figure 5.2 we can trace different ways the atom can follow and with only

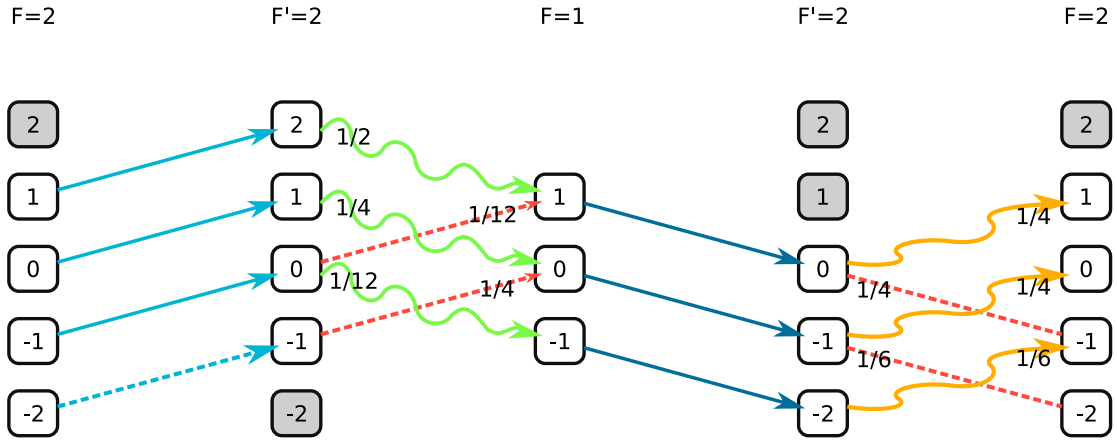

Figure (5.2) All atoms are initially pumped on $|\,F=2\,\rangle$, from where they are transferred to an excited level $|\,F'=2\,\rangle$ by the right circular polarized pump 1 (light blue arrows). The light blue arrow demonstrates the pumping process which takes place, although does not result in detectable correlated photons. The spontaneous emission $F'=2 \rightarrow F=2$ has two parts: detectable and 'good' photons (green wavy line) and undetectable red dahed arrows. Dark blue arrows indicate the second pump. The second spontaneous emission process again has detectable (orange) photons and inevitable (red-dashed) lost photons.

five coherently enhanced paths. Among the five paths there are three trajectories which are detected. They are shown in Figure 5.1. Together with them there are two paths $|\,F=2, m_F=-2\,\rangle \rightarrow |\,F=1, m_F=0\,\rangle \rightarrow |\,F=2, m_F=-2\,\rangle$ and $|\,F=2, m_F=-2\,\rangle \rightarrow |\,F=1, m_F=0\,\rangle \rightarrow |\,F=2, m_F=-2\,\rangle$, which are coherent and enhanced, although they are undetectable. Red dashed photons on the diagram have opposite polarizations compared to 'good' green and orange photons. Please note, that we have omitted spontaneously emitted π-polarized photons from the picture. Their emission is suppressed by the phase-matching condition and they are undetectable in our experiment, as they escape the cavity mode.

From the description above we conclude that the main detrimental effect due to Zeeman sublevels is a decrease of an optical depth. The generation of the noise photons into the measurable mode is suppressed. Additionally, the probabilities of the spontaneous emissions $|\,F'=2, m_{F'}\,\rangle \rightarrow |\,F=1, m_F\,\rangle$ are not evenly distributed, and are proportional to the hyperfine dipole matrix elements. The values are multiples of $\langle\, J=1/2\,||\,er\,||\,J'=1/2\,\rangle$ [67], and the squares of the multiplication factors are depicted in Figure 5.2.

5.1.2 Phase matching

We have mentioned that in our experiment two phase-matching conditions coexist. In this subsection we compare three mode-matching conditions (Fig. 5.3): collinear backward and forward, and at 90 degrees [39]. The phase-matching condition is fulfilled if this sum of the vectors $\Delta\boldsymbol{k} = \boldsymbol{k}_{c1} + \boldsymbol{k}_{c2} - \boldsymbol{k}_1 - \boldsymbol{k}_2$ is equal to zero[2]. The perfect phase-matching is attributed to the forward collinear regime $\Delta\boldsymbol{k}_F = 0$ in the case of two-photon resonances. The other two sums of wavevectors are easily found:

$$\Delta\boldsymbol{k}_B = 2\delta/c, \quad \Delta\boldsymbol{k}_{90} = \frac{\sqrt{2}}{c}\sqrt{\Delta_{HFS}^2 + \delta^2} \tag{5.5}$$

In order to find the phase factor from Subsection 2.4.4, which is directly related to strength

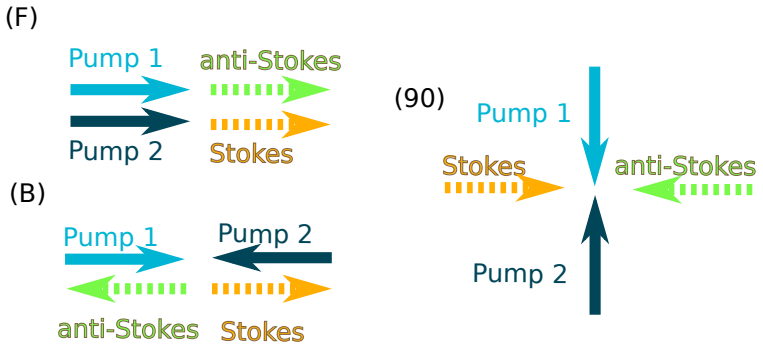

Figure (5.3) Three different phase-matching configurations

of the FWM process, we change the summation over each atom to an integration over an ensemble. Using homogeneity in the transverse plane and even density distribution $\rho(\boldsymbol{r})$, we keep integration only along the cavity mode over the length of an atomic ensemble L:

$$\phi = \sum_j e^{i(\boldsymbol{k}_{c1}+\boldsymbol{k}_{c2}-\boldsymbol{k}_1-\boldsymbol{k}_2)\boldsymbol{r}_j} \to \int \rho(\boldsymbol{r}) e^{i\Delta\boldsymbol{k}\cdot\boldsymbol{r}} d^3\boldsymbol{r} \approx \frac{N}{L}\int_{-L/2}^{L/2} e^{i\Delta k\cdot z\sin\theta} dz. \tag{5.6}$$

[2] As a reminder the modulus of the wavevectors $k_{c1} = \frac{\omega_{23}-\Delta_2}{c}$, $k_{c2} = \frac{\omega_{13}-\Delta_1}{c}$, $k_1 = \frac{\omega_{13}-\Delta_2}{c}$, and $k_2 = \frac{\omega_{23}-\Delta_1}{c}$.

The phase factor is equal to number of atoms for the forward collinear regime ($\phi_{\mathrm{F}} = N$). The phase matching is close to perfect for both the backward collinear and 90 degrees regime:

$$\phi_{\mathrm{B}} = N\mathrm{sinc}(\Delta k_{\mathrm{B}} L/2) \approx N, \qquad \phi_{90} = 0.9 \cdot N. \tag{5.7}$$

From this point of view, the efficiency is the same. This would not be the case if we make a delay between two pumps, as it was analyzed in the work by Zhao et al. [71]. Here we follow their line of derivation. If we consider the storage we need to analyze what happens to the spin-wave (SW) embedded on an atomic ensemble after the first (anti-Stokes) photon is detected. All N atoms carry the phase of the SW, and the residual atomic movement leads to its dephasing. In [71] the time of dephasing is defined as the time an atom needs to pass $1/2\pi$ of the SW wavelength. We find SW wavelength as $\lambda_{\mathrm{SW}} = \frac{2\pi}{|\,\boldsymbol{k}_{\mathrm{c}1} - \boldsymbol{k}_1\,|}$ for three schemes: $\lambda_{\mathrm{F}}^{\mathrm{SW}} = 4.4$ cm, $\lambda_{\mathrm{B}}^{\mathrm{SW}} = 398$ nm, and $\lambda_{90}^{\mathrm{SW}} = 562$ nm. The lifetime of a coherence $\tau = \frac{\lambda^{\mathrm{SW}}}{2\pi v}$ could be rewritten as a generalized function of angle and temperature:

$$\tau(\theta, T) = \frac{1}{v\,|\,\Delta\boldsymbol{k}\,|} = \sqrt{\frac{m}{k_{\mathrm{B}} T (k_{\mathrm{c}1}^2 + k_1^2 - 2k_{\mathrm{c}1}k_1\cos(\theta))}}. \tag{5.8}$$

Figure 5.4 represents a lifetime of an SW in a cold atomic ensemble for temperatures from the sub-Doppler to Doppler limit. The function strongly depends on an angle: for zero degree lifetime is hundreds of milliseconds, whereas already for two degrees it drops below hundreds of microseconds. Please note that all the fields propagate perpendicularly to an acceleration of a free fall, so gravity will not additionally reduce the lifetime of an SW. The counter-example is the work by Bimbard et al. [39], where the cavity is along the accleration of a free fall and the velocity must be increased by $g_0 t$.

5.1.3 Standing wave

So far we did not take into account that our Fabry-Perot cavity makes the electric field inside to form a standing wave pattern (Subsection 4.4.1). There is a distinct effect from the

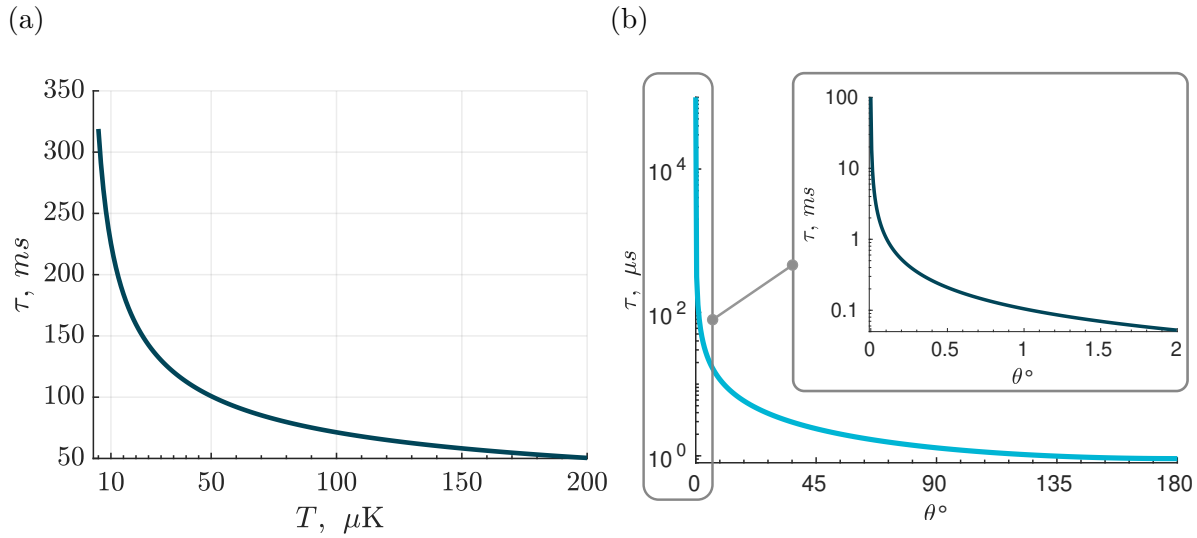

Figure (5.4) The dependence of a SW lifetime on a temperature (a) and on an angle (b). (a) The plot is built for a collinear scheme, $\theta = 0$. (b) The temperature of atoms is 50 μK. The inset shows a smaller range of angles, which could be used as a semi-collinear scheme in order to separate the pumps from signals.

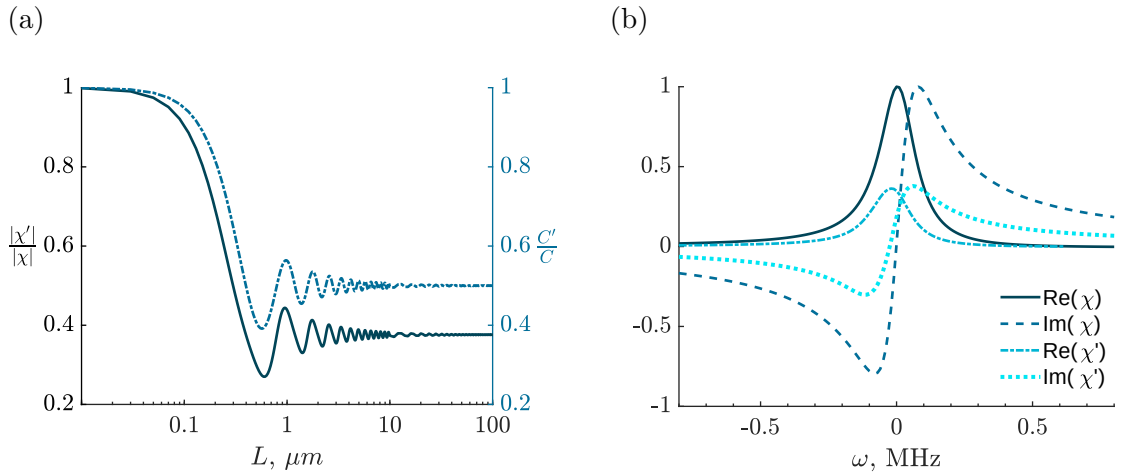

Figure (5.5) (a) The ratio of the effective nonlinear coefficient and cooperativity in a presence of a standing wave to their analogs in a running wave case as a function of the sample size. (b) Spectrum of the nonlinearity coefficients χ and χ'. For the reference here we list the parameters used to produce these graphs: $\delta_1 = -\delta_2 = 60$, Ω_1=$2\pi\cdot$ 1.64, Ω_2=$2\pi \cdot 4.66$, $\gamma_{12} = 2\pi \cdot 0.1$, $\gamma_{23} = \gamma_{13} = 2\pi \cdot 6$, $\Delta_2 = 2\pi \cdot 20$, $\Delta_2 = 2\pi \cdot 80$. All parameters are in MHz.

collinear configuration on the generated fields: besides the modulated signal modes, both pumps have a standing wave pattern, which is uncommon. The effect of the standing waves for both pump and signal modes manifests itself as modulation of the pump's Rabi frequency and the cavity coupling constant respectively:

$$\Omega_{1,2} \approx \pm \mid \Omega_{1,2} \mid \cos\left(k_{1,2}\, x\right) \quad \text{and} \quad g_{1,2} = \pm \mid g_{1,2} \mid \cos\left(k_{1,2}\, x\right), \tag{5.9}$$

where x is a coordinate along the cavity mode. The plus or minus sign in the formula originates from the frequency difference between two fields being equal to twice the FSR: $\Delta_{\text{HFS}} + \delta = 2\text{FSR}$. This results in the phase difference between pumps/signals acting on different transitions to be π (Subsection 4.4.2). The pumps are detuned from the cavity resonance by 60 MHz, although they will still enter the cavity and form a standing wave with $k_1 \approx k_{\text{c1}}$ and $k_2 \approx k_{\text{c2}}$ and smaller amplitude.

As a result we can estimate the change of the effective nonlinearity, cooperativity, and their spectra, if we take into account that modulation occurs with wavevector $k = \frac{2\pi}{\lambda}$ and wavelength $\lambda \sim 795$ nm. The nonlinear coefficient considered in a case of phase matching takes the form:

$$\chi'(\omega) = \frac{N}{L} \int_{-L/2}^{L/2} \frac{\mid g_1 \mid \mid g_2 \mid \mid \Omega_1 \mid \mid \Omega_2 \mid \cos^2(k_1 x) \cos^2(k_2 x)}{\tilde{\delta}_2(\omega)\Delta_1(\omega)\left(i(\delta-\omega) + \gamma_{12}/2 + \frac{\Omega_2^2 \cos^2 k_2 x}{-i(\Delta_2+\omega)+\gamma_{23}/2}\right)} dx. \tag{5.10}$$

Having this we can compare the new nonlinear coefficient to the one obtained without a standing wave:

$$\frac{\chi'(\omega)}{\chi(\omega)} = \frac{\tilde{\Delta}(\omega)\tilde{\delta}_1(\omega)}{L} \int_{-L/2}^{L/2} \frac{\cos^2(k_1 x)\cos^2(k_2 x)\left(i(\delta-\omega) + \gamma_{12}/2 + \frac{\Omega_2^2 \cos^2 k_2 x}{-i(\Delta_2+\omega)+\gamma_{23}/2}\right)^{-1}}{\left(i(\Delta_1-\omega) + \gamma_{13}/2 + \frac{\Omega_1^2 \cos^2 kx}{i(\delta-\omega)+\gamma_{12}/2+\frac{\Omega_2^2 \cos^2 kx}{-i(\Delta_2+\omega)+\gamma_{23}/2}}\right)} dx. \tag{5.11}$$

The same effect takes place for cooperativities (Eq. 2.87). In a similar manner it is quantified

and presented in Figure 5.5. As we can see in Figure 5.5(a), the standing wave decreases the cooperativity by about a half, while the effective nonlinearity drops to about a third of the initial value for a sample size larger than few resonant wavelengths. The spectral properties of the gain are not affected as we can see in Figure 5.5(b). As a result we may state that standing wave effect manifests itself as a reduction in both cooperativity and nonlinearity and can be compensated by use of a larger or a denser atomic ensemble.

5.1.4 Phase noise

In this subsection we consider the effect of the phase noise on two mode squeezing generation. As it was shown in Section 2.1, the phase difference between the pumps ϕ determines squeezing correlations between the quadratures. Furthermore from Equation (2.22) it follows that the quadrature variance depends on the squeezing phase ϕ and the phases of LOs: θ_1 and θ_2. Thus the phase noise affecting the final result comes from two sources: one, the phase noise between the two pumps inducing the FWM; two, the noise between the LO and the signal in the homodyne detection. In our experiment the two pumps (and LOs) are derived from two different phase-locked lasers, thus we would need to estimate how much it will affect the level of squeezing. If we assume that during the time between generation and detection the phase experiences normally distributed random fluctuations $\frac{e^{-\frac{(\phi)^2}{2\delta\phi^2}}}{\sqrt{2\pi}\delta\phi}$ with zero mean and variance $\delta\phi$, the maximal observed squeezing would be

$$\langle\, \delta Q^2 \,\rangle = \frac{1}{2}\left(\frac{1 + r^2 - 2re^{-\delta\phi^2/2}}{1 - r^2}\right). \tag{5.12}$$

Thus to quantify the effect we need to estimate the phase deviation on a time scale corresponding to the delay between squeezing generation and detection. Taking into account the noise spectrum presented earlier in Figure 4.5, we may estimate the phase variation as [130]

$$\delta\phi^2(\tau) = \int S(f)\mathrm{sinc}^2\left(\pi\tau f\right) df, \tag{5.13}$$

where $S(f)$ is the noise power spectral density, and τ is the time interval. The result of integration gives the square of relative phase variation to be $\delta\phi^2 \approx 0.02$ rad^2 for injection locking (and 0.07 rad^2 for OPLL) on a 100 ns time scale. The correlation decreases by a factor $e^{-\delta\phi^2/2} \approx 0.99$ (0.966), which corresponds to an effective "transmission coefficient" of 99.5% (98%). If the effective path lengths for the pumps and signals are matched with the paths that the LO travels, then the time interval of hundreds of ns is a good estimate. The correlation stays high, unless we are interested in a storage of quantum state, then on a 10 μs time scale the variation increases to $\delta\phi^2 \approx 0.28$ rad^2 (1.17 rad^2) and an effective transmission coefficient is 93% (75%).

There are other approaches than an active phase stabilization, one of them is to derive all beams from the same laser. For even better relative-phase stability between LO and generated fields, LO could be generated inside the same media as the TMSV [15]. The authors of [15] split the pump into two spatially separated parts. While the TMSV is created in one part of the cell with only pumps being present; in the second part a bit of seeding is added leading to a bright twin beam generation. The strong beams generated in the FWM process serve as LO for the homodyne detection.

5.1.5 Detection inefficiencies

Losses in the system will disproportionally affect squeezing and antisqueezing levels as it was shown in Subsection 2.1.6. Three main sources of losses are detection efficiency, optical losses and phase stability. Homodyne detector efficiency includes quantum efficiencies of the photodetectors of 91%, the finite ratio between electronic and shot noises results in an effective transmission of 99% (Subsection 4.6.2), and mode-matching between local oscillator and signal paths is set by the visibility of interference (is 94%)[3]. The pure optical losses for each signal path in our experiment are of around 20%. Recalling that the phase stability

[3]During the data acquisition all the losses were the same, except for the visibility. The mode matching between the LO and signal modes could have dropped to 85% due to thermal fluctuations, resulting in an uncertainty of the overall losses of 5%.

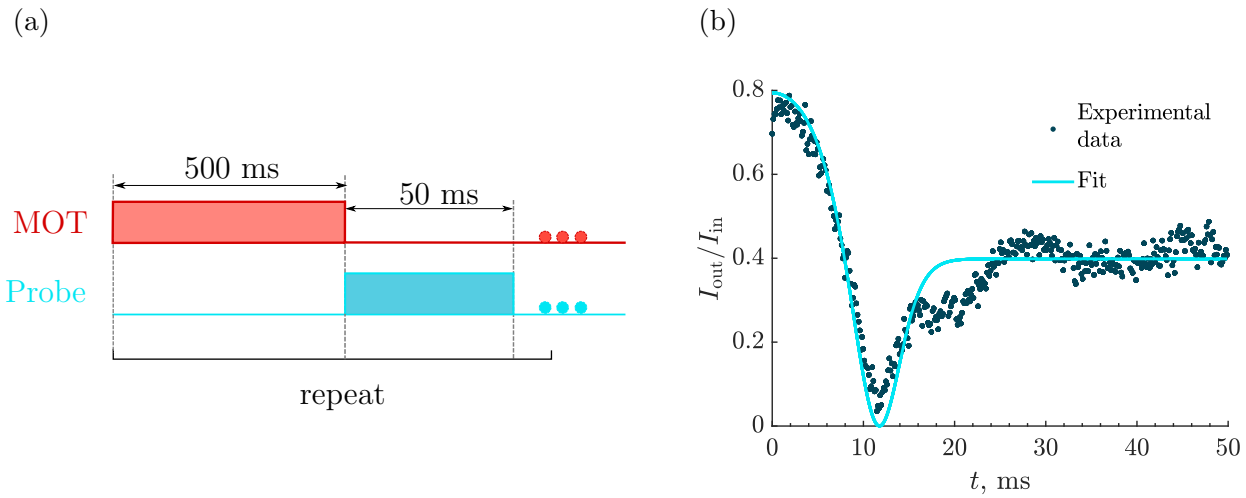

Figure (5.6) (a) The pulse sequence used for the cooperativity measurement. (b) Reflected weak coherent light with a homodyne detector. At initial moment of time t=0 we let the cloud expand.

from the above is 99.5%. Overall it gives us $\eta_A = \eta_S = 35\%$ of effective losses for each channel. The measurable squeezing level with such losses could not exceed a 5 dB level.

5.2 Atom-light interaction measurement

We realized pulsed scheme which gives us access to another way of measurement of the background pressure and the temperature of a cold atomic cloud. As a first step we prepare the atomic ensemble and switch off the MOT, see Figure 5.6(a). While the atomic cloud expands we probe it with minuscule power resonant to a transition we want to characterize, so it will not induce any significant frequency shift or saturate the atoms. We monitor reflected intensity of the probe field, as shown in Figure 5.6(b). In the first 10 ms we see how the level drops at first as the atoms start to expand and leave the cavity mode. The minimum reflection corresponds to the impedance matching described in Subsection 4.4.1. After that the reflection increases to the level corresponding to the bare cavity. A simple model—Equation (2.63)—fits the experimental data in Figure 5.6(b). From the fit we find cooperativity to be 10.

A closely related measurement is based on the frequency shift of the cavity resonance

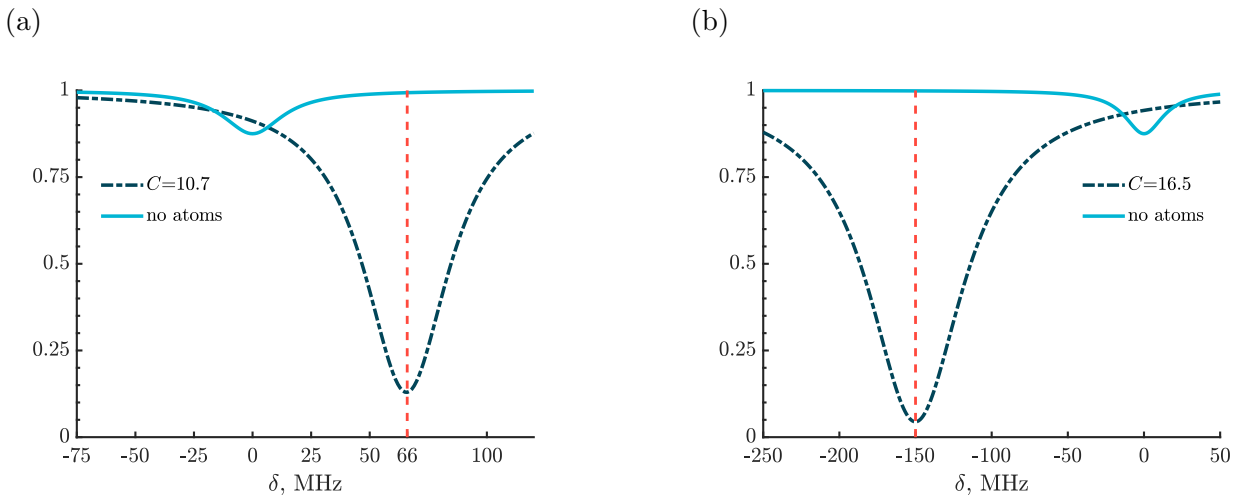

Figure (5.7) Cavity resonance frequency shifts in the presence of atoms. (a) The probe is red detuned from the atomic resonance by $\Delta = -30$ MHz (b) Blue detuning $\Delta = 20$ MHz

due to atoms. We once again send the weak probe with a fixed non-zero detuning from the atomic resonance, and monitor the frequency shift as demonstrated in Figure 5.7. We can see a shot-to-shot discrepancy in the values, although the range of the cooperativity parameter is limited by 10 to 20 depending on the alignment of the cooling beams.

Everyday before running the experiment we make sure that cooperativity is above 10. We do optimization by consequentially aligning cooling laser beams and magnetic coils position in three dimensions. While we run the experiment we monitor the atomic cloud position and brightness on a camera to keep cooperativity high.

5.3 Four-wave mixing

In this section and below we present the results on quasi-continuous non-degenerate FWM. First laser cooled atoms are prepared for 500 ms (Fig. 5.8), after that the gradient magnetic coils are switched off to eliminate spatial Zeeman broadening. During the first 500 ms besides preparation of the cloud, we send the cavity lock laser, and we keep it off during the FWM process.

The pumps with counter-rotating $\sigma_{\pm}$ polarization are derived from Ti:Sapphire laser and

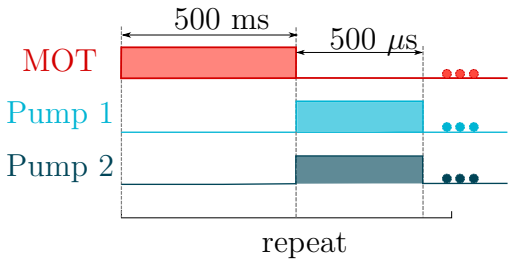

Figure (5.8) Time sequence for quasi-continuous non-degenerate FWM

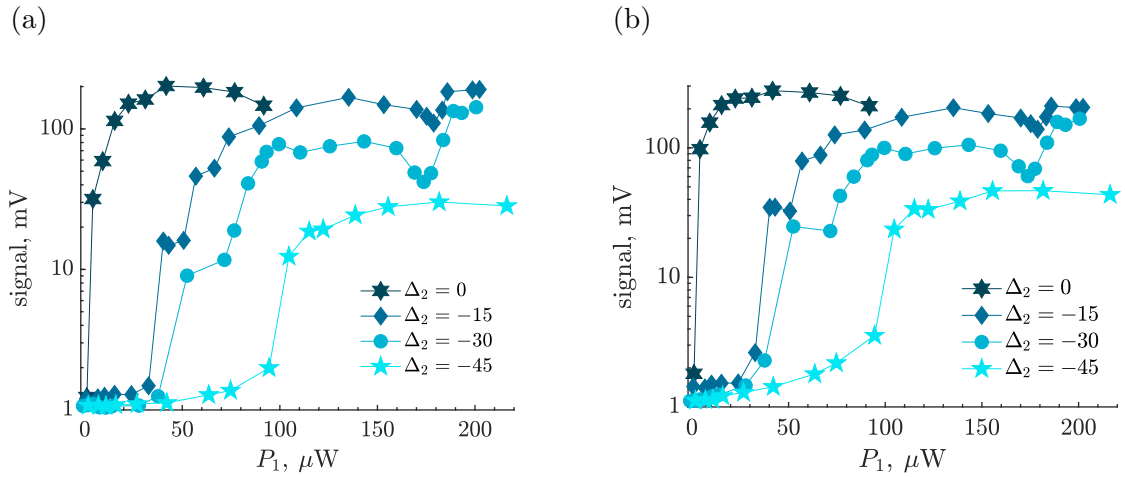

Figure (5.9) We keep the power of the second pump constant $P_2 = 50\,\mu$W, detuning Δ_2 from the excited level is scanned through a few values written in the legend. (a) Signal in the first channel in mV (b) Signal in the second channel in mV.

the injection locked ECDL respectively by modulation through the independent acousto-optical modulators. The pump with σ_+ polarization acts on $\left|\,5S_{1/2}, F = 2\,\right\rangle \rightarrow \left|\,5P_{1/2}, F = 2\,\right\rangle$ being red detuned by a variable value Δ_2, while the second pump with σ_- polarization acts on $\left|\,5S_{1/2}, F = 1\,\right\rangle \rightarrow \left|\,5P_{1/2}, F = 2\,\right\rangle$ transition being red detuned by $\Delta_2 = \Delta_2 + 60$ MHz, as it is depicted in Figure 5.1.

The pumps are launched into the same cavity spatial mode. The four-wave mixing exposure happens for 500 μs. During this time the generated photons are measured on corresponding homodyne detectors, where the LO's frequencies are derived from the unmodulated lasers, which are used for pumps. Each local oscillator is mode matched with a pump and has a power of 10 mW.

5.3.1 Threshold characterization

One of the OPO characteristics is a threshold of stimulated emission. When the gain of an amplifier is large enough, the spontaneously emitted photons seed the amplifier and provide positive feedback. The subsequent radiation becomes coherent and saturates the gain of the OPO. In principle, coherent generation can be achieved in a free space [73], when the gain is large enough that a single emitted photon still has a significant chance to be amplified to macroscopic numbers of photons. The method exploited here is the use of a cavity, which increases the effective lifetime of the emitted photon and hence the chances for amplification of the successful seeding to a macroscopic value. In contrast to a free space, where the threshold happens only in the backward configuration (Fig. 5.3), coherent generation can happen in both travelling wave and standing wave in the cavity. According to the model (Subsection 2.4.7) threshold occurs when the denominator is equal to zero.

To observe the threshold, we monitor the averaged variance measured by both homodyne detectors, while changing the power of one pump for a number of detunings and for the fixed second pump power. The averaged homodyne outputs normalized to the vacuum's value are presented in Figure 5.9. As it is expected, the output is symmetrical for both channels and increases by two orders of magnitude at the saturation. Saturation represents the lack of the second pump's strength to provide conversion of the Stokes photon into the anti-Stokes. Each curve represents different detunings of the pumps from the excited level. As the detuning becomes large the gain decreases as $\sim \frac{1}{(\Delta_1-\Delta_2)\Delta_1\Delta_2}$. Despite getting lower gain, the losses due to spontaneous emission also decrease $\sim \frac{1}{\Delta_1}$. As a result, for a relatively small detuning the decrease in gain is compensated by a reduction in losses and the maximum output value is the same, while for a larger detuning the gain reduction cannot be compensated further.

The chart of the above-threshold generation as a dependence on both pump powers and detuning Δ_2 is presented in Figure 5.10. Here we see, that effective parametric gain is proportional to the cooperativity and the pumps amplitudes, therefore there is linear dependence on the pumps power ratio. In theory, the losses are proportional to the real part

(a) Simplified theory

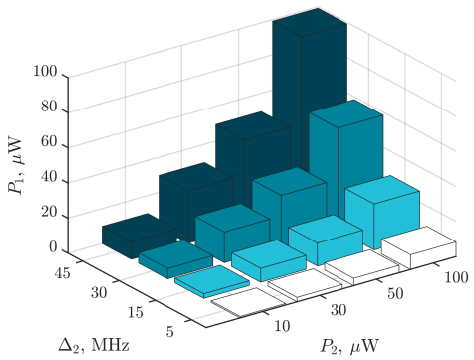

(b) General theory

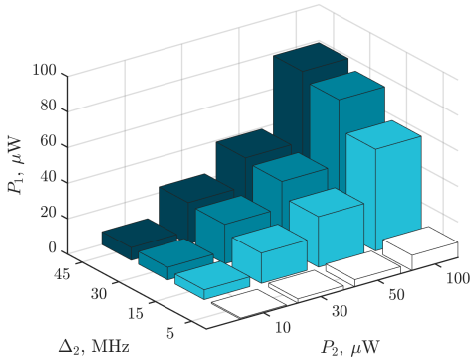

(c) Experimental data

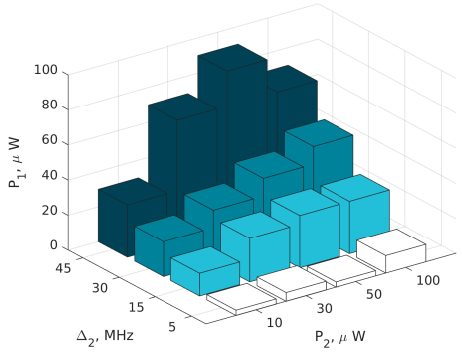

Figure (5.10) The chart gives a map of the threshold generation. (a) Simplified theory given by formula (2.106) with parameters $C = 10$ and $\gamma_{13} = \gamma_{23} = 2\pi \cdot 6$ MHz. (b) General theory given by equation (2.104) with parameters $C = 13$, $\gamma_{13} = \gamma_{23} = 2\pi \cdot 6$ MHz, $\kappa = 2\pi \cdot 30$ MHz and $\gamma_{12} = 2\pi \cdot 10$ kHz. (c) Experimental data.

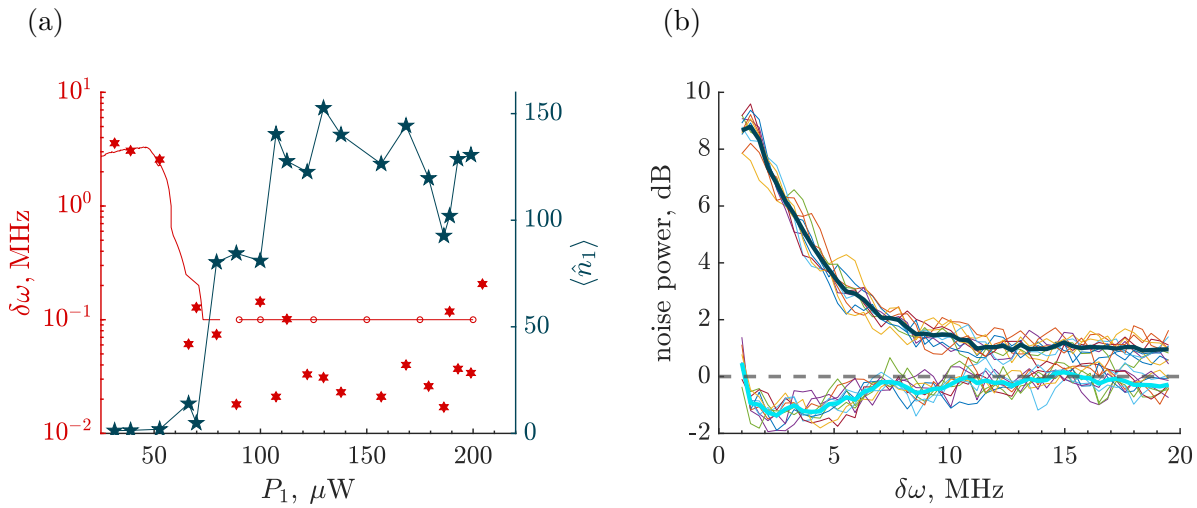

Figure (5.11) (a) The spectrum of signal with a power of the first pump being scanned. Other parameters are fixed: $\Omega_2 = 100\,\mu$W, $\Delta_2 = 30$ MHz. Red hexagons are the experimental data with red line being the theoretical fit. We have extended the theory above the threshold with the same values (line with red circles). Parameters used in calculation $C = 13$, $\gamma_{13} = \gamma_{23} = 2\pi \cdot 6$ MHz, $\kappa = 2\pi \cdot 30$ MHz and $\gamma_{12} = 2\pi \cdot 10$ kHz. (b) The spectrum of squeezing and anti-squeezing levels averaged over 10 sets.

of cooperativity and stay constant for different pump powers. However, for tightly focused pumps their inhomogeneous beam profile produces a transverse Stark shift that reduces the collective coherent enhancement and hence the gain. Thus at high pump powers we have discrepancy between theory and experiment.

As we can see from Figure 5.11(a) as we approach the threshold the linewidth of the generated light significantly reduces. The observed dependence of the rapid decrease of signal bandwidth stops at $\sim$ 100 kHz, which corresponds to the linewidth of the Master laser and this limits the ultimate gain bandwidth.

5.3.2 Experimental results on continuous TMS

For observing the squeezing we decrease the pump power to make sure that operational conditions are below the coherent generation (see map 5.10). In Figure 5.12 we present the traces from two homodyne detectors, which we acquire during 200 μs, while both pumps are present (Fig. 5.8). The traces are normalized by the standard deviation of the signals in

absence of the pumps (standard quantum limit). We keep all phases locked to demonstrate correlation between the same quadratures X_1 and X_2. Single channel homodyne output is expected to be in a thermal state, i.e., having super-Poisson distribution in photon numbers and Gaussian distribution in the phase space. In other words, the signals have a standard deviation larger than the one for the vacuum (see Fig. 5.12(a)).

To establish the entanglement we find the sum and difference between traces or quadratures (Fig. 5.12(b)). From the distributions on the right inset we can find squeezing and anti-squeezing levels via this formula $10\log\left(\frac{\mathrm{Std}^2}{2}\right)$. For the specified set of data we have these values: -1.35 dB of squeezing and 7.1 dB of anti-squeezing.

We account for losses via formula (2.30), where optical and detection losses are 35% in each channel. The corrected squeezing level is -2.3 dB. However, for the same parametric gain the anti-squeezing level is 1.65 dB (or corrected 2.3 dB), which is far from the measured value. The remaining disbalance between measured squeezing and anti-squeezing levels is attributed to the non-ideal efficiency of correlated pair generation akin to efficiency in the DLCZ protocol. Thus we can estimate the efficiency of correlated pair generation by fitting squeezing and anti-squeezing levels by Equation (2.30), where an additional 43% of losses in both channels match the theory with the experiment.

Another important characteristic is bandwidth of squeezing (Fig. 5.11(b)), which determines the correlation time between the two modes. To obtain the spectrum we applied a low-pass filter digitally and searched for a squeezing level. This bandwidth reconciles with our theoretical estimation (see Fig. 5.11). At small pump powers the bandwidth is mostly dictated by the natural linewidth of optical transition, which is 6 MHz (Table 4.1).

One more way to monitor squeezing is to scan through quadratures by varying the phase of one of the LOs or one of the signals. In fact the phase is always scanned as the air and optics vibrate, however a more predictable way is to scan one of the mirrors with a piezo actuator. We used a slightly different frequency for one AOM controlling the pump that effectively scanned the phase in a bigger frequency range (see Fig. 5.13). In this figure it is

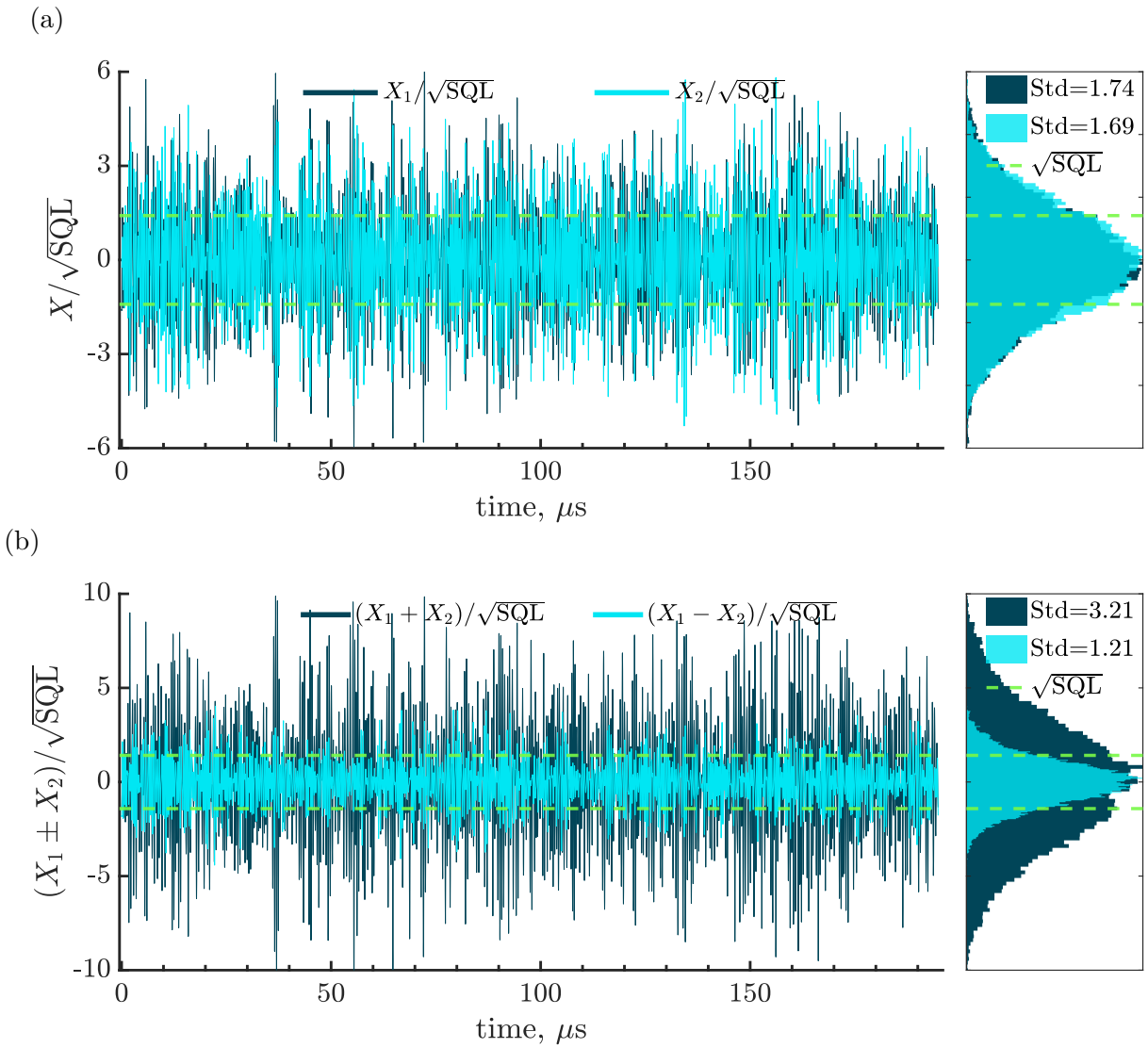

Figure (5.12) (a) The signal measured by each homodyne detector during 200 μs of acquisition. (b) Sum and difference between the signals from subfigure (a) show antisqueezing and squeezing in the time domain correspondingly. The inset on the right demonstrates the quadrature distribution (a) of Stokes and anti-Stokes photons and (b) of sum and difference between two channels.

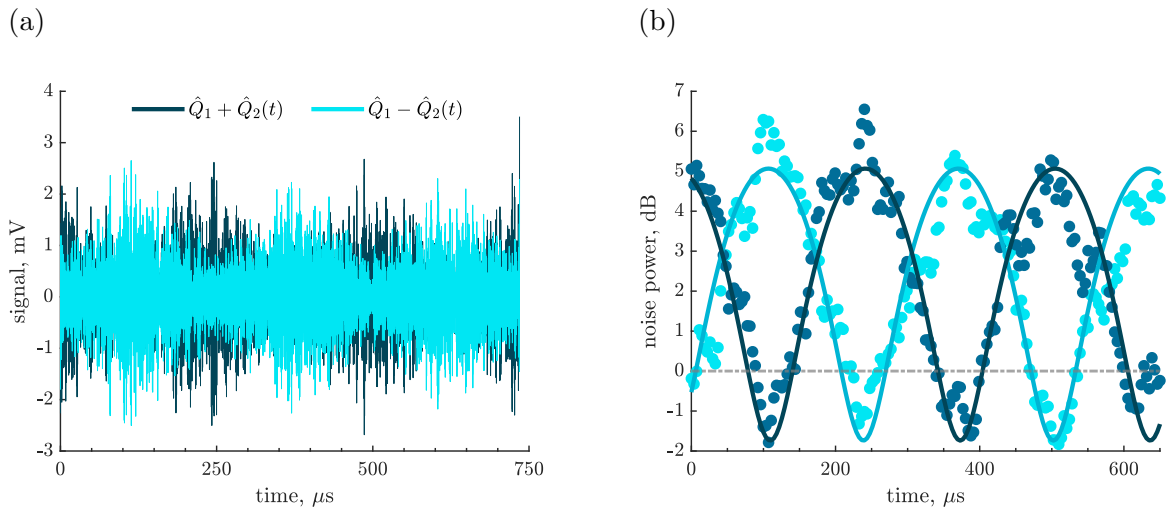

Figure (5.13) The signal scanned by detuning of AOM frequency by 4 kHz. (a) Raw data acquired with an oscilloscope. (b) Processed data, which is a ratio of the signal to the shot noise and the fit.

clearly visible how the noise of sum/difference between two channels changes from high noise levels to low with a scanning period of 250 μs. Naturally, the sum and difference change out of phase (Section 2.1.3). As in a no-scanning regime we divide the signal by the shot noise level and find the squeezing and anti-squeezing levels (Fig. 5.13(b)). The curve is fit with a simple beam-splitter model of losses (Eq. 2.30). The averaged -1.9 dB of squeezing corresponds to the corrected -3.7 dB. The efficiency of generation of correlated pairs is 55%, which follows from the antisqueezing level.

5.4 Conclusion

In this chapter we summarize limitations of our experimental setup as a source of the two-mode squeezed vacuum. By measuring the weak resonant light from the cavity we find the cooperativity parameter. We show that the developed system can operate in the regime of optical parametric oscillator. We characterize the system by monitoring the threshold conditions, bandwidth and intensity of generated signals below the threshold. We show consistency between our experimental data and the theory introduced in Chapter 2. We provide results on continuous TMS, where we obtain 1–2 dB of squeezing without account-

ing for losses. The optical and detection losses are 35% per channel, thus the corrected squeezing level is -2.3 to -3.7 dB. We estimate conditional efficiency of correlated photon generation pairs from our atomic ensemble to be up to 55%.

The paper relevant to this chapter is in preparation.

Chapter 6

Conclusion and Outlook

Here I summarize the key findings of the thesis.

In Chapter 2, we give the necessary theoretical background for the generation of two-mode squeezing in atomic media. We begin the chapter with an overview of the main properties of the two-mode squeezed light. We review squeezing generated via parametric processes and indicate immanent limitations, such as losses and limited gain. We show how the use of a cavity together with the nonlinear media enhances squeezing and modifies its bandwidth.

We build a model to describe the generation of two-mode squeezing in cold atoms coupled to a cavity. To do this, we present the necessary theoretical background for the description of the interaction between the cavity field and ensemble of two-level atoms. To quantify the coherent interaction between light and atoms, the cooperativity parameter is introduced, and its measurement via the light reflected from the cavity is discussed.

The model is further extended to three-level atoms that interact with two cavity modes to describe the desirable FWM in cold atoms. The approximations for getting the analytically solvable system of equations are introduced and justified numerically. The link between the obtained equations for the two cavity modes and generalized OPO is discussed. The various regimes of two-mode light generation are presented, such as coherent generation above the threshold and different types of asymmetrical generation below the threshold. An appearance

of the above-the-threshold regime is quantified depending on the experimentally accessible control parameters. Based on the analysis, the intuitive strategy for enhancing two-mode squeezing is proposed.

In Chapter 3, we introduce a new type of two-mode resonant transparency that is not based on EIT. The TMS state with a specific parametric gain parameter is not absorbed by the resonant media, because of quantum interference between the two optical modes. The proposed phenomenon leads to generation of narrow-band TMS light through dissipation rather than conventional unitary evolution. The optical dark state discovered is a new type of resonant transparency. While indirect experimental evidence through two-mode squeezing generation exists, direct experimental justification is needed. The described mechanism of dark state formation can be generalized for light-atom interaction depending on atomic ensemble polarization, and therefore, this mechanism can be used for generation of more complex quantum states of light. The use of cavity modes instead of free space may bring new phenomena. This requires additional studies.

Chapter 4 is devoted to the description of experimental apparatus for the generation of TMS state in a cold atomic ensemble. First, the main components for the obtaining of a cold atomic cloud are listed. Secondly, the custom vacuum chamber and the pumping process for obtaining a high vacuum are described. Thirdly, the roles and properties of constructed lasers are reviewed. The different techniques of frequency stabilization are listed accordingly to their performance and frequency stabilization requirements. The obtained cold atomic cloud of ^{87}Rb in a magneto-optical trap is characterized by the time of flight measurement.

In the subsequent section we choose the appropriate optical cavity design and parameters. The Pound-Drever-Hall stabilization technique is used to keep the cavity's length constant. All blocks of the experiment are controlled by the time sequencer, which is based on direct digital synthesizers and microcontrollers. This electronic control system is versatile and allows easy modifications while an experiment runs. We discuss its performance and limitations. The measurement of the quantum correlations of two modes of light is done via

two optical homodyne detectors. We cover the basic principles of their operation and highlight particularities of their operation. The acquisition and analysis of homodyne outputs is realized via the high-speed analog-to-digital converter, the details of which are discussed in the last section of the chapter.

The system we built is versatile and capable of generating different types of quantum states. In Chapter 5, this system was shown to operate as the generalized OPO having several regimes. Its properties were examined theoretically and experimentally. The regime suitable for generation of entangled light was identified, and the TMS state, with the squeezing factor below -3.7 dB and the efficiency of the pair creation up to 60%, was demonstrated.

The main limitation for further increase of the efficiency in our setup was the lack of power for pumps in order to increase further single photon detuning while maintaining high enough gain. The increased detuning would eliminate losses in both modes due to direct absorption. The use of a ring cavity with a large waist can eliminate the inhomogeneities of light-atom coupling and hence improve the efficiency of pair creation to above 79% [39]. Moreover, the ring cavity enables efficient splitting of signals and pumps, thereby reducing our optical losses from 20% to 10% or less. Use of both photodiodes having larger quantum efficiency and polarization optics with a better extinction ratio would increase the detection efficiency up to 90% [12].

Our experimental system has the potential to be significantly improved in the future. To achieve this, one major improvement is to introduce an optical dipole trap (unaffordable at the time the setup was built). If we trap atoms in the optical dipole trap, the hyperfine coherence time can be increased by three orders of magnitude, since atoms are confined in the interaction area [42]. This provides a way for the long time storage of continuous-variable entanglement between light and atoms. Additionally, the large trapping time would enable the continuous generation of TMSV on a minute time scale [38] rather than the quasi-continuous generation for milliseconds. These improvements can make the system suitable for the generation of high-purity TMS and long-time quantum memory akin to the DLCZ

protocol.

The experimental setup that we built is unassembled and our work at present will not be continued in this group. Despite this, our findings are instructive and inspiring for further research on quantum repeaters with light and atoms. Long-term perspectives can include the investigation of a potential purification scheme to reduce the effect of optical losses on the two-mode squeezed state. Together with this, the temporal, spatial, and frequency multiplexing can lead to larger entanglement generation rates.

Bibliography

[1] A. Einstein, B. Podolsky, and N. Rosen. Can quantum-mechanical description of physical reality be considered complete? *Phys. Rev.*, 47:777–780, May 1935.

[2] R. E. Slusher, L. W. Hollberg, B. Yurke, J. C. Mertz, and J. F. Valley. Observation of squeezed states generated by four-wave mixing in an optical cavity. *Phys. Rev. Lett.*, 55:2409–2412, Nov 1985.

[3] Ling-An Wu, H. J. Kimble, J. L. Hall, and Huifa Wu. Generation of squeezed states by parametric down conversion. *Phys. Rev. Lett.*, 57:2520–2523, Nov 1986.

[4] A. Heidmann, R. J. Horowicz, S. Reynaud, E. Giacobino, C. Fabre, and G. Camy. Observation of quantum noise reduction on twin laser beams. *Phys. Rev. Lett.*, 59:2555–2557, Nov 1987.

[5] Samuel L. Braunstein and Peter van Loock. Quantum information with continuous variables. *Rev. Mod. Phys.*, 77:513–577, Jun 2005.

[6] A. Furusawa, J. L. Sørensen, S. L. Braunstein, C. A. Fuchs, H. J. Kimble, and E. S. Polzik. Unconditional quantum teleportation. *Science*, 282(5389):706–709, 1998.

[7] Earl T. Campbell, Marco G. Genoni, and Jens Eisert. Continuous-variable entanglement distillation and noncommutative central limit theorems. *Phys. Rev. A*, 87:042330, Apr 2013.

[8] Petr M. Anisimov, Gretchen M. Raterman, Aravind Chiruvelli, William N. Plick, Sean D. Huver, Hwang Lee, and Jonathan P. Dowling. Quantum metrology with two-mode squeezed vacuum: Parity detection beats the heisenberg limit. *Phys. Rev. Lett.*, 104:103602, Mar 2010.

[9] Raul Carranza and Christopher C. Gerry. Photon-subtracted two-mode squeezed vacuum states and applications to quantum optical interferometry. *JOSA B*, 29(9):2581–2587, 2012.

[10] Lars S. Madsen, Vladyslav C. Usenko, Mikael Lassen, Radim Filip, and Ulrik L. Andersen. Continuous variable quantum key distribution with modulated entangled states. *Nat. Commun.*, 3:1083, Sep 2012.

[11] Frédéric Grosshans and Philippe Grangier. Reverse reconciliation protocols for quantum cryptography with continuous variables. *arXiv preprint quant-ph/0204127*, 2002.

[12] Tobias Eberle, Vitus Händchen, and Roman Schnabel. Stable control of 10 db two-mode squeezed vacuum states of light. *Opt. Express*, 21(9):11546–11553, May 2013.

[13] R. M. Shelby, M. D. Levenson, S. H. Perlmutter, R. G. DeVoe, and D. F. Walls. Broadband parametric deamplification of quantum noise in an optical fiber. *Phys. Rev. Lett.*, 57:691–694, Aug 1986.

[14] Quentin Glorieux, Luca Guidoni, Samuel Guibal, Jean-Pierre Likforman, and Thomas Coudreau. Quantum correlations by four-wave mixing in an atomic vapor in a nonamplifying regime: Quantum beam splitter for photons. *Phys. Rev. A*, 84:053826, Nov 2011.

[15] Vincent Boyer, Alberto M. Marino, Raphael C. Pooser, and Paul D. Lett. Entangled images from four-wave mixing. *Science*, 321(5888):544–547, 2008.

[16] F. Marin, A. Bramati, E. Giacobino, T. C. Zhang, J. Ph. Poizat, J. F. Roch, and P. Grangier. Squeezing and intermode correlations in laser diodes. *Phys. Rev. Lett.*, 75:4606–4609, Dec 1995.

[17] A. Pontin, M. Bonaldi, A. Borrielli, L. Marconi, F. Marino, G. Pandraud, G. A. Prodi, P. M. Sarro, E. Serra, and F. Marin. Dynamical two-mode squeezing of thermal fluctuations in a cavity optomechanical system. *Phys. Rev. Lett.*, 116:103601, Mar 2016.

[18] Patrick M. Ledingham, William R. Naylor, and Jevon J. Longdell. Experimental realization of light with time-separated correlations by rephasing amplified spontaneous emission. *Phys. Rev. Lett.*, 109:093602, Aug 2012.

[19] Kate R. Ferguson, Sarah E. Beavan, Jevon J. Longdell, and Matthew J. Sellars. Generation of light with multimode time-delayed entanglement using storage in a solid-state spin-wave quantum memory. *Phys. Rev. Lett.*, 117:020501, Jul 2016.

[20] C. Eichler, D. Bozyigit, C. Lang, M. Baur, L. Steffen, J. M. Fink, S. Filipp, and A. Wallraff. Observation of two-mode squeezing in the microwave frequency domain. *Phys. Rev. Lett.*, 107:113601, Sep 2011.

[21] D. M. Meekhof, C. Monroe, B. E. King, W. M. Itano, and D. J. Wineland. Generation of nonclassical motional states of a trapped atom. *Phys. Rev. Lett.*, 76:1796–1799, Mar 1996.

[22] A. Lambrecht, T. Coudreau, A. M. Steinberg, and E. Giacobino. Squeezing with cold atoms. *EPL*, 36(2):93–98, Oct 1996.

[23] V. Josse, A. Dantan, A. Bramati, M. Pinard, and E. Giacobino. Continuous variable entanglement using cold atoms. *Phys. Rev. Lett.*, 92:123601, Mar 2004.

[24] Lu-Ming Duan, G. Giedke, J. I. Cirac, and P. Zoller. Inseparability criterion for continuous variable systems. *Phys. Rev. Lett.*, 84:2722–2725, Mar 2000.

[25] C. F. McCormick, V. Boyer, E. Arimondo, and P. D. Lett. Strong relative intensity squeezing by four-wave mixing in rubidium vapor. *Opt. Lett.*, 32(2):178–180, Jan 2007.

[26] Ulrik L Andersen, Tobias Gehring, Christoph Marquardt, and Gerd Leuchs. 30 years of squeezed light generation. *Physica Scripta*, 91(5):053001, 2016.

[27] A. M. Marino, R. C. Pooser, V. Boyer, and P. D. Lett. Tunable delay of Einstein-Podolsky-Rosen entanglement. *Nature*, 457(7231):859, Feb 2009.

[28] C. F. McCormick, A. M. Marino, V. Boyer, and P. D. Lett. Strong low-frequency quantum correlations from a four-wave-mixing amplifier. *Phys. Rev. A*, 78:043816, Oct 2008.

[29] W. Wasilewski, T. Fernholz, K. Jensen, L. S. Madsen, H. Krauter, C. Muschik, and E. S. Polzik. Generation of two-mode squeezed and entangled light in a single temporal and spatial mode. *Opt. Express*, 17(16):14444–14457, Aug 2009.

[30] L.-M. Duan, M. D. Lukin, J. Ignacio Cirac, and P. Zoller. Long-distance quantum communication with atomic ensembles and linear optics. *Nature*, 414(6862):413–418, Nov 2001.

[31] Alexey V. Gorshkov, Axel André, Mikhail D. Lukin, and Anders S. Sørensen. Photon storage in Λ-type optically dense atomic media. ii. free-space model. *Phys. Rev. A*, 76:033805, Sep 2007.

[32] A. Kuzmich, W. P. Bowen, A. D. Boozer, A. Boca, C. W. Chou, L.-M. Duan, and H. J. Kimble. Generation of nonclassical photon pairs for scalable quantum communication with atomic ensembles. *Nature*, 423(6941):731–734, Jun 2003.

[33] D. N. Matsukevich and A. Kuzmich. Quantum state transfer between matter and light. *Science*, 306(5696):663–666, 2004.

[34] Boris Albrecht, Pau Farrera, Georg Heinze, Matteo Cristiani, and Hugues de Riedmatten. Controlled rephasing of single collective spin excitations in a cold atomic quantum memory. *Phys. Rev. Lett.*, 115:160501, Oct 2015.

[35] Yunfei Pu, Yukai Wu, Nan Jiang, Wei Chang, Chang Li, Sheng Zhang, and Luming Duan. Experimental entanglement of 25 individually accessible atomic quantum interfaces. *Sci. Adv.*, 4(4):eaar3931, 2018.

[36] R. Zhao, Y. O. Dudin, S. D. Jenkins, C. J. Campbell, D. N. Matsukevich, T. A. B. Kennedy, and A. Kuzmich. Long-lived quantum memory. *Nat. Phys.*, 5:100–104, Dec 2008.

[37] A. G. Radnaev, Y. O. Dudin, R. Zhao, H. H. Jen, S. D. Jenkins, A. Kuzmich, and T. A. B. Kennedy. A quantum memory with telecom-wavelength conversion. *Nat. Phys.*, 6:894–899, Sep 2010.

[38] Y. O. Dudin, L. Li, and A. Kuzmich. Light storage on the time scale of a minute. *Phys. Rev. A*, 87:031801, Mar 2013.

[39] Erwan Bimbard, Rajiv Boddeda, Nicolas Vitrant, Andrey Grankin, Valentina Parigi, Jovica Stanojevic, Alexei Ourjoumtsev, and Philippe Grangier. Homodyne tomography of a single photon retrieved on demand from a cavity-enhanced cold atom memory. *Phys. Rev. Lett.*, 112:033601, Jan 2014.

[40] Sheng-Jun Yang, Xu-Jie Wang, Jun Li, Jun Rui, Xiao-Hui Bao, and Jian-Wei Pan. Highly retrievable spin-wave–photon entanglement source. *Phys. Rev. Lett.*, 114:210501, May 2015.

[41] Xiao-Hui Bao, Andreas Reingruber, Peter Dietrich, Jun Rui, Alexander Dück, Thorsten Strassel, Li Li, Nai-Le Liu, Bo Zhao, and Jian-Wei Pan. Efficient and long-lived quantum memory with cold atoms inside a ring cavity. *Nat. Phys.*, 8(7):517–521, May 2012.

[42] Sheng-Jun Yang, Xu-Jie Wang, Xiao-Hui Bao, and Jian-Wei Pan. An efficient quantum light-matter interface with sub-second lifetime. *Nat. Photonics*, 10:381–384, Apr 2016.

[43] Hidetoshi Katori, Masao Takamoto, V. G. Pal'chikov, and V. D. Ovsiannikov. Ultrastable optical clock with neutral atoms in an engineered light shift trap. *Phys. Rev. Lett.*, 91:173005, Oct 2003.

[44] B. M. Sparkes, J. Bernu, M. Hosseini, J. Geng, Q. Glorieux, P. A. Altin, P. K. Lam, N. P. Robins, and B. C. Buchler. An ultra-high optical depth cold atomic ensemble for quantum memories. *J. Phys. Conf. Ser.*, 467:012009, Dec 2013.

[45] Michał Dabrowski, Michał Parniak, and Wojciech Wasilewski. Einstein–Podolsky–Rosen paradox in a hybrid bipartite system. *Optica*, 4(2):272–275, 2017.

[46] Josephine Dias and T. C. Ralph. Quantum repeaters using continuous-variable teleportation. *Phys. Rev. A*, 95:022312, Feb 2017.

[47] Fabian Furrer and William J. Munro. Repeaters for continuous-variable quantum communication. *Phys. Rev. A*, 98:032335, Sep 2018.

[48] Pieter Kok and Brendon W. Lovett. *Introduction to Optical Quantum Information Processing*. Cambridge University Press, 2010.

[49] A. Furusawa and P. van Loock. *Quantum Teleportation and Entanglement: A Hybrid Approach to Optical Quantum Information Processing*. Wiley, Berlin, 2011.

[50] P. van Loock. Optical hybrid approaches to quantum information. *Laser & Photonics Reviews*, 5(2):167–200, 2011.

[51] Ulrik L. Andersen, Jonas S. Neergaard-Nielsen, Peter Van Loock, and Akira Furusawa. Hybrid discrete-and continuous-variable quantum information. *Nat. Phys.*, 11(9):713, Sep.

[52] Hermann A. Haus. *Electromagnetic Noise and Quantum Optical Measurements*. Springer Science & Business Media, 2012.

[53] M. O. Scully and S. M. Zubairy. *Quantum Optics*. Cambridge Univ. Press, 1997.

[54] Fulvio Flamini, Nicolò Spagnolo, and Fabio Sciarrino. Photonic quantum information processing: a review. *Rep. Prog. Phys.*, 82(1):016001, Nov 2018.

[55] Nicolas Gisin, Grégoire Ribordy, Wolfgang Tittel, and Hugo Zbinden. Quantum cryptography. *Rev. Mod. Phys.*, 74(1):145–195, Mar 2002.

[56] John S. Bell. *Speakable and Unspeakable In Quantum Mechanics*. Cambridge University Press, 1987.

[57] R. Paschotta. Birefringent phase matching. *Encyclopedia of Laser Physics and Technology*, 2008.

[58] Morton H. Rubin, David N. Klyshko, Y. H. Shih, and A. V. Sergienko. Theory of two-photon entanglement in type-ii optical parametric down-conversion. *Phys. Rev. A*, 50:5122–5133, Dec 1994.

[59] Andrei B. Klimov and Sergei M. Chumakov. *A Group-Theoretical Approach to Quantum Optics: Models of Atom-Field Interactions*. John Wiley & Sons, 2009.

[60] U. Leonhardt. *Measuring the Quantum State of Light*. Cambridge Studies in Modern Optics. Cambridge University Press, 1997.

[61] Daniel F. Walls and Gerard J. Milburn. *Quantum Optics*. Springer Science & Business Media, 2007.

[62] Roger Gehr, Jürgen Volz, Guilhem Dubois, Tilo Steinmetz, Yves Colombe, Benjamin L. Lev, Romain Long, Jérôme Estève, and Jakob Reichel. Cavity-based single atom preparation and high-fidelity hyperfine state readout. *Phys. Rev. Lett.*, 104:203602, May 2010.

[63] Michael Tavis and Frederick W. Cummings. Exact solution for an n-molecule—radiation-field hamiltonian. *Phys. Rev.*, 170:379–384, Jun 1968.

[64] Ravinder R. Puri. *Mathematical Methods of Quantum Optics*, volume 79. Springer Science & Business Media, 2001.

[65] Marcis Auzinsh, Dmitry Budker, and Simon Rochester. *Optically Polarized Atoms: Understanding Light-Atom Interactions*. Oxford University Press, 2010.

[66] Howard Carmichael. *An open systems approach to quantum optics: lectures presented at the Université Libre de Bruxelles, October 28 to November 4, 1991*, volume 18. Springer Science & Business Media, 2009.

[67] Daniel A Steck. Rubidium 87 D line data, 2001.

[68] Michael Fleischhauer, Atac Imamoglu, and Jonathan P. Marangos. Electromagnetically induced transparency: Optics in coherent media. *Rev. Mod. Phys.*, 77:633–673, Jul 2005.

[69] M. Sargent, M. O. Scully, and W. E. Lamb. *Laser Physics*. Addison-Wesley Publishing Co., 1974.

[70] Nikolai Lauk, Christopher O'Brien, and Michael Fleischhauer. Fidelity of photon propagation in electromagnetically induced transparency in the presence of four-wave mixing. *Phys. Rev. A*, 88:013823, Jul 2013.

[71] Bo Zhao, Yu-Ao Chen, Xiao-Hui Bao, Thorsten Strassel, Chih-Sung Chuu, Xian-Min Jin, Jörg Schmiedmayer, Zhen-Sheng Yuan, Shuai Chen, and Jian-Wei Pan. A mil-

lisecond quantum memory for scalable quantum networks. *Nat. Phys.*, 5(2):95–99, Dec 2009.

[72] Leonard Mandel and Emil Wolf. *Optical Coherence and Quantum Optics*. Cambridge university press, 1995.

[73] Yefeng Mei, Xianxin Guo, Luwei Zhao, and Shengwang Du. Mirrorless optical parametric oscillation with tunable threshold in cold atoms. *Phys. Rev. Lett.*, 119(15):150406, Oct 2017.

[74] A. Aspect, E. Arimondo, R. Kaiser, N. Vansteenkiste, and C. Cohen-Tannoudji. Laser cooling below the one-photon recoil energy by velocity-selective coherent population trapping. *Phys. Rev. Lett.*, 61:826–829, Aug 1988.

[75] M. Fleischhauer and M. D. Lukin. Quantum memory for photons: Dark-state polaritons. *Phys. Rev. A*, 65:022314, Jan 2002.

[76] Jian Li, G. S. Paraoanu, Katarina Cicak, Fabio Altomare, Jae I. Park, Raymond W. Simmonds, Mika A. Sillanpää, and Pertti J. Hakonen. Decoherence, autler-townes effect, and dark states in two-tone driving of a three-level superconducting system. *Phys. Rev. B*, 84:104527, Sep 2011.

[77] S. Novikov, T. Sweeney, J. E. Robinson, S. P. Premaratne, B. Suri, F. C. Wellstood, and B. S. Palmer. Raman coherence in a circuit quantum electrodynamics lambda system. *Nat. Phys.*, 12:75–79, Nov 2015.

[78] Ziliang Ye, Ting Cao, Kevin O'Brien, Hanyu Zhu, Xiaobo Yin, Yuan Wang, Steven G. Louie, and Xiang Zhang. Probing excitonic dark states in single-layer tungsten disulphide. *Nature*, 513(7517):214–218, Sep 2014.

[79] Xiao-Xiao Zhang, Yumeng You, Shu Yang Frank Zhao, and Tony F. Heinz. Experimental evidence for dark excitons in monolayer WSe_2. *Phys. Rev. Lett.*, 115:257403, Dec 2015.

[80] Mikhail I. Kolobov. The spatial behavior of nonclassical light. *Rev. Mod. Phys.*, 71:1539–1589, Oct 1999.

[81] Nathaniel B. Phillips, Alexey V. Gorshkov, and Irina Novikova. Light storage in an optically thick atomic ensemble under conditions of electromagnetically induced transparency and four-wave mixing. *Phys. Rev. A*, 83:063823, Jun 2011.

[82] Klemens Hammerer, Anders S. Sørensen, and Eugene S. Polzik. Quantum interface between light and atomic ensembles. *Rev. Mod. Phys.*, 82:1041–1093, Apr 2010.

[83] T. Holstein and H. Primakoff. Field dependence of the intrinsic domain magnetization of a ferromagnet. *Phys. Rev.*, 58:1098–1113, Dec 1940.

[84] E. S. Moiseev, Arina Tashchilina, S. A. Moiseev, and A. I. Lvovsky. Darkness of two-mode squeezed light in {\Lambda}-type atomic system. *arXiv preprint arXiv:1803.08911*, 2018.

[85] A. I. Lvovsky. *Squeezed Light*, pages 121–163. John Wiley & Sons, Inc., 2015.

[86] A. E. Kozhekin, K. Mølmer, and E. Polzik. Quantum memory for light. *Phys. Rev. A*, 62:033809, Aug 2000.

[87] M. Hosseini, B. M. Sparkes, G. Campbell, P. K. Lam, and B. C. Buchler. High efficiency coherent optical memory with warm rubidium vapour. *Nat. Commun.*, 2:174, Feb 2011.

[88] Daniel B. Higginbottom, Jiao Geng, Geoff T. Campbell, Mahdi Hosseini, Ming Tao Cao, Ben M. Sparkes, Julian Bernu, Nick P. Robins, Ping Koy Lam, and Ben C. Buchler. Dual-rail optical gradient echo memory. *Opt. Express*, 23(19):24937–24944, 2015.

[89] E. S. Moiseev and S. A. Moiseev. Scalable time reversal of raman echo quantum memory and quantum waveform conversion of light pulse. *New J. Phys.*, 15(10):105005, 2013.

[90] Christine A. Muschik, Eugene S. Polzik, and J. Ignacio Cirac. Dissipatively driven entanglement of two macroscopic atomic ensembles. *Phys. Rev. A*, 83:052312, May 2011.

[91] Hanna Krauter, Christine A. Muschik, Kasper Jensen, Wojciech Wasilewski, Jonas M. Petersen, J. Ignacio Cirac, and Eugene S. Polzik. Entanglement generated by dissipation and steady state entanglement of two macroscopic objects. *Phys. Rev. Lett.*, 107:080503, Aug 2011.

[92] L. F. Buchmann and D. M. Stamper-Kurn. Nondegenerate multimode optomechanics. *Phys. Rev. A*, 92:013851, Jul 2015.

[93] Nicolas Spethmann, Jonathan Kohler, Sydney Schreppler, Lukas Buchmann, and Dan M. Stamper-Kurn. Cavity-mediated coupling of mechanical oscillators limited by quantum back-action. *Nat. Phys.*, 12:27–31, Oct 2015.

[94] Jonathan Kohler, Justin A. Gerber, Emma Dowd, and Dan M. Stamper-Kurn. Negative-mass instability of the spin and motion of an atomic gas driven by optical cavity backaction. *Phys. Rev. Lett.*, 120:013601, Jan 2018.

[95] Ying-Dan Wang and Aashish A. Clerk. Reservoir-engineered entanglement in optomechanical systems. *Phys. Rev. Lett.*, 110:253601, Jun 2013.

[96] Chunhua Dong, Victor Fiore, Mark C. Kuzyk, and Hailin Wang. Optomechanical dark mode. *Science*, 338(6114):1609–1613, 2012.

[97] Mankei Tsang and Carlton M. Caves. Evading quantum mechanics: Engineering a classical subsystem within a quantum environment. *Phys. Rev. X*, 2:031016, Sep 2012.

[98] W. Wasilewski, K. Jensen, H. Krauter, J. J. Renema, M. V. Balabas, and E. S. Polzik. Quantum noise limited and entanglement-assisted magnetometry. *Phys. Rev. Lett.*, 104:133601, Mar 2010.

[99] L. Ricci, M. Weidemüller, T. Esslinger, A. Hemmerich, C. Zimmermann, V. Vuletic, W. König, and T. W. Hänsch. A compact grating-stabilized diode laser system for atomic physics. *Opt. Comm.*, 117(5-6):541–549, Jun 1995.

[100] Ye Cunyun. *Tunable External Cavity Diode Lasers*. World Scientific, 2004.

[101] Jurgen Appel. *A light-atom quantum interface based on electromagnetically induced transparency*. PhD thesis, 2007.

[102] P. W. Smith and R. Hänsch. Cross-relaxation effects in the saturation of the 6328-å neon-laser line. *Phys. Rev. Lett.*, 26:740–743, Mar 1971.

[103] Kristan L. Corwin, Zheng-Tian Lu, Carter F. Hand, Ryan J. Epstein, and Carl E. Wieman. Frequency-stabilized diode laser with the zeeman shift in an atomic vapor. *Appl. Opt.*, 37(15):3295–3298, May 1998.

[104] H. R. Telle, D. Meschede, and T. W. Hänsch. Realization of a new concept for visible frequency division: phase locking of harmonic and sum frequencies. *Opt. Lett.*, 15(10):532–534, May 1990.

[105] Jürgen Appel, Andrew MacRae, and A. I. Lvovsky. A versatile digital ghz phase lock for external cavity diode lasers. *Meas. Sci. Technol.*, 20(5):055302, 2009.

[106] D. A. Tulchinsky. Sub 23 μhz instantaneous linewidth and frequency stability measurements of the beat note from an offset phase locked single frequency heterodyned nd: Yag laser system. *Opt. Express*, 25(20):24119–24137, 2017.

[107] Pantita Palittapongarnpim, Andrew MacRae, and A. I. Lvovsky. Note: A monolithic filter cavity for experiments in quantum optics. *Rev. Sci. Instrum.*, 83(6):066101, May 2012.

[108] Isabelle Petitbon, Philippe Gallion, Guy Debarge, and Claude Chabran. Locking bandwidth and relaxation oscillations of an injection-locked semiconductor laser. *IEEE J. Quantum Electron.*, 24(2):148–154, 1988.

[109] Bo Jing, Xu-Jie Wang, Yong Yu, Peng-Fei Sun, Yan Jiang, Sheng-Jun Yang, Wen-Hao Jiang, Xi-Yu Luo, Jun Zhang, Xiao Jiang, et al. Entanglement of three quantum memories via interference of three single photons. *Nat. Photonics*, 13(3):210, 2019.

[110] Alexander Keesling, Ahmed Omran, Harry Levine, Hannes Bernien, Hannes Pichler, Soonwon Choi, Rhine Samajdar, Sylvain Schwartz, Pietro Silvi, Subir Sachdev, et al. Quantum kibble–zurek mechanism and critical dynamics on a programmable rydberg simulator. *Nature*, 568:207–211, 2019.

[111] Massimo Inguscio and Leonardo Fallani. *Atomic Physics: Precise Measurements and Ultracold Matter*. OUP Oxford, 2013.

[112] Christopher J. Foot. *Atomic Physics*, volume 7. Oxford University Press, 2005.

[113] Harold J. Metcalf and Peter Van der Straten. Laser cooling and trapping of neutral atoms. *The Optics Encyclopedia: Basic Foundations and Practical Applications*, 2007.

[114] Claude N. Cohen-Tannoudji. Nobel lecture: Manipulating atoms with photons. *Rev. Mod. Phys.*, 70:707–719, Jul 1998.

[115] Jean Dalibard and Claude Cohen-Tannoudji. Laser cooling below the doppler limit by polarization gradients: simple theoretical models. *JOSA B*, 6(11):2023–2045, 1989.

[116] Warren Nagourney. *Quantum Electronics for Atomic Physics and Telecommunication*. OUP Oxford, 2014.

[117] R. W. P. Drever, John L. Hall, F. V. Kowalski, J. Hough, G. M. Ford, A. J. Munley, and H. Ward. Laser phase and frequency stabilization using an optical resonator. *Appl. Phys. B*, 31(2):97–105, Feb 1983.

[118] Harald T Friis. Noise figures of radio receivers. *Proceedings of the IRE*, 32(7):419–422, 1944.

[119] Carlos L. Garrido Alzar, Plamen G. Petrov, Daniel Oblak, Joerg H. Mueller, and Eugene S. Polzik. Compensation of eddy-current-induced magnetic field transients in a mot. *arXiv preprint physics/0701251*, 2007.

[120] Robert H. Hadfield. Single-photon detectors for optical quantum information applications. *Nat. Photonics*, 3:696–705, Dec 2009.

[121] Francesco Mattioli, Zili Zhou, Alessandro Gaggero, Rosalinda Gaudio, Saeedeh Jahanmirinejad, Döndü Sahin, Francesco Marsili, Roberto Leoni, and Andrea Fiore. Photon-number-resolving superconducting nanowire detectors. *Supercond. Sci. Technol.*, 28(10):104001, Aug 2015.

[122] Clinton Cahall, Kathryn L. Nicolich, Nurul T. Islam, Gregory P. Lafyatis, Aaron J. Miller, Daniel J. Gauthier, and Jungsang Kim. Multi-photon detection using a conventional superconducting nanowire single-photon detector. *Optica*, 4(12):1534–1535, Dec 2017.

[123] D. T. Smithey, M. Beck, M. G. Raymer, and A. Faridani. Measurement of the wigner distribution and the density matrix of a light mode using optical homodyne tomography: Application to squeezed states and the vacuum. *Phys. Rev. Lett.*, 70:1244–1247, Mar 1993.

[124] M. G. Raymer, J. Cooper, H. J. Carmichael, M. Beck, and D. T. Smithey. Ultrafast measurement of optical-field statistics by dc-balanced homodyne detection. *JOSA B*, 12(10):1801–1812, Oct 1995.

[125] Jürgen Appel, Dallas Hoffman, Eden Figueroa, and A. I. Lvovsky. Electronic noise in optical homodyne tomography. *Phys. Rev. A*, 75:035802, Mar 2007.

[126] R. Kumar, E. Barrios, A. MacRae, E. Cairns, E. H. Huntington, and A. I. Lvovsky. Versatile wideband balanced detector for quantum optical homodyne tomography. *Opt. Commun.*, 285(24):5259–5267, 2012.

[127] Alexander I. Lvovsky, Barry C. Sanders, and Wolfgang Tittel. Optical quantum memory. *Nat. Photonics*, 3(12):706–714, 2009.

[128] Yen-Wei Lin, Wen-Te Liao, Thorsten Peters, Hung-Chih Chou, Jian-Siung Wang, Hung-Wen Cho, Pei-Chen Kuan, and Ite A. Yu. Stationary light pulses in cold atomic media and without bragg gratings. *Phys. Rev. Lett.*, 102:213601, May 2009.

[129] A. MacRae, T. Brannan, R. Achal, and A. I. Lvovsky. Tomography of a high-purity narrowband photon from a transient atomic collective excitation. *Phys. Rev. Lett.*, 109:033601, Jul 2012.

[130] R. Pulikkoonattu. Oscillator phase noise and sampling clock jitter. Technical report, Citeseer, 2007.

[131] Nikolai Lauk. *Quantum Networks for Photons: Nonlinear Effects in Quantum Memories, Quantum Interfaces and Single-photon Filter*. PhD thesis, Technische Universität Kaiserslautern, 2016.

Appendix A

Langevin operators

To take into account the spontaneous emission the Heisenberg-Langevin approach could be used, where the decay of the coherence $\hat{R}^j_{nm}$ can be expressed in the general form as

$$\frac{d\hat{R}^j_{nm}}{dt} = -\frac{\gamma_{nm}}{2}\hat{R}^j_{nm} - i[\hat{R}^j_{nm}, \hat{\mathcal{H}}_{\mathrm{rf}}] + \hat{F}^j_{nm}, \tag{A.1}$$

where γ_{nm} is the decay constant and $\hat{\mathcal{H}}_{\mathrm{rf}}$ is Hamiltonian (2.65) in the rotating frame. We have assumed, that Langevin noise operator $\hat{F}_{nm}$ is composed from Markov bosonic bath annihilation operator at zero temperature coupled to atomic population difference operator. In turn the equations for population operators have the form:

$$\frac{d\hat{R}^j_{33}}{dt} = -(\gamma_{13} + \gamma_{23})\hat{R}^j_{33} - i[\hat{R}^j_{33}, \hat{\mathcal{H}}_{\mathrm{rf}}] + \hat{F}^j_{33}, \tag{A.2}$$

$$\frac{d\hat{R}^j_{22}}{dt} = \gamma_{23}\hat{R}^j_{33} - i[\hat{R}^j_{22}, \hat{\mathcal{H}}_{\mathrm{rf}}] + \hat{F}^j_{22}, \tag{A.3}$$

$$\frac{d\hat{R}^j_{11}}{dt} = \gamma_{13}\hat{R}^j_{33} - i[\hat{R}^j_{11}, \hat{\mathcal{H}}_{\mathrm{rf}}] + \hat{F}^j_{11} \tag{A.4}$$

The baths for two atomic transitions are assumed independent. Langevin noise operator has zero mean value $\langle\, \hat{F}_{nm}(t) \,\rangle = 0$. In turn, two-time correlator has the delta-type correlation

[53, Ch. 9]:

$$\langle\, \hat{F^i}_{nm}(t) \cdot \hat{F^j}_{n'm'}(t') \,\rangle = \delta(t-t')\delta^i_j \langle\, \hat{F}^j_{nm} \cdot \hat{F}^j_{n'm'} \,\rangle, \tag{A.5}$$

To derive the former correlator we may notice, that these equation has common form

$$\frac{d\hat{z}}{dt} = \hat{A}_z + \hat{F}_z, \tag{A.6}$$

where $\hat{A}_y$ represent deterministic part of the equation, $\hat{F}_y$ is corresponding Langevin noise operator. The former is obtained through generalized Einstein relation [131]:

$$\langle\, \hat{F}_z \hat{F}_x \,\rangle = -\langle\, \hat{z}\hat{A}_x \,\rangle - \langle\, \hat{A}_z \hat{x} \,\rangle + \frac{d}{dt}\langle\, zx \,\rangle \tag{A.7}$$

As the result, the values for correlators are presented in the Table (A.1). Due to linearity of the Fourier transform similar expression takes place for frequency domain Langevin operators $\langle\, \hat{F}^j_{nm}(\omega'), \hat{F}^j_{n'm'}(\omega) \,\rangle = \delta(\omega-\omega')\langle\, \hat{F}^j_{nm}\hat{F}^j_{n'm'} \,\rangle$, where the values for $\langle\, \hat{F}^j_{nm}\hat{F}^j_{n'm'} \,\rangle$ are also presented in the A.1.

A.1 Langevin noise contribution

The contribution of the stochastic operators into the observables happens due to the following superposition of Langevin operators:

$$\delta F_1 = |g_1| \sum_j \frac{e^{-i\mathbf{k}_1\mathbf{r}_j}\left(\tilde{\delta}_1(\omega)\hat{F}^j_{13}(\omega) + \frac{|\Omega_1\Omega_2|}{\tilde{\delta}_2(\omega)} e^{i(\mathbf{k}_{c1}+\mathbf{k}_{c2})\mathbf{r}_j}\hat{F}^j_{32}(\omega) - i|\Omega_1| e^{i\mathbf{k}_{c1}\mathbf{r}_j}\hat{F}^j_{12}(\omega)\right)}{(\gamma_{13}/2 + i\,(\Delta_1-\omega))\left(\tilde{\delta}_1(\omega) + \frac{|\Omega_1|^2}{\gamma_{13}/2+i(\Delta_1-\omega)}\right)} \tag{A.8}$$

$$\delta F_2 = \sum_j \frac{|g_2| e^{i\mathbf{k}_2\mathbf{r}_j}\left(i|\Omega_2| e^{-i\mathbf{k}_{c2}\mathbf{r}_j}\hat{F}^j_{12}(\omega) + \tilde{\delta}_3(\omega)\hat{F}^j_{32}(\omega) + e^{-i(\mathbf{k}_{c1}+\mathbf{k}_{c2})\mathbf{r}_j}\frac{|\Omega_1\Omega_2|}{\gamma_{13}/2+i(\Delta_1-\omega)}\hat{F}^j_{13}(\omega)\right)}{\tilde{\delta}_2(\omega)\left(\tilde{\delta}_1(\omega) + \frac{|\Omega_1|^2}{(\gamma_{13}/2+i(\Delta_1-\omega))}\right)} \tag{A.9}$$

	$\hat{F}^j_{13}\rangle$	$\hat{F}^j_{23}\rangle$	$\hat{F}^j_{12}\rangle$	$\hat{F}^j_{31}\rangle$	$\hat{F}^j_{32}\rangle$	$\hat{F}^j_{21}\rangle$
$\langle\hat{F}^j_{13},$	0	0	0	$\gamma_{13}\langle\,\hat{R}^j_{11}\,\rangle$ $+\gamma_{13}\langle\,\hat{R}^j_{33}\,\rangle$	$\gamma_{32}\langle\,\hat{R}^j_{12}\,\rangle$ $+\gamma_{13}\langle\,\hat{R}^j_{12}\,\rangle$ $-\gamma_{12}\langle\,\hat{R}^j_{12}\,\rangle$	0
$\langle\hat{F}^j_{23},$	0	0	0	$\frac{\gamma_{13}}{2}\langle\,\hat{R}^j_{21}\,\rangle$ $+\frac{\gamma_{23}}{2}\langle\,\hat{R}^j_{21}\,\rangle$ $-\frac{\gamma_{12}}{2}\langle\,\hat{R}^j_{21}\,\rangle$	$\gamma_{23}\langle\,\hat{R}^j_{22}\,\rangle$ $+\gamma_{23}\langle\,\hat{R}^j_{33}\,\rangle$	0
$\langle\hat{F}^j_{12},$	0	$\frac{\gamma_{23}}{2}\langle\,\hat{R}^j_{13}\,\rangle$ $-\frac{\gamma_{13}}{2}\langle\,\hat{R}^j_{13}\,\rangle$ $+\frac{\gamma_{12}}{2}\langle\,\hat{R}^j_{13}\,\rangle$	0	0	0	$\gamma_{12}\langle\,\hat{R}^j_{11}\,\rangle$ $+\gamma_{13}\langle\,\hat{R}^j_{33}\,\rangle$ $+\gamma_{23}\langle\,\hat{R}^j_{33}\,\rangle$
$\langle\hat{F}^j_{31},$	$-\gamma_{23}\langle\,\hat{R}^j_{33}\,\rangle$	$\frac{\gamma_{23}}{2}\langle\,\hat{R}^j_{21}\,\rangle$	$\gamma_{13}\langle\,\hat{R}^j_{32}\,\rangle$ $-\gamma_{23}\langle\,\hat{R}^j_{32}\,\rangle$ $+\gamma_{12}\langle\,\hat{R}^j_{32}\,\rangle$	0	0	0
$\langle\hat{F}^j_{32},$	0	$-\gamma_{13}\langle\,\hat{R}^j_{33}\,\rangle$	0	0	0	$\frac{\gamma_{12}}{2}\langle\,\hat{R}^j_{13}\,\rangle$
$\langle\hat{F}^j_{21},$	$\frac{\gamma_{13}}{2}\langle\,\hat{R}^j_{23}\,\rangle$ $-\frac{\gamma_{23}}{2}\langle\,\hat{R}^j_{23}\,\rangle$ $+\frac{\gamma_{12}}{2}\langle\,\hat{R}^j_{23}\,\rangle$	0	$\gamma_{32}\langle\,\hat{R}^j_{33}\,\rangle$ $+\gamma_{12}\langle\,\hat{R}^j_{22}\,\rangle$	0	0	0

Table (A.1) Langevin correlators matrix

The summation over atoms is replaced with one dimensional integration along the medium as it was for inclusion of the standing wave effects. The integration damps the contribution of the cross-correlators with the phase matching factor $\mathrm{sinc}(\delta kl) \sim 10^{-3}$, what makes same operator correllators negligible $\langle\,\delta\tilde{F}_{1,2}\cdot\delta\tilde{F}_{1,2}\,\rangle = \langle\,\delta\tilde{F}^\dagger_{1,2}\cdot\delta\tilde{F}^\dagger_{1,2}\,\rangle \approx 0$. Only the terms proportional to the product of conjugate operators $\langle\,F^j_{nm}\cdot F^j_{mn}\,\rangle$ are left. As the result the second order correlators the following contributions vanish in any geometry: In turn the terms non zero terms are

$$\begin{aligned}
\langle\,\delta\tilde{F}^\dagger_1\cdot\delta\tilde{F}_1\,\rangle = {}& |\,g_1\,|^2\sum_j \frac{-\,|\,\delta_1\,|^2\,\gamma_{23}\langle\,\hat{R}^j_{33}\,\rangle}{\left(\gamma^2_{13}/4+(\Delta_1-\omega)^2\right)\left(|\tilde{\delta}_1(\omega)|^2+\frac{|\Omega_1|^4}{\gamma^2_{13}/4+(\Delta_1-\omega)^2}\right)}+\\
&+|\,g_1\,|^2\sum_j \frac{\frac{|\Omega_1\Omega_2|^2}{|\,\tilde{\delta}_2(\omega)\,|^2}\gamma_{23}(\langle\,R^j_{33}\,\rangle+\langle\,R^j_{22}\,\rangle)}{\left(\gamma^2_{13}/4+(\Delta_1-\omega)^2\right)\left(|\tilde{\delta}_1(\omega)|^2+\frac{|\Omega_1|^4}{\gamma^2_{13}/4+(\Delta_1-\omega)^2}\right)}\\
&+|\,g_1\,|^2\sum_j \frac{|\,\Omega_1\,|^2\left(\gamma_{23}\langle\,\hat{R}^j_{33}\,\rangle+\gamma_{12}\langle\,\hat{R}^j_{11}\,\rangle\right),}{\left(\gamma^2_{13}/4+(\Delta_1-\omega)^2\right)\left(|\tilde{\delta}_1(\omega)|^2+\frac{|\Omega_1|^4}{\gamma^2_{13}/4+(\Delta_1-\omega)^2}\right)}
\end{aligned} \tag{A.10}$$

The second correlator:

$$\langle \delta\tilde{F}_2^\dagger \cdot \delta\tilde{F}_2 \rangle = |\, g_2 \,|^2 \frac{|\, \Omega_2 \,|^2 \left(\gamma_{32}\langle \hat{R}_{33}^j \rangle + \gamma_{12}\langle \hat{R}_{22}^j \rangle\right) + |\, \delta_3(\omega) \,|^2 \gamma_{23} \left(\langle R_{33}^j \rangle + \langle R_{22}^j \rangle\right)}{\left|\, \tilde{\delta}_2(\omega) \,\right|^2 \left|\, \left(\tilde{\delta}_1(\omega) + \frac{|\Omega_1|^2}{(\gamma_{13}/2 + i(\Delta_1 - \omega))}\right) \right|^2} \tag{A.11}$$

$$- |\, g_2 \,|^2 \frac{\gamma_{23} \frac{|\Omega_1 \Omega_2|^2}{\gamma_{13}^2/4 + (\Delta_1 - \omega)^2} \langle R_{33}^j \rangle}{\left|\, \tilde{\delta}_2(\omega) \,\right|^2 \left|\, \left(\tilde{\delta}_1(\omega) + \frac{|\Omega_1|^2}{(\gamma_{13}/2 + i(\Delta_1 - \omega))}\right) \right|^2} \tag{A.12}$$

The third correlator:

$$\begin{aligned} &\langle \delta\tilde{F}_1^\dagger \cdot \delta\tilde{F}_2 \rangle \approx |\, g_1 \,|\, |\, g_2 \,|\, |\, \Omega_1 \,|\, |\, \Omega_2 \,| \cdot \\ &\frac{-\left(\gamma_{32}\langle \hat{R}_{33}^j \rangle + \gamma_{12}\langle \hat{R}_{22}^j \rangle\right) - \frac{\tilde{\delta}_1^*(\omega)}{\gamma_{13}/2 + i(\Delta_1 - \omega)} \gamma_{23} \langle R_{33}^j \rangle + \frac{\gamma_{23} \tilde{\delta}_3(\omega)}{\tilde{\delta}_2^*(\omega)} (\langle R_{22}^j \rangle + \langle R_{33}^j \rangle)}{\tilde{\delta}_2(\omega) \left(\gamma_{13}/2 - i\left(\Delta_1 - \omega\right)\right) \left|\, \left(\tilde{\delta}_1(\omega) + \frac{|\Omega_1|^2}{(\gamma_{13}/2 + i(\Delta_1 - \omega))}\right) \right|^2} \end{aligned} \tag{A.13}$$

The last correlator

$$\begin{aligned} &\langle \delta\tilde{F}_2^\dagger \cdot \delta\tilde{F}_1 \rangle = |g_1|\, |\, g_2 \,|\, |\Omega_1||\Omega_2| \cdot \\ &\frac{-\left(\gamma_{23}\langle \hat{R}_{33}^j \rangle + \gamma_{12}\langle \hat{R}_{22}^j \rangle\right) + \frac{\tilde{\delta}_3^*(\omega)}{\tilde{\delta}_2(\omega)} \gamma_{23} \left(\langle \hat{R}_{22}^j \rangle + \langle \hat{R}_{33}^j \rangle\right) - \gamma_{23} \langle \hat{R}_{33}^j \rangle \frac{\tilde{\delta}_1(\omega)}{\gamma_{13}/2 - i(\Delta_1 - \omega)}}{\tilde{\delta}_2^*(\omega) \left(\gamma_{13}/2 + i\left(\Delta_1 - \omega\right)\right) \left|\, \left(\tilde{\delta}_1(\omega) + \frac{|\Omega_1|^2}{(\gamma_{13}/2 + i(\Delta_1 - \omega))}\right) \right|^2} \end{aligned} \tag{A.14}$$

If we can neglect the population on the upper level:

$$\langle \delta\tilde{F}_1^\dagger \cdot \delta\tilde{F}_1 \rangle = |\, g_1 \,|^2 \,|\, \Omega_1 \,|^2 \frac{\gamma_{12}\langle \hat{R}_{11}^j \rangle + \frac{|\Omega_2|^2}{\left|\, \tilde{\delta}_2(\omega) \,\right|^2} \gamma_{23} (\langle R_{22}^j \rangle)}{\left(\gamma_{13}^2/4 + (\Delta_1 - \omega)^2\right) \left(|\tilde{\delta}_1(\omega)|^2 + \frac{|\Omega_1|^4}{\gamma_{13}^2/4 + (\Delta_1 - \omega)^2}\right)}$$

$$\langle \delta\tilde{F}_2^\dagger \cdot \delta\tilde{F}_2 \rangle = |\, g_2 \,|^2 \frac{\left(|\, \Omega_2 \,|^2 \gamma_{12} + |\, \delta_3(\omega) \,|^2 \gamma_{23}\right) \langle R_{22}^j \rangle}{\left|\, \tilde{\delta}_2(\omega) \,\right|^2 \left|\, \left(\tilde{\delta}_1(\omega) + \frac{|\Omega_1|^2}{(\gamma_{13}/2 + i(\Delta_1 - \omega))}\right) \right|^2} \tag{A.15}$$

$$\langle \delta\tilde{F}_1^\dagger \cdot \delta\tilde{F}_2 \rangle = \frac{|\, g_1 \,|\, |\, g_2 \,|\, |\, \Omega_1 \,|\, |\, \Omega_2 \,| \cdot \left(\frac{\tilde{\delta}_1(\omega)}{\tilde{\delta}_2^*(\omega)} \gamma_{23} - \gamma_{12}\right) \langle R_{22}^j \rangle}{\tilde{\delta}_2(\omega) \left(\gamma_{13}/2 - i\left(\Delta_1 - \omega\right)\right) \left|\, \left(\tilde{\delta}_1(\omega) + \frac{|\Omega_1|^2}{(\gamma_{13}/2 + i(\Delta_1 - \omega))}\right) \right|^2} \tag{A.16}$$

$$\langle \delta\tilde{F}_2^\dagger \cdot \delta\tilde{F}_1 \rangle = \frac{|g_1|\, |\, g_2 \,|\, |\Omega_1||\Omega_2| \cdot \left(\frac{\tilde{\delta}_3^*(\omega)}{\tilde{\delta}_2(\omega)} \gamma_{23} - \gamma_{12}\right) \langle \hat{R}_{22}^j \rangle}{\tilde{\delta}_2^*(\omega) \left(\gamma_{13}/2 + i\left(\Delta_1 - \omega\right)\right) \left|\, \left(\tilde{\delta}_1(\omega) + \frac{|\Omega_1|^2}{(\gamma_{13}/2 + i(\Delta_1 - \omega))}\right) \right|^2}$$

Appendix B

Generalized OPO

In the experiment two modes could have different gain due to asymmetrical populations on ground levels $|\,1\,\rangle$ and $|\,2\,\rangle$. Consequentially losses for two modes might vary as well. Here we introduce two different losses $\kappa_{\mathrm{in},1}$ and $\kappa_{\mathrm{in},2}$, and κ is still the losses through an input coupler:

$$\dot{a}_1 = -\chi a_2^\dagger - \frac{\kappa+\kappa_{\mathrm{in},1}}{2}a_1 + \sqrt{\kappa}a_{1,\mathrm{in}} + \sqrt{\kappa_{\mathrm{in},1}}\hat{F}_1 \tag{B.1}$$

$$\dot{a}_2^\dagger = -\chi^* a_1 - \frac{\kappa+\kappa_{\mathrm{in},2}}{2}a_2^\dagger + \sqrt{\kappa}a_{2,\mathrm{in}}^\dagger + \sqrt{\kappa_{\mathrm{in},2}}\hat{F}_2^\dagger \tag{B.2}$$

The solution of this linear system of equations with input-output relations applied, gives the field outside of a resonator:

$$\begin{aligned} a_{\mathrm{out},1}(\omega) =& \frac{\sqrt{\kappa\kappa_{\mathrm{in},1}}\hat{F}_1(\omega)\left(i\omega - \frac{\kappa+\kappa_{\mathrm{in},2}}{2}\right) + \chi\left(\kappa a_{2,\mathrm{in}}^\dagger(-\omega) + \sqrt{\kappa\kappa_{\mathrm{in},2}}\hat{F}_2^\dagger(-\omega)\right)}{\Delta'} + \\ &+ a_{1,\mathrm{in}}(\omega)\frac{\left(i\omega - \frac{\kappa+\kappa_{\mathrm{in},2}}{2}\right)(i\omega + \frac{\kappa-\kappa_{\mathrm{in},1}}{2}) - |\,\chi\,|^2}{\Delta'}, \end{aligned} \tag{B.3}$$

$$\begin{aligned} a_{\mathrm{out},2}^\dagger(-\omega) =& \frac{\sqrt{\kappa\kappa_{\mathrm{in},2}}\hat{F}_2^\dagger(-\omega)\left(i\omega - \frac{\kappa+\kappa_{\mathrm{in},1}}{2}\right) + \chi^*\left(\kappa a_{1,\mathrm{in}}(\omega) + \sqrt{\kappa\kappa_{\mathrm{in},1}}\hat{F}_1(\omega)\right)}{\Delta'} + \\ &+ a_{2,\mathrm{in}}^\dagger(-\omega)\frac{(i\omega - \frac{\kappa+\kappa_{\mathrm{in},1}}{2})(i\omega + \frac{\kappa-\kappa_{\mathrm{in},2}}{2}) - |\,\chi\,|^2}{\Delta'}, \end{aligned} \tag{B.4}$$

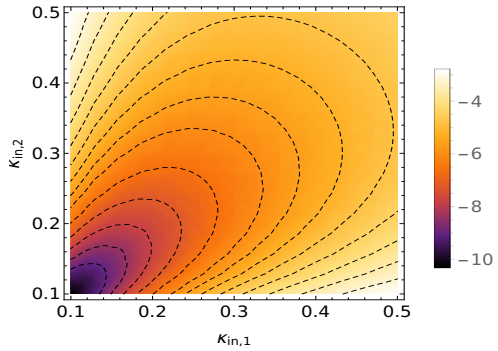

Figure (B.1) Dependence of maximum squeezing level on losses in both channels $\kappa_{\mathrm{in},1}$ and $\kappa_{\mathrm{in},2}$.

where the denominator is $\Delta' = |\chi|^2 - (i\omega - \frac{\kappa+\kappa_{\mathrm{in},1}}{2})(i\omega - \frac{\kappa+\kappa_{\mathrm{in},2}}{2})$.

The arbitarary quadrature variance:

$$\langle \Delta Q_{\pm}^2 \rangle = \frac{|\alpha_1|^2 + |\alpha_2|^2 + |\beta_1|^2 + |\beta_2|^2 + |\gamma_1|^2 + |\gamma_2|^2 + |\mu_1|^2 + |\mu_2|^2}{2} \pm$$
$$\pm \Re e \left(\alpha_1 \alpha_2^* e^{-i(\theta_1+\theta_2)} + \beta_1^* \beta_2 e^{i(\theta_1+\theta_2)} + \gamma_1 \mu_1^* e^{-i(\theta_1+\theta_2)} + \gamma_2 \mu_2^* e^{-i(\theta_1+\theta_2)}\right), \quad \text{(B.5)}$$

where coefficients are:

$$\alpha_1 = \frac{\left(i\omega - \frac{\kappa+\kappa_{\mathrm{in},2}}{2}\right)(i\omega + \frac{\kappa-\kappa_{\mathrm{in},1}}{2}) - |\chi|^2}{\Delta'}, \quad \beta_1 = \frac{\chi\kappa}{\Delta'}, \quad \gamma_1 = \frac{\sqrt{\kappa\kappa_{\mathrm{in},1}}\left(i\omega - \frac{\kappa+\kappa_{\mathrm{in},2}}{2}\right)}{\Delta'},$$
$$\beta_2 = \frac{(i\omega - \frac{\kappa+\kappa_{\mathrm{in},1}}{2})(i\omega + \frac{\kappa-\kappa_{\mathrm{in},2}}{2}) - |\chi|^2}{\Delta'}, \quad \alpha_2 = \frac{\chi^*\kappa}{\Delta'}, \quad \mu_2 = \frac{\sqrt{\kappa\kappa_{\mathrm{in},2}}\left(i\omega - \frac{\kappa+\kappa_{\mathrm{in},1}}{2}\right)}{\Delta'},$$
$$\mu_1 = \frac{\chi^*\sqrt{\kappa\kappa_{\mathrm{in},1}}}{\Delta'}, \quad \text{and} \quad \gamma_2 = \frac{\chi\sqrt{\kappa\kappa_{\mathrm{in},2}}}{\Delta'}.$$

Appendix C

Steady-state population

C.1 Approximate solution

As a zero order approximation we assume the atomic system under an action of two classical pumps without any quantum fields and stochastic operators. In this case the corresponding Heisenberg equations are:

$$\frac{dR_{13}^j}{dt} = -(i\Delta_1 + \gamma_{13}/2)R_{13}^j - i\Omega_2(z_j)(R_{11}^j - R_{33}^j) - i\Omega_1(z_j)\hat{R}_{12}^j \tag{C.1}$$

$$\frac{dR_{31}^j}{dt} = (i\Delta_1 - \gamma_{13}/2)R_{31}^j + i\Omega_2(z_j)(R_{11}^j - R_{33}^j) + i\Omega_1(z_j)\hat{R}_{21}^j \tag{C.2}$$

$$\frac{dR_{32}^j}{dt} = (i\Delta_2 - \gamma_{23}/2)R_{32}^j + i\Omega_1^*(z_j)(R_{22}^j - R_{33}^j) + i\Omega_2^*(z_j)\hat{R}_{12}^j \tag{C.3}$$

$$\frac{dR_{23}^j}{dt} = (-i\Delta_2 - \gamma_{23}/2)R_{23}^j - i\Omega_1^*(z_j)(R_{22}^j - R_{33}^j) - i\Omega_2(z_j)\hat{R}_{21}^j \tag{C.4}$$

$$\frac{dR_{12}^j}{dt} = -(i\delta + \gamma_{12}/2)\hat{R}_{12}^j - i\Omega_1^*(z_j)R_{13}^j + i\Omega_2(z_j)R_{32}^j \tag{C.5}$$

$$\frac{d(R_{11}^j - R_{22}^j)}{dt} = (\gamma_{13} - \gamma_{23})R_{33}^j - i\Omega_2(z_j)R_{13}^j + i\Omega_2(z_j)R_{31}^j + i\Omega_1(z_j)R_{23}^j - i\Omega_1(z_j)R_{32}^j \tag{C.6}$$

$$\frac{dR_{33}^j}{dt} = -(\gamma_{13} + \gamma_{23})R_{33}^j + i(\Omega_2(z_j)R_{13}^j + \Omega_1(z_j)R_{23}^j) - i(\Omega_2(z_j)R_{31}^j + \Omega_1(z_j)R_{32}^j) \tag{C.7}$$

C.2 Collective operator approach

We introduced collective operators in the main text (Eqs. (2.82)–(2.83)) and assumed phase matching and all coupling constants to be homogeneous, thus the system of equations:

$$\frac{d\hat{a}_1}{dt} = -(i\delta_1 + \kappa/2)\hat{a}_1 - i\sqrt{N}g_1^*\hat{R}_{13} + \sqrt{\kappa}\hat{a}_{in,1} \tag{C.8}$$

$$\frac{d\hat{a}_2^\dagger}{dt} = -(-i\delta_2 + \kappa/2)\hat{a}_2^\dagger + i\sqrt{N}g_2\hat{R}_{32} + \sqrt{\kappa}\hat{a}_{in,2}^\dagger \tag{C.9}$$

$$\frac{d\hat{R}_{13}}{dt} = i\sqrt{N}(g_1\hat{a}_1 + \Omega_2)(\hat{R}_{33} - \hat{R}_{11}) - (i\Delta_1 + \gamma_{13}/2)\hat{R}_{13} - i\Omega_1\hat{R}_{12} + \frac{1}{\sqrt{N}}\sum_j \hat{F}_{13}^j \tag{C.10}$$

$$\frac{d\hat{R}_{32}}{dt} = i\sqrt{N}(g_2\hat{a}_2^\dagger + \Omega_1)(\hat{R}_{22} - \hat{R}_{33}) + (i\Delta_2 - \gamma_{23}/2)\hat{R}_{32} + i\Omega_2\hat{R}_{12} + \frac{1}{\sqrt{N}}\sum_j \hat{F}_{32}^j \tag{C.11}$$

$$\frac{d\hat{R}_{12}}{dt} = -(i\delta + \gamma_{12}/2)\hat{R}_{12} - i\Omega_1(z_j)\hat{R}_{13} + i\Omega_2(z_j)\hat{R}_{32} + \frac{1}{\sqrt{N}}\sum_j \hat{F}_{12} \tag{C.12}$$

$$\frac{d\hat{R}_{11}}{dt} = \gamma_{13}\hat{R}_{33} + iN^{-1/2}(g_1\hat{a}_1 + \Omega_2)\hat{R}_{31} - iN^{-1/2}(g_1\hat{a}_1^\dagger + \Omega_2)\hat{R}_{13} \tag{C.13}$$

$$\frac{d\hat{R}_{22}}{dt} = \gamma_{23}\hat{R}_{33} + iN^{-1/2}(g_2\hat{a}_2 + \Omega_1)\hat{R}_{32} - iN^{-1/2}(g_2\hat{a}_2^\dagger + \Omega_1)\hat{R}_{23} \tag{C.14}$$

$$\hat{R}_{33} = 1 - \hat{R}_{11} - \hat{R}_{22} \tag{C.15}$$

Appendix D

PDH circuit diagram

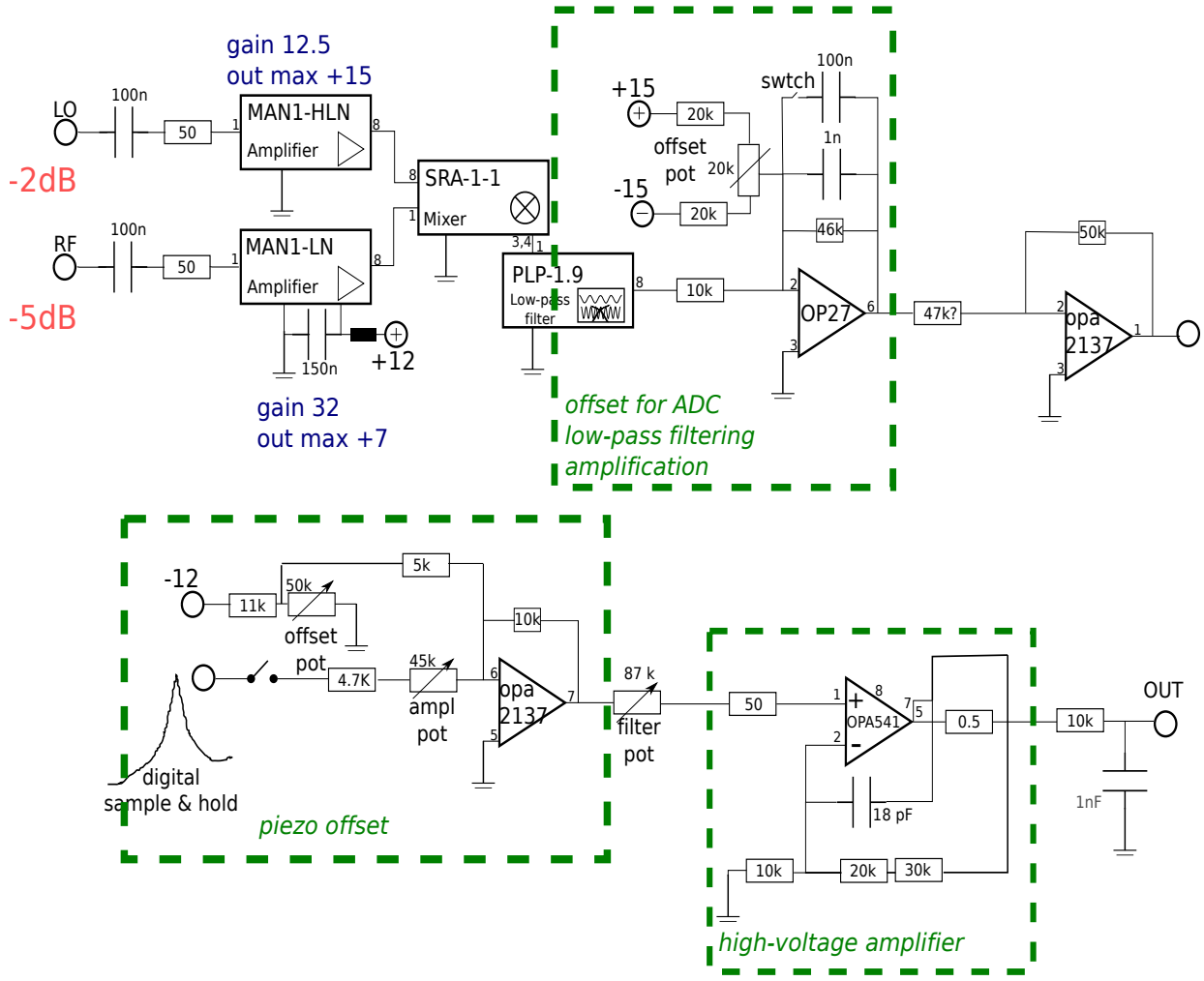

Figure (D.1) PDH circuit diagram

Appendix E

DAVLL circuit

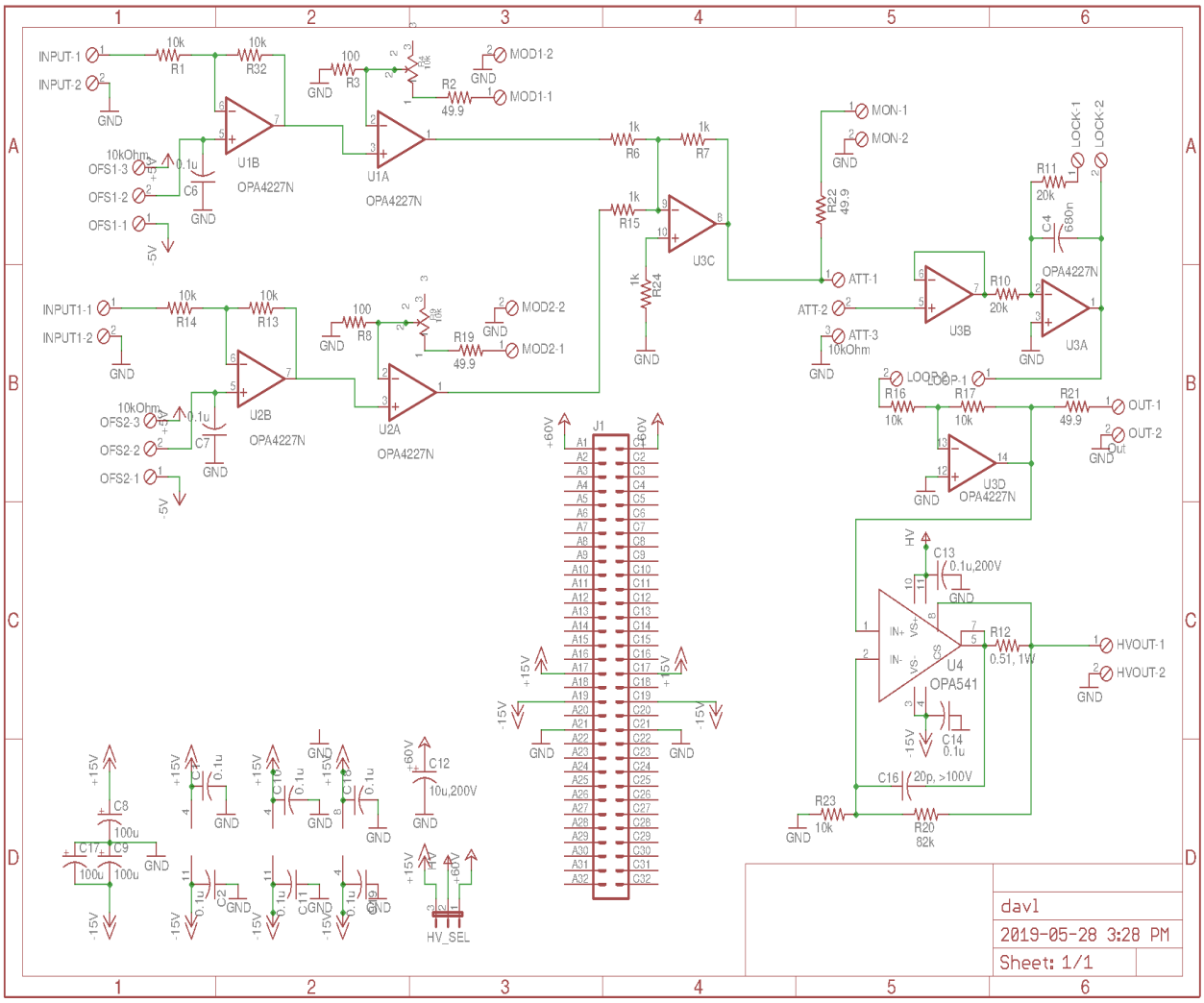

Figure (E.1) DAVLL circuit diagram

Appendix F

Magnetic coil switch

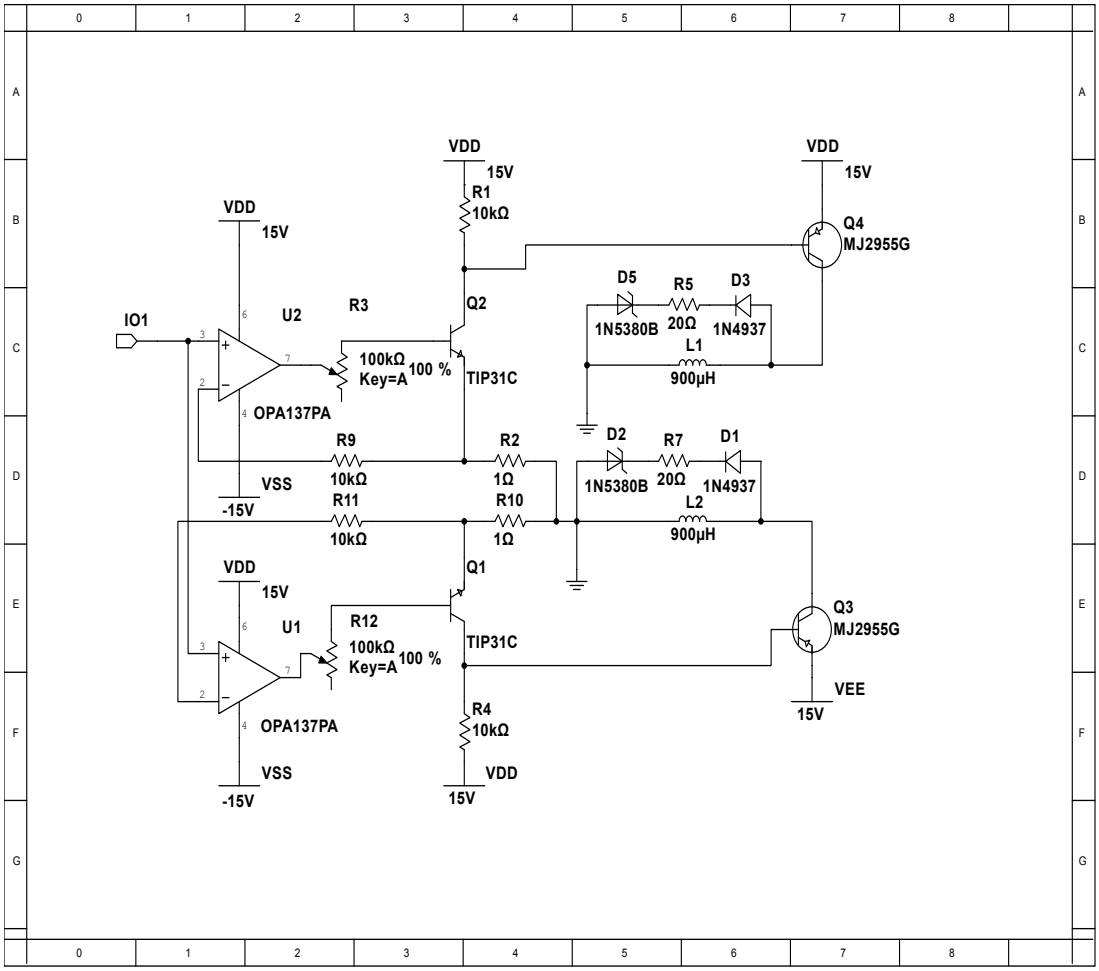

Figure (F.1) Magnetic switch circuit diagram